HOKKAIDO UNIVERSITY

Title	Formation Behavior of Nanostructured Anodic Films on Metals in Fluoride Containing Organic Electrolytes
Author(s)	Shahzad, Khurram
Citation	北海道大学. 博士(工学) 甲第12503号
Issue Date	2016-12-26
DOI	10.14943/doctoral.k12503
Doc URL	http://hdl.handle.net/2115/64448
Type	theses (doctoral)
File Information	Khurram_Shahzad.pdf

Instructions for use

Hokkaido University Collection of Scholarly and Academic Papers : HUSCAP

Formation Behavior of Nanostructured Anodic Films on Metals in Fluoride Containing Organic Electrolytes

2016

Doctoral thesis

Khurram Shahzad

Laboratory of Interfacial Electrochemistry, Graduate School of Chemical
Sciences and Engineering, Hokkaido University, Japan

Table of contents

Abstract

Chapter 5 **Growth of barrier-type anodic film on magnesium in EG-water mixed electrolytes containing fluoride and phosphate**………………………………...91

List of publications

Acknowledgement

Abstract

Porous anodic alumina films with self-ordered nanopore channels have been used for surface treatment of aluminum and its alloys to improve corrosion and wear resistance. The films are also of recent interest as key materials for nanodevices and as template for fabrication of nanomaterials. Self-ordering electrochemical anodizing has been recently extended to other metals including titanium, zirconium, niobium, iron and stainless steel, and these nanostructured anodic films have many promising applications. The extensions to many metals and alloys were mainly achieved by finding novel organic electrolytes containing fluoride and small amounts of water. Although extensive studies on formation mechanism of porous anodic alumina films formed in aqueous acid electrolytes have been conducted, little is known about the growth mechanism of the anodic films in the organic electrolytes, particularly on iron that is the most important practical metal. Understanding the growth mechanism is of significant importance to control the morphology and composition of the anodic films. Thus, this study focused on elucidating the growth mechanism of the nanostructured anodic films on iron. Further, in this study it was found that the fluoride-containing organic electrolytes with a wide range of water concentrations are suitable for the formation of compact, so-called barrier-type anodic films on magnesium, which is also a practically important light metal.

This dissertation includes six chapters. Chapter 1 describes the general introduction of anodizing and objective of this dissertation. In chapter 2, the preparation of materials and experimental conditions employed for this study as well as major characterization techniques were described in detail.

Chapter 3 describes the critical factors influencing the film morphology and growth mechanism on the anodic film on iron. Water concentration in electrolyte influences largely the film structure and composition of the anodic film as well as the distribution of fluoride-rich layer within the anodic film. For instance, scalloped metal/film interface, typical of porous anodic alumina, was observed only when the water concentration was ≥ 1.5 mol dm^{-3}. At lower water concentrations the interface became flat. A thinner barrier layer beneath the porous layer was formed by an increase in water concentration. Carbon and fluoride incorporations were also suppressed at high water concentration. TEM observations clearly disclosed that fluoride enrichment occurred at the cell boundaries as well as at the scalloped metal/film interface when the water concentration was 1.5 ml dm^{-3}. The preferential dissolution of fluoride-rich cell boundaries caused the development of self-ordered nanotubular anodic films at high water concentrations. In contrast, no fluoride enrichment was found at cell boundaries when the water concentration was low (0.1 mol dm^{-3}). Thus, no nanotubular film was formed at low water concentrations. Through the findings in this

chapter, a transition of the growth mechanism from “field-assisted dissolution” to “field-assisted flow” with water concentration was proposed.

In Chapter 4, a barrier-type anodic film was formed on magnetron-sputtered iron by employing potentiodynamic anodizing at a relatively fast sweep rate, and the influence of electric field on the dissolution of the barrier-type anodic film was examined. It was found from Rutherford backscattering spectroscopy that the barrier-type anodic film formed in ethylene glycol electrolyte containing 0.1 mol dm^{-3} NH_4F and 0.1 mol dm^{-3} water consists of two layers, comprising an outer iron hydroxy-fluoride layer and an inner iron fluoride layer, with the latter layer forming as a consequence of the faster migration of fluoride ions in comparison with oxygen species. The barrier layer was formed even at a current efficiency as low as 49%. The application of electric field to the barrier-type film on iron accelerated the chemical dissolution of the anodic film at the film/electrolyte interface. Below the critical field of approximately 2.8 MeV cm^{-1}, uniform thinning of the anodic film occurred due to field-assisted dissolution, while a nanoporous film was developed above the critical field. The critical field for anodic film on iron is much lower than that recently examined on aluminum (~5.5 MeV cm^{-1}).

In chapter 5, the uniform growth of barrier-type anodic film on magnetron-sputtered magnesium was examined in fluoride and phosphate-containing ethylene glycol-H_2O mixed and aqueous electrolytes. The addition of phosphate to fluoride-containing organic electrolytes induced amorphization of anodic film and increases the volume expansion factor. The anodic films consisted of phosphate-incorporated oxyfluoride and the concentration of incorporated phosphate decreased gradually with an increase in water concentration. The anodic films consist of two layers with an inner layer containing less amount of phosphate. The outer layer is formed at the film/electrolyte interface by the migration of Mg^{2+} ions outwards, while the inner layer is formed at the metal/film interface. The efficiency of film growth reduced from 100 % at 0.1 mol dm^{-3} H_2O to ∼ 52% in aqueous electrolyte. Despite the low efficiency in aqueous electrolyte, a barrier-type anodic film with a uniform thickness was developed. The reason for the formation of the barrier-type anodic film, not the porous-type film, at such low efficiency was discussed.

Chapter 6 is the general conclusion of this dissertation and future prospects of anodizing research are described.

Chapter 1

Introduction and Literature Survey

1.1 Introduction

Nanotechnology, in combination with surface engineering, focused on the fabrication of various new materials has become a subject of immense scientific interest in recent years. Particularly, the inexpensive formation of ordered structures such as nanopores, nanotubes, and nanowires etc. with a periodicity less than 100 nm, has triggered extensive activities in research. Moreover, in micro/nanofabrication's, ordered porous structures formed by anodizing of valve metals, such as aluminum, titanium, zirconium, tungsten, play a key role in technological evolution. Under controlled conditions, porous structures can be tailored to a variety of morphologies to match the particular practical application.

Over the last 80 years, anodizing of aluminum, which thickens the natural oxide layer by the application of suitable current and/or voltage, has been established as a well-known commercial process for the fabrication of a corrosion-protection and wear-resistant layer as well as a decorative coating on aluminum surfaces. The structure of porous anodic films on aluminum was first proposed by Keller *et al*. in 1953 by means of transmission electron microscope (TEM) to examine the hexagonally closed-packed structure [1]. Later in 1995, Masuda and Fukuda found that under certain anodizing conditions, self-organized nanoporous oxide structure can be produced on aluminum [2], which extends the applications of such films in aerospace, biomedical, architecture, nanotechnology, and as templates for the fabrication of nanomaterials in the form of nanowires, nanopores, and nanotubes [1-7]. In addition to practical applications of these films, fundamental aspects of anodic films such as ionic transport processes under high electric field and the correlation between film formation conditions, and the film morphology, composition, structure, and properties have also been investigated extensively in recent years [8-13]. These films are generally formed in aqueous electrolytes under direct current or voltage at various temperatures.

1.2 Types of anodic oxide films

Depending on substrate metals and the anodizing conditions, such as pH and the composition of electrolyte, temperature, and applied current/voltage, three types of anodic films can be produced: barrier-type, porous-type, and nanotubular-type [14-16].

1.2.1 Barrier-type anodic films

Barrier-type anodic films on many metals are generally formed in electrolytes which have very low chemical reactivity with the oxide and they are formed under suitable current density at high efficiency with almost no loss of film formation species from film material to the electrolyte. Flaws or defects always exist in the barrier layer and their population densities are of the order of 10^8 to 10^{10} m^{-2} [17]. Flaws population depends on the surface pretreatment employed and the film thickness. The generation of flaws is mainly related with local heterogeneities in the metal substrate [18]. The presence of such surface defects and surface treatment employed prior to anodizing may cause the reduction of current efficiency. During the growth of barrier-type films at 100 % Faradaic efficiency, formation voltage increases linearly with time until the dielectric breakdown of the anodic film occurs at a certain voltage, which is depending on the type of metallic substrate and electrolyte used. The barrier-type films are compact and thin, usually less than several hundred nanometers, and find applications for capacitors and corrosion protection. Barrier-type anodic films formed on Al, Bi, Nb, Ta, and W are usually amorphous. The thickness of barrier layer is proportional to the formation voltage before reaching to dielectric breakdown [19-24].

Xu *et al.* reported that growth of barrier-type or porous-type films on aluminum depends on the effective current density and hence the current efficiency in a specific electrolyte [25]. The growth efficiency of the barrier-type film at the film/electrolyte interface decreases with a decrease in current density and the pH of the electrolyte employed. For low current densities than a critical value, film formation at the film/electrolyte interface is lost locally by field-induced dissolution and a porous layer commences to grow. In the case of aluminum anodizing, this critical current density for the formation of a porous film depends on the electrolyte concentration, temperature, and pH of the electrolyte [25]. Extensive studies on barrier-type anodic alumina films show that these films are not pure oxides of aluminum, but also contain a small amount of electrolyte-derived anion species that significantly influence the properties of resultant anodic films. In addition, the distribution and extent of the depth of these species within the film is complex. Shimizu *at el.* and Skeldon *at al.* have reported that the distribution of incorporated species is determined by the transport number of metals ions as well as by the relative migration rates of incorporated species during the growth of barrier films. Boron, phosphate, chromium, molybdenum, and tungsten species are usually incorporated into the anodic films to varying depth in borate, phosphate, chromate, molybdate, and tungstate electrolytes, respectively. Such species can be used as tracers for the investigation of ion transport processes during the film growth [26-31]. It is well-known in aluminum anodizing that phosphate is incorporated within outer two-third of the anodic film and an inner one-third is usually a phosphate-free, relatively pure alumina region. Investigations of the barrier-type anodic films on aluminum revealed that inward migrating phosphorous species migrate at a rate of ~ 0.5 times that of O^{2-} [32-34].

The incorporation and different depth distributions of various electrolyte anion-derived species are strongly correlated with the ionic transport process in growing anodic oxides. Extensive research work on the growth of barrier-type anodic film on aluminum has been done to clarify whether the growth proceeds owing to the migration of metal cation through the film to react with electrolyte species, or due to the migration of oxygen anions across the film to react with the metal at the metal/film interface, or due to the migration of both cations or anion species. Hoar and Mott reported that hydroxyl ions also carry the ionic current during film growth and the outer region of the film materials are usually hydrated while Brock and Wood suggested that only oxide anions are mobile as no hydration is found in glycerol-based organic electrolytes [35, 36].

It is well known that the growth of amorphous barrier-type films proceeds by high field conduction mechanisms, where transportation of ionic species occurs under the electric field of 10^6-10^7 V cm^{-1} and new film material is formed at the film/electrolyte and metal/film interfaces by outward migration of metal cations and inward migration of electrolyte-derived anion species, respectively, as shown in **Fig. 1.1.** In contrast to aluminum, films formed on some metals such as zirconium and hafnium are crystalline and growth proceeds predominantly by the migration of O^{2-} ions, with a minor contribution from zirconium cations Zr^{4+} [37]. Films formed on titanium show a transition from amorphous to a mixture of amorphous and crystalline oxide at relatively low voltages less than 10 V [38]. The current density, I, during amorphous film growth is related to the electric field by the following equation [39],

$$i = \mathrm{A} \exp (\mathrm{B}E) \qquad (1\text{-}1)$$

where E is the electric field, A and B are constants that depend on temperature. The electric field E is further related to the anodizing voltage, V, and film thickness, d, by the following equation.

$$V = Ed \qquad (1\text{-}2)$$

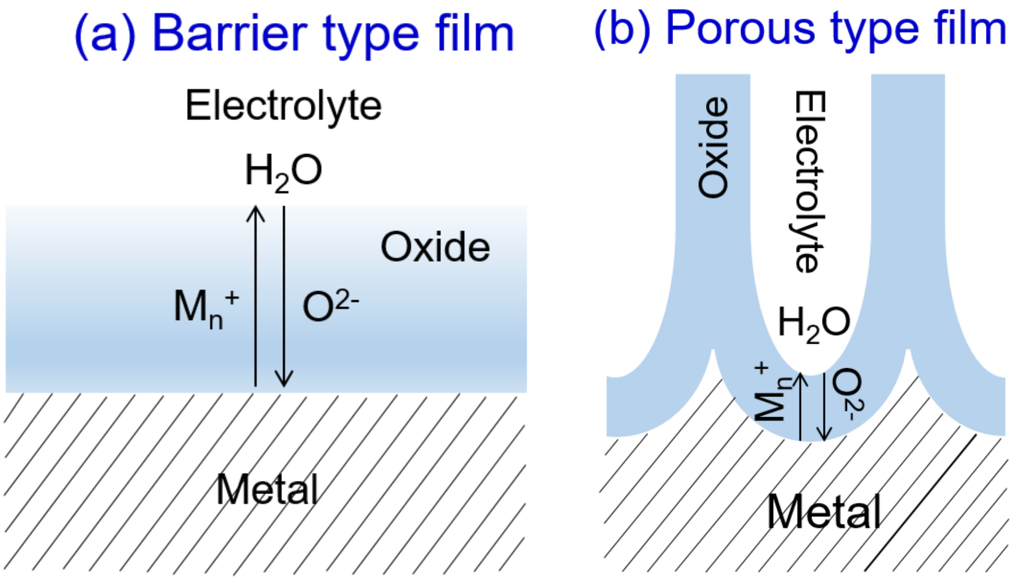

Figure 1.1 Schematic illustration of ionic transport processes (a) barrier-type anodic alumina, (b) Porous-type anodic alumina.

Various tracer techniques such as ion implantation, micro-analytical, and radioactive techniques have also been employed to understand the ionic transport processes [35-36, 40-41]. It was confirmed using an immobile xenon marker that counter migrations of both oxygen and aluminum species contribute to barrier film formation. It is now well known that aluminum cation transport number is approximately 0.4 under 100 % Faradaic efficiency [42]. Later studies on barrier-type film on aluminum suggested that electrolyte-derived species are incorporated within the film at a constant rate under constant current film growth and electrolytes-derived species could be immobile, migrate outwards or inwards at different rates [43-45]. Wood *et al.* presented a model for the incorporation of electrolyte-derived species during the growth of barrier type anodic films in aqueous electrolytes at constant current density [44] as shown in **Fig. 1.2**. They concluded that the amount of electrolyte-derived species to aluminum is independent of the Faradaic efficiency for the species that are mobile inwards, whereas dependent on the efficiency for the species that are mobile outwards.

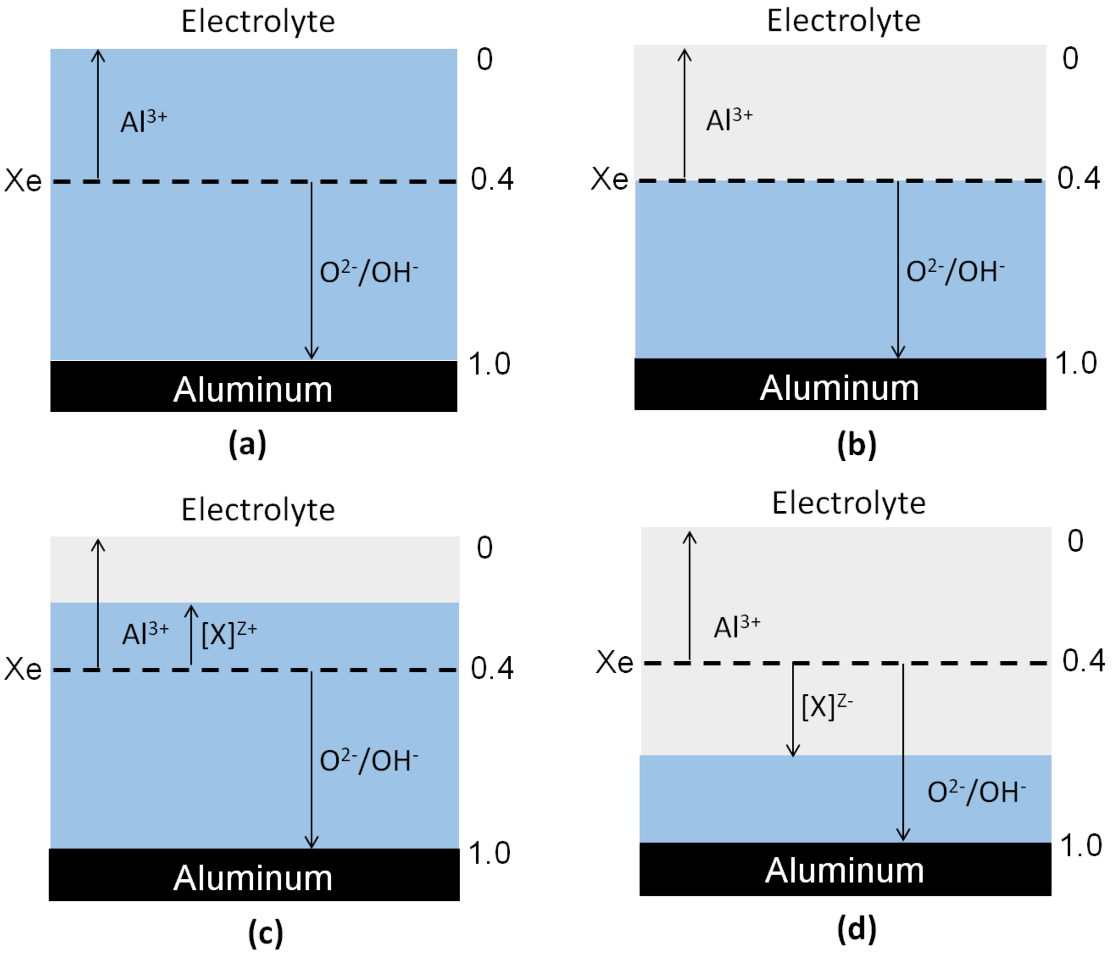

Figure 1.2 Schematic diagram of immobile Xenon tracer experiments to determine the migration of electrolytes species during the barrier-type films formed in aqueous electrolytes galvanostatically at 100 % Faradaic efficiency; (a) impurity-free anodic alumina film, (b) anodic alumina film containing an immobile electrolyte species that contaminate the outer 0.4 of the film, (c) anodic alumina film containing electrolyte species migrating outwards that contaminate < 0.4 of the film thickness and, (d) anodic alumina film containing electrolyte species migrating inwards that contaminate > 0.4 of the film thickness [Reproduced from 44].

1.2.2 Porous-type anodic films

The formation behavior of compact barrier films is relatively simple in terms of electrochemical theories with the film thickness is controlled by formation voltage. In contrast, the formation behavior and the formation mechanism of self-organized porous oxide films have attracted much debate in recent years. These films on aluminum are formed in certain acidic and alkaline electrolytes, such as phosphoric acid, oxalic acid, sulfuric acid, and borax that have the capability of partially dissolving the film. In potentiostatic anodizing, the current decreases continuously when a barrier type anodic film is formed at high current efficiency, while a steady current appears when a porous anodic film is developed. The porous-type anodic films comprise a relatively thick porous layer with numbers of cylindrical pores normal to the metal substrate and a thin barrier layer sandwiched between the metal substrate and the porous layer. Various film parameters, including barrier layer thickness, and pore, and cell sizes, are directly proportional to anodizing voltage. These films are usually formed by anodizing at a constant voltage or constant current. The typical voltage vs time and current density vs time responses during porous film growth are shown in **Fig. 1.3**.

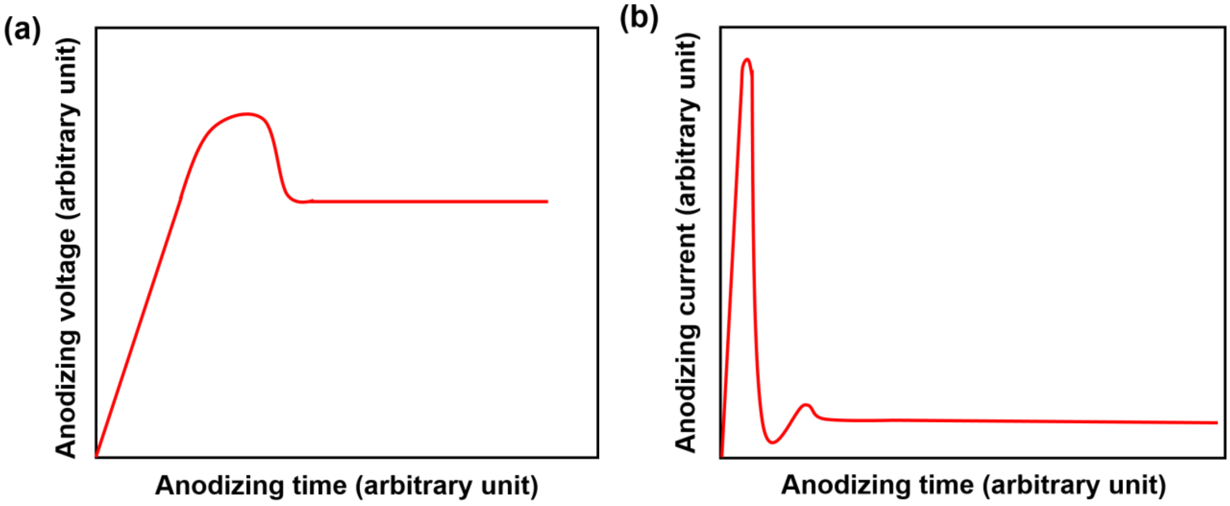

Figure 1.3 Typical voltage-time and current density-time responses during anodizing at (a) constant current condition and (b) constant voltage condition.

When a constant current is applied to the growth of porous film, the cell voltage rises linearly with time until the maximum is reached, and then decreases gradually to a steady sate voltage. Linear non-steady rise of potential is associated with thickening of a barrier layer and then, pores start to develop when the voltage-time curve is deviated from the slope of the linear voltage rise. At the steady-state constant voltage, thickening of porous layer proceeds with the barrier layer thickness remained constant. In anodizing at a constant voltage, an initial rapid current rise is observed, followed by a decrease in current density to a minimum value. Thereafter current rises to local maximum before reaching to steady state.

1.2.2.1 Growth mechanism of porous film

It is well known that growth of porous anodic film on aluminum occurs by the inward migration of O^{2-} ions through the barrier at the metal/film interface and outward migration of Al^{3+} ions, where they are ejected into the electrolyte at the pore base without forming any film material at the film/electrolyte interface **(Fig. 1.1)**. However, the precise mechanism of porous film formation is still the subject of debate and the causes of formation of the highly order porous structure as a consequence of substrate pre-treatment and anodizing parameters are still not well-defined. It is generally presumed that generation of pores is associated with the dynamic equilibrium between the rate of oxide formation at the metal/film interface and the dissolution of oxide at the film/electrolyte interface. Development of pores causes the electric field and ionic current to be concentrated only in the barrier layer beneath the pores. As a result of this concentrated electric field, migration of anions continues to form a solid film at the film/electrolyte interface. Simultaneously Al^{3+} ions are ejected to the electrolyte at the pore base under the influence of high electric field across the barrier layer.

Various mechanisms have been proposed to explain the formation of porous film formation [8, 46-51]. Hoar and Mott suggested that pore formation was associated with the field-induced and thermally assisted dissolution of anodic alumina at the pore base [35]. O' Sullivan and Wood proposed that field-assisted dissolution is accelerated by the polarization of Al-O bonds [19, 48]. Clerki *et al.* employed the O^{18} tracers to investigate the mechanisms of dissolution, transport, and growth associated with oxygen during the formation of porous films and estimated that 40 % of ionic current is carried by aluminum ions, while about 60 % is transported by oxygen anions. They also found that pore formation causes the loss of aluminum cations to the electrolyte rather than oxygen ions resulting reduced growth efficiency close to 60 % for porous film formation [49, 50]. The field-assisted ejection of aluminum cations to the electrolyte was first confirmed by Xu *et al.* using a xenon inert marker [25]. Sato gave the concept of plastic flow and mechanical breakdown of the oxide film and estimated that electrostriction stresses at the pore bottom are 100 times higher than that acting on the pore walls and proposed that stresses at the pore bottom are sufficient for plastic flow of oxide materials from pore base [50]. In addition to the experimental study, the various mathematical model has also been developed, based on ionic transport processes and interfacial reactions, as well as on the effects of surface energy, and elastic stress [52, 53]. Houser and Hebert proposed a model for the potential distribution in porous anodic alumina films during steady state growth using computational approach [9]. Recently, Garcia-Vergara *et al.* proposed a flow mechanism based on direct experimental evidence, to explain the mechanism of pore generation and development in porous anodic alumina films. They found an increase in thickness of porous anodic films relative to that of metal consumed by an expansion factor of 1.35 during anodizing in 0.4M sulfuric and phosphoric acids. This value of expansion factor exceeded the expected value of 1.16 based on purely field-assisted dissolution model. They estimated that increased film thickness is equal to pore volume. They predicted that plastic flow of alumina beneath the pore in the presence of ion transport and compressive stresses displace the material from the barrier layer towards the cell wall region and this contributes to an increased thickness of porous film relative to that of metal consumed [54]. Garcia-Vergara *et al.* and Skeldon *et al.* also conducted a series of tracer experiments and they incorporated tungsten tracer into the sputtered-deposited aluminum substrate prior to anodizing in phosphoric acid electrolyte [55-56]. They found by direct TEM observations that tungsten band is distorted, flowing upwards toward the cell wall regions from the pore base as pore develops. These findings are contradictory to the field-assisted dissolution model of pore development, indicating the flow of film material owing to the plasticity and high compressive stresses in the barrier layer of porous anodic alumina films. A schematic diagram, indicating flow mechanism is shown in **Fig. 1.4**, which shows the incorporation of tungsten tracer into the barrier layer and its subsequent migration towards the pore wall.

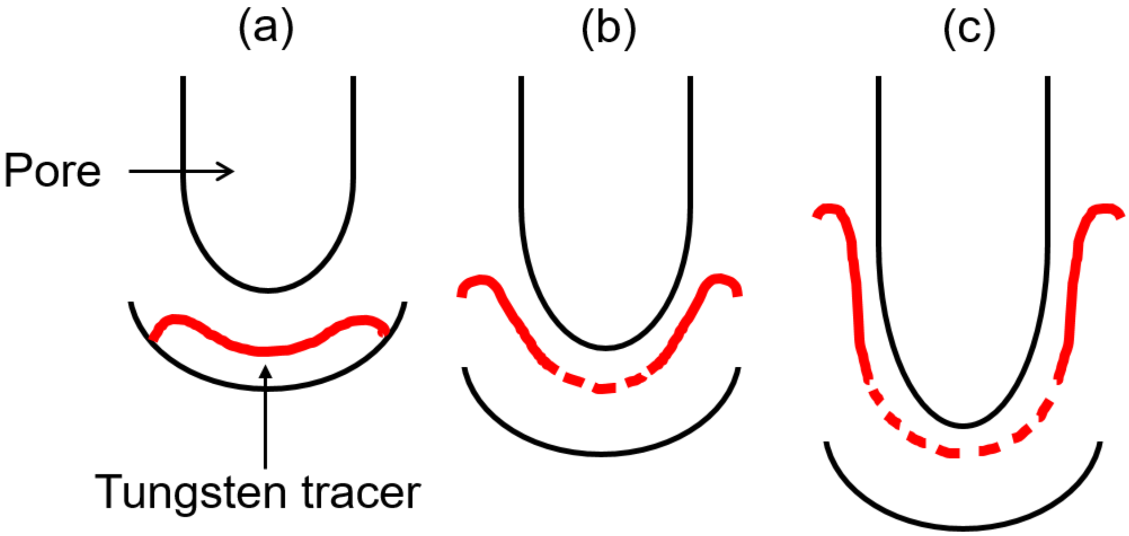

Figure 1.4 Schematic diagram illustrating the migration of tungsten tracer band during growth of porous film on aluminum; (a) tungsten tracer in the barrier layer and (b, c) migration of tungsten tracer towards the walls from pore base during pore growth [Reproduced from 55].

1.2.3 Nanotubular-type anodic films

In addition to barrier and porous-type anodic films, self-organized ordered nanotubular anodic films on titanium [57], zirconium [58], niobium [59], tantalum [60], and iron [61] have also attracted significant attention because of their unique properties in various fields, including energy conversion, photo-catalysis and biomedical devices, since the observation of titanium surface by Assefpour-Dezeuly *et al.* [62] and formation of self-organized nanotubes on titatnium, by Zwilling *et al*. [63-66]. Among various porous morphologies, nanotubular morphology provides an extra degree of freedom in its wall thickness that can be tuned in addition to the diameter and length of nanotubes to obtain the required properties. Furthermore, nanotubes provide a large surface area than nanowires of the same diameter and length. The desired morphology of nanotubes depends on applied voltage, duration, temperature, and fluoride concentration. While voltage, duration, and fluoride concentration primarily controls the nanotube length, diameter, and growth rate, the electrolyte composition including water content, pH, viscosity, and conductivity also affect the nanotube properties. Apart from the optimization of nanotubes growth parameters for specific applications, several studies have been conducted for the investigation of growth mechanism and efforts have been made to understand the transitional behavior from nanoporous to the nanotubular structure. The nanotubes are normally formed under constant potential in fluoride-containing non-aqueous glycerol and ethylene glycol electrolytes and in aqueous electrolytes [67-70]. Recent direct observation on the formation of nanotubes on titanium and zirconium in non-aqueous electrolytes have proved that transition from nanoporous to nanotubular films starts along the cell boundaries [71-73]. The formation of the fluoride-rich layer along the cell boundaries can be explained by their fast migration rate compared with oxide anions [74-75]. These fluoride species are then preferentially dissolved into the electrolyte, thus forming the nanotubes. A schematic of fluoride enrichment and dissolution is shown in **Fig. 1.5.** However, it is extremely difficult to detect thin fluoride-rich layer along the cell boundaries, therefore, the above-mentioned mechanism remained speculative.

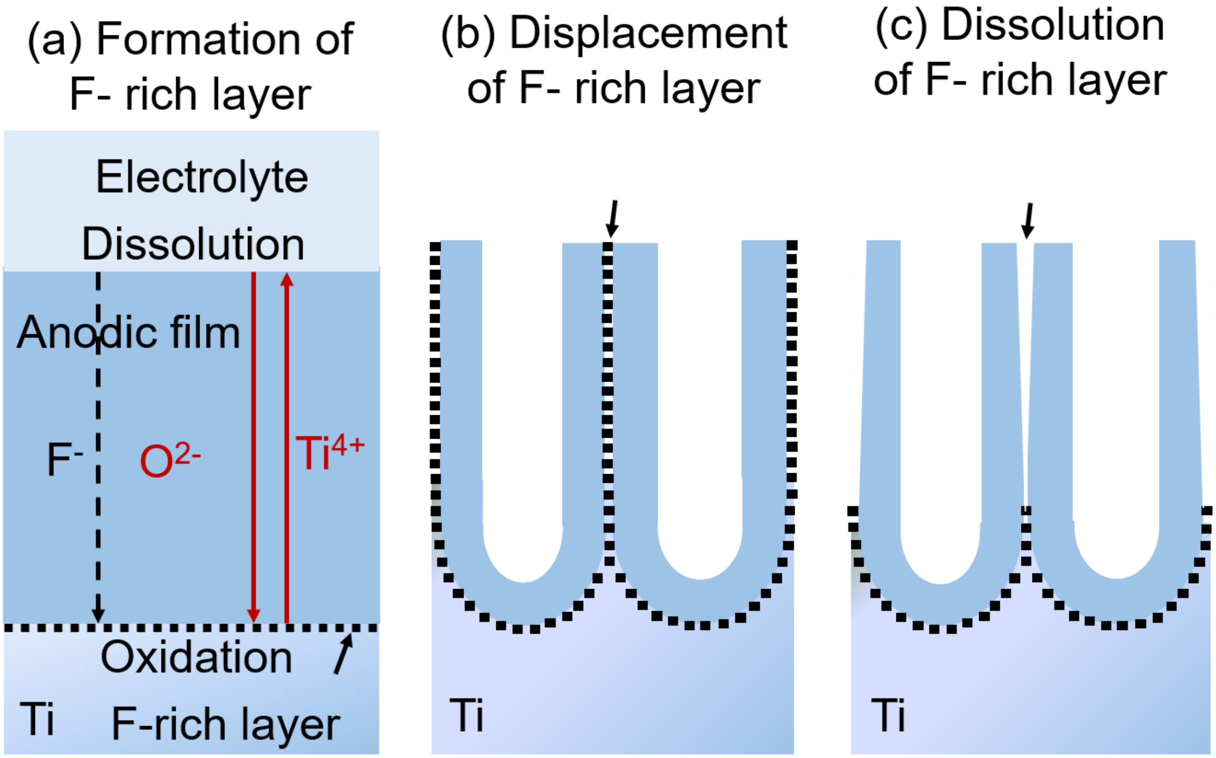

Figure 1.5 Schematic illustration of TiO_2 nanotubes formation (a) formation of fluoride rich-layer, (b) displacement of F-rich layer, and (c) dissolution of fluoride-rich layer [72, 73]. The fluoride-rich layer is indicated by a broken line.

1.3 Fabrication of iron-based anodic films

The formation of self-organized nanoporous and nanotubular films have now been extended recently to a range of valve metals and their alloys including tantalum, zirconium, niobium, tungsten, and hafnium, and such films have diverse potential applications. In addition to valve metals, self-organized nanoporous and nanotubular anodic films have also been reported in the last decade on non-valve metals, including iron and stainless steels; such films have been formed mainly in organic electrolytes containing fluoride and small amounts of water [76-82].

Iron belongs to a special class of materials which combines low cost, abundant availability, chemical stability, functionality and can be oxidized to different valence states such as FeO, Fe_2O_3, Fe_3O_4 and hence is the subject of immense debate in various fields including humidity and gas sensors, as photocatalysts, magnetic storage devices, lithium ion batteries, and electrodes for electrochemical capacitors [83-89]. Various synthesis routes including thermal oxidation of iron, electrospinning, hydrothermal process, and electrochemical anodizing have been reported recently for the formation of nanostructured iron oxides. The electrochemical anodizing of iron is one of the potential approaches that can contribute to all of the above fields owing to its low fabrication cost and possibility of synthesizing large area electrodes. It is also reported recently that nanotubular arrays prepared by anodizing of iron would have similar charge transport properties as that of TiO_2 nanotubes prepared by the same method [90]. Photoelectrochemical characterization of iron-based films with a similar band gap as TiO_2 has also been reported recently [91].

The use of organic electrolytes enables the formation of thick porous anodic films with high growth efficiency on iron and stainless steel and improves the uniformity of the self-ordered porous or nanotubular array as well as the thickening of the anodic films on valve metals. Hence, for the efficient fabrication of nanoporous and nanotubular anodic oxide films on iron at high efficiency, understanding of growth behavior of the porous films and the inter-relationship between structure, composition, and morphology of the anodic films on iron is of crucial importance [80].

1.4 Formation of anodic films on magnesium

Magnesium and its alloys have many outstanding properties such as low density, high specific strength, high heat conductivity, low heat capacity, recyclability, and non-toxicity. These properties are attractive to many technologies, particularly in the aerospace, automotive, and electronics industries and therefore, magnesium and its alloys are considered alternative to aluminum alloys. However, magnesium is one of the metals which bear stain most easily because of its low electrochemical potential region where metallic magnesium can exist in the wet environment. Thus, magnesium metal is thermodynamically very unstable and easily corrode in water as shown by the potential-pH diagram in **Fig. 1.6** [92].

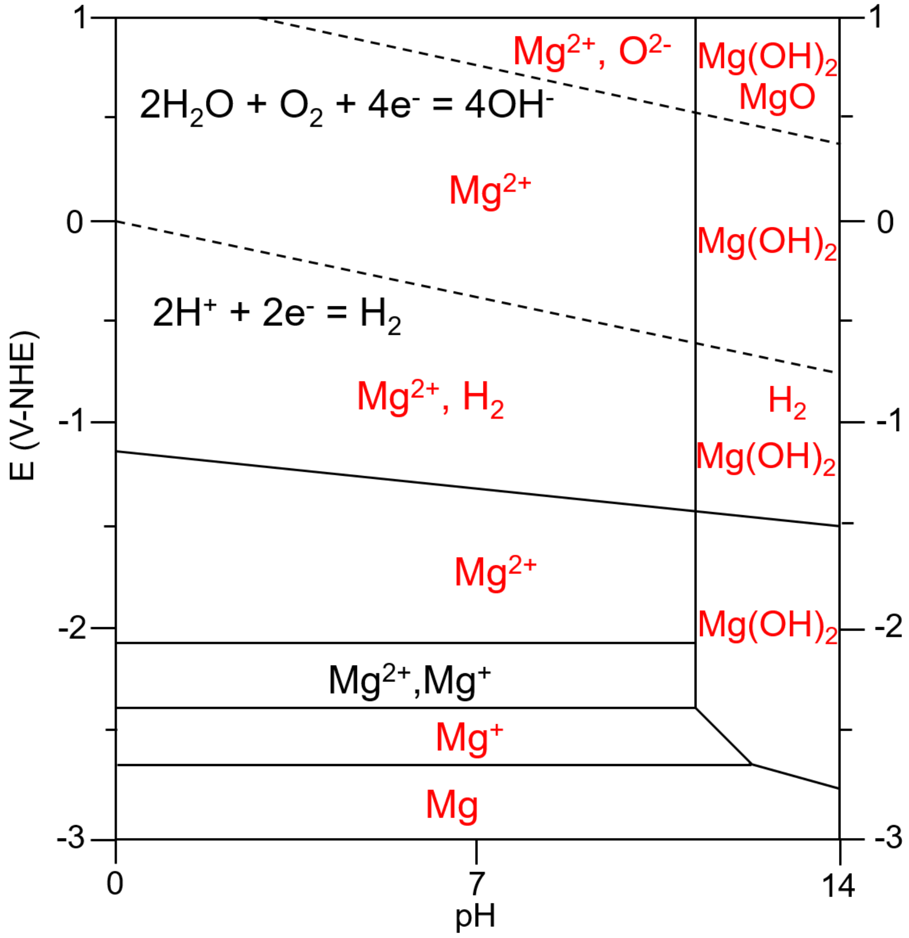

Figure 1.6 Potential-pH diagram indicating the electrochemical behaviour of magnesium in water at 298 K [92].

Most of the electrochemical reactions have a negative standard equilibrium potential, E_o, suggesting that they can be an anodic process relative to an electrochemical hydrogen process in the corrosion of Mg [93].

$$Mg \rightleftarrows Mg^{2+} + 2e^- \qquad E_o = -2.363\ V \qquad (1\text{-}3)$$

$$Mg + 2OH^- \rightleftarrows Mg(OH)_2 + 2e- \qquad E_o = -2.689\ V \qquad (1\text{-}4)$$

$$Mg + 2H_2O \rightleftarrows Mg(OH)_2 + e^- \qquad E_o = -1.065\ V \qquad (1\text{-}5)$$

These reactions indicate that magnesium in natural environments has a great tendency to transform into its oxidized states. Therefore, magnesium surface tends to be rapidly oxidized on exposure to water or oxygen, forming an oxide or hydroxide surface layer. The poor corrosion resistance of magnesium in aqueous electrolytes also limits their wide applications window. Without effective solutions of magnesium corrosion, further expansion of magnesium and its alloys applications appears to be unlikely [94-95]. Therefore, various surface treatments including anodizing have been applied to provide protection against corrosion [96-99].

As mentioned above, anodic films are contaminated with electrolyte-derived species, therefore, most recent studies focused on anodizing of magnesium and its alloys in environmental friendly electrolytes containing small concentrations of various additives such as Na_3PO_4, $Al(OH)_3$, Na_2SiO_3. Their concentrations significantly affect the properties and growth behavior of anodic films [100-103]. However, despite many studies on anodizing of magnesium and its alloys, much less is known about the morphology, composition, growth mechanism of barrier-type anodic films on magnesium compared with anodic films on many other metals.

1.5 Anodizing in fluoride-containing organic electrolytes

Extensive studies on the formation of titanium oxide nanotubes in HF-based aqueous electrolytes showed that nanotubes could be grown only up to few hundreds of nm, consequently reducing the growth efficiency. This limited growth may be assumed to be the result of fast dissolution process than the formation of an oxide film by chemical oxidation in these electrolytes. Thus, nanotube length is limited to 500 nm for acidic and 2µm for neutral aqueous electrolytes [63]. In contrast, nanotubes of 1mm thickness are reported at 60V in ethylene glycol electrolytes containing 0.5 wt. % ammonium fluoride and 3 % water [104]. Therefore, organic electrolytes with low conductivity compared with aqueous electrolytes allow the growth of nanotubes with highest efficiencies and with high degree of ordering. In addition to organic electrolytes, nanotubes growth rates on titanium are also determined by a balance between water and fluoride concentration. High fluoride concentration (> 0.1 mol dm^{-3} ammonium fluoride) enhances the dissolution of nanotubes, while the small addition of water to organic electrolytes allows sufficient rate of oxidation. In this regards, most recent studies have focused on the formation of nanoporous and nanotubular anodic films on Ti, Zr, Fe, and Mg in fluoride and water-containing glycerol/ethylene glycol electrolytes. These studies revealed that water concentration significantly affects the resultant film morphology and growth efficiency. For instance, anodizing of iron in aqueous electrolytes produces soluble ferrates at high potential, and it is difficult to produce thick porous film on iron in aqueous electrolyte [105], whereas fluoride containing organic electrolytes enables the formation of thick porous film on iron and it is recently reported that growth efficiency of anodic film on iron is significantly improved at low water concentrations [106]. Likewise, the corrosion rate of magnesium decreased with an increasing concentration of ethylene glycol and by the addition of fluoride that reacts with magnesium to form the protective surface film. Song *et al.* reported that ethylene glycol is almost inert to magnesium and corrosion of magnesium in ethylene glycol electrolyte is strongly related to the amount of water as shown in **Fig. 1.7**. This may be due to the high resistivity of ethylene glycol, which is almost 40 times higher than ASTM type II water [107]. Thus, the addition of water strongly influences the growth behavior of anodic film on magnesium surface in ethylene glycol electrolyte.

Fortunately, recent formation of barrier-type and porous-type films at high growth efficiency on iron, magnesium and ZE41 magnesium alloy in ethylene glycol electrolyte containing fluoride and water provides an opportunity to understand the growth behavior of anodic films on magnesium [106, 108]. However, despite the recent formation of anodic films in organic electrolytes, only a few attempts has been made to understand the formation behavior of fluoride-based anodic films on iron and magnesium in non-aqueous electrolytes.

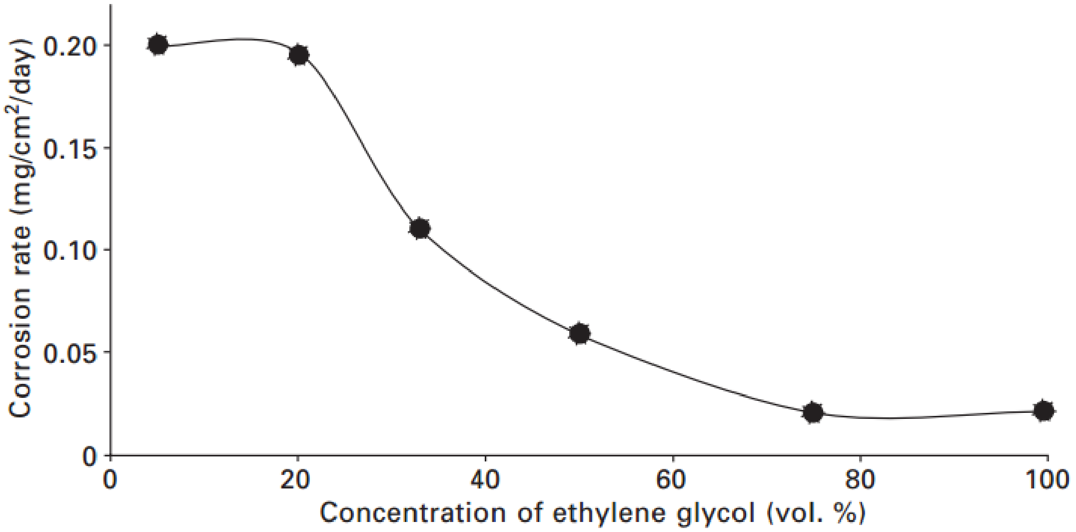

Figure 1.7 Corrosion rate of pure magnesium as a function of ethylene glycol concentration in water at ambient temperature [107].

1.6 Objective of the present work

As described above, both iron and magnesium are important practical metals. Surface treatments of these metals are always necessary to prevent these metals from corrosion in practical environments. The formation of nanostructured anodic films on these metals is also interesting to provide various surface functionalities. Anodizing studies on iron was triggered in 2006 when Prakasam *et al.* reported the formation of nanoporous anodic films on iron in fluoride-containing organic electrolytes [76]. Anodizing of magnesium have been studied for several decades and practically used, but the growth mechanism of the anodic films on both iron and magnesium has not yet well understood. Detailed understanding of the film growth mechanism is of importance for the control of nanostructured morphology of the anodic films, and for the improvement of the film uniformity and growth efficiency. Therefore, in the present study, fundamental aspects of formation behavior of anodic films on iron and magnesium in fluoride-containing ethylene glycol electrolytes are examined at several water concentrations.

Since, barrier and porous film morphologies are strongly dependent on interfacial processes at the film/electrolyte interface and porous film growth proceeds either due to field-assisted dissolution or field-assisted flow. Thus, understanding of the role of the electric field in the film/electrolyte interface process is crucial to control the film morphology. In this thesis study, the growth behavior of anodic films on iron and magnesium was examined with particular attention paying to the ionic transport and interfacial processes, which control the film morphology. These fundamental aspects of formation behavior for the anodic films on iron and magnesium were investigated mainly by employing high-resolution transmission electron microscopy (TEM) and Rutherford backscattering spectroscopy (RBS) for the better understanding of correlation between film morphology and composition.

1.7 Thesis outline

This thesis consists of total six chapters.

Chapter 1 describes the brief introduction of anodizing of iron and magnesium, as well as science behind the formation of various types of anodic films and their growth mechanisms.

Chapter 2 elaborates the details of experimental conditions and materials employed for the fabrication of anodic films. The major characterization techniques employed are also briefly introduced.

In Chapter 3, morphology, composition, and structure of the anodic films on the iron sheet in the ethylene glycol electrolyte at several water concentrations were examined for a better understanding of the porous anodic film growth. In addition, the effects of formation voltage and fluoride enrichment on the formation of nanotubes were also investigated at optimum water concentration.

Chapter 4 explains the mechanistic study of the barrier and porous-type films formation on magnetron-sputtered iron films at different sweep rates at low water concentration. This chapter also addresses the film growth efficiency, estimated by Rutherford backscattering spectroscopy (RBS) at different sweep rates. Field-assisted dissolution of anodic film on iron and impact of electric field on film formation and dissolution will also be discussed in this chapter.

Chapter 5 addresses the uniform formation of the barrier-type anodic film on magnetron-sputtered magnesium films in phosphate-containing ethylene glycol and aqueous electrolytes. This chapter explains the influence of water concentration and phosphate addition on the film structure, composition, and growth efficiency. Based on TEM and RBS analysis, the growth mechanism of barrier-type anodic film on magnesium will be discussed.

Chapter 6 contains the summary of the results of the previous chapters. This chapter also includes suggestions for future work.

References:

[1] F. Keller, M. S. Hunter, D. L. Robinson, *J. Electrochem. Soc.*, **100**, 411 (1953).

[2] H. Masuda, K. Fukuda, *Science*, **268**, 1466 (1995).

[3] S. Ono, M. Saito, M. Ishiguro, H. Asoh, *J. Electrochem. Soc.*, **151**, B473 (2004).

[4] J. P. S. Pringle, *J. Electrochem. Soc.*, **119**, 482 (1972).

[5] L. Young, Anodic Oxide Films, *Academic Press*, *London and New York*, (1961).

[6] O. Jessensky, F. Müller, U. Gösele, *J. Electrochem. Soc.*, **145**, 3735 (1998).

[7] J. P. O'Sullivan, G. C. Wood, *Proc. R. Soc. Lond. A,* **317**, 511 (1970).

[8] S. J. Garcia-Vergara, L. Iglesias-Rubianes, C. E. Blanco-Pinzon, P. Skeldon, G. E. Thompson, P. Campestrini, *Proc. R. Soc. A,* **462**, 2345 (2006).

[9] J. E. Houser, and K. R. Hebert, *Nature Mater.*, **8**, 415 (2009).

[10] G. E. Thompson, R. C. Furneaux, G. C. Wood, J. A. Richardson, J. S. Goode, *Nature,* **272**, 433 (1978).

[11] G. E. Thompson, Y. Xu, P. Skeldon, K. Shimizu, S. H. Han, G. C. Wood, *Phil. Mag. B***,** **55**, 651 (1987).

[12] J. P. S. Pringle, *J. Electrochem. Soc.*, **121**, 865 (1974).

[13] Q. Lu, P. Skeldon, G. E. Thompson, D. Masheder, H. Habazaki, K. Shimizu, *Corros. Sci.*, **46**, 2817 (2004).

[14] G. E. Thompson, G. C. Wood, *Corrosion: Aqueous Processes and Passive Films* (Tretise on Materials Science and Technology, Vol. **23**. J. C. Scully, Ed., (Academic Press Inc. London, (1983).

[15] P. Skeldon, K. Shimizu, G. E. Thompson, G. C. Wood, *Thin Solid Film,* **123**, 127 (1985).

[16] S. Ono, K. Kuramochi, Haditaka Asoh, *Corros Sci.*, **51**, 1513 (2009).

[17] J. A. Richardson, G. C. Wood, *Corros. Sci.,* **10**, 313 (1970).

[18] J. A. Richardson, G. C. Wood, W. H. Sutton, *Thin Solid Films,* **16**, 99 (1973).

[19] J. P. O'Sullivan, G. C. Wood, *Proc. Roy. Soc. Lond. A,* **317**, 511 (1970).

[20] R. W. Franklin, *Nature*, **180**, 1470 (1957).

[21] D. J. Stirland, R. W. Bicknell, *J. Electrochem. Soc.*, **106**, 481 (1959).

[22] J. S. L. Leach, P. Neufeld, *Corros. Sci.,* **9**, 413 (1969).

[23] G. A. Dorsey, *J. Electrochem. Soc.*, **113**, 169 (1966).

[24] H. Takahashi, M. Nagayama, *Electrochim. Acta*, **23**, 729 (1978).

[25] Y. Xu, G. E. Thompson, G. C. Wood, *Trans. IMF,* **63**, 98 (1985).

[26] P. Skeldon, K. Shimizu, G. E. Thompson, G. C. Wood, *Thin Solid Films*, **123**, 127 (1985).

[27] K. Shimizu, K. Kobayashi, G. E. Thompson, P. Skeldon, G. C. Wood, *Phil. Mag. B,* **73**, 461 (1996).

[28] P. Skeldon, K. Shimim, G.E. Thompson, G.C. Wood, *Surf. Interface Anal.,* **5**, 247 (1983).

[29] H.Habazaki, P. Skeldon, K. Shimizu, G.E.Thompson, G.C. Wood, *Corros. Sci.*, **37**, 1497 (1995).

[30] K. Shimizu, G.C.Wood, G.E. thompson, *Thin Solid Films*, **85**, 53 (1981).

[31] K. Shimizu, K. Kobayashi, G. E. Thompson, G. C. Wood, P. Skeldon, *Philos. Trans. R. Soc. Lond. A,* **354**, 213 (1996).

[32] K. Shimizu, G.M. Brown, H. Habazaki, K. Kobayashi, P. Skeldon, G.E.Thompson, G.C. Wood, , *Corros. Sci.,* **41**, 1971 (1999).

[33] H. Takahashi, K. Fujimoto, M.Nagayama, *J. Electrochem. Soc.*, **135**, 1349 (1988).

[34] M. F. ABD. Rabbo, J. A. Richardson, G. C. Wood, *Corros. Sci.,* **16**, 689 (1976).

[35] P. Hoar, N. F. Mott, *J. Phys. Chem. Solids,* **9**, 97 (1959).

[36] A. J. Brock, G. C. Wood, *Electrochim. Acta,* **12**, 395 (1967).

[37] H. Habazaki, M. Uozumi, H. Konno, K. Shimizu, P. Skeldon, G.C. Thompson, *Corros. Sci.*, **45**, 2063 (2003).

[38] J.A. Davies, B. Domeij, J.P.S. Pringle, F. Brown, *J. Electrochem. Soc.*, **112,** 675 (1965).

[39] A. Guntherschultze, H. Betz, Z. *Phys.*, **92**, 367 (1934).

[40] J. E. Lewis, R. C. Plumb, *J. Electrochem. Soc.*, **105**, 496 (1958).

[41] J. M. Diggle, T. C. Downle, C. F. Goulding, *J. Electrochem. Soc.,* **116**, 1347 (1969).

[42] G. Bailey, Ph.D. Thesis, *University of Manchester* (1978).

[43] W. J. Bernard, *J. Electrochem. Soc.*, **109**, 1082 (1962).

[44] G. C. Wood, P. Skeldon, G. E. Thompson, K. Shimizu, *J. Electrochem. Soc.,* **143**, 74 (1996).

[45] W. J. Bernard, J. J. Randall, *J. Electrochem. Soc.*, **20**, 653 (1975).

[46] G. E. Thompson, *Thin Solid Films,* **297**, 192 (1997).

[47] J. E. Houser, K.R. Hebert, *Nat. Mater.,* **8**, 415 (2009).

[48] T. P. Hoar, N.F. Mott, *J. Phys. Chem. Solids,* **9**, 97 (1959).

[49] C. Cherki, J. Siejka, *J. Electrochem. Soc.*, **120**, 784 (1973).

[50] N. Sato, *Electrochim. Acta,* **16**, 1683 (1971).

[51] J. Siejka, C. Ortega, *J. Electrochem. Soc.*, **124**, 883 (1977).

[52] V. P. Parkhutik, V. I. Shershulsky, *J. Phys. D: Appl. Phys.*, **25**, 1258 (1992).

[53] G. K. Singh, A. A. Golovin, I. S. Aranson, V. M. Vinokur, *Europhys. Let.,* **70**, 836 (2005).

[54] S. J. Garcia-Vergara, P. Skeldon, G. E. Thompson, H. Habazaki, *Corros. Sci.,* **49**, 3772 (2007).

[55] S. J. Garcia-Vergara, P. Skeldon, G. E. Thompson, H. Habazaki, *Electrochim. Acta,* **52**, 681 (2006).

[56] P. Skeldon, G. E. Thompson, S. J. Garcia-Vergara, L. Iglesias-Rubianes, C. E. Blanco-Pinzon, *Electrochem. Solid State Let.,* **9**, B47 (2006).

[57] J. M. Macak, P. Schmuki, *Electrochim. Acta,* **52**, 1258 (2006).

[58] S. Berger, J. Faltenbacher, S. Bauer, P. Schmuki, *Phys. Status Solidi Rapid Res. Lett.,* **2**, 102 (2008).

[59] J. Z. Ou, R.A. Rani, M.H. Ham, M. R. Field, Y. Zhang, H. Zheng, P. Reece, S. Zhuiykov, S. Sriram, M. Bhaskaran, R.B. Kanee, K. Kalantar-Zadeh, *ACSNano,* **6**, 4045 (2012).

[60] W. Wei, J.M. Macak, P. Schmuki, *Electrochem. Commun.*, **10**, 428 (2008).

[61] R. R. Rangaraju, A. Panday, K.S. Raja, M. Misra, *J. Phys. D. Appl. Phys.,* **42**, 135303 (2009).

[62] M. Assefpour-Dezfuly, C. Vlachos, E. H. Andrews, *J. of Mater. Sci.,* **19**, 3626 (1984).

[63] P. Roy, S. Berger, P. Schmuki, *Angew. Chem. Int. Ed.*, **50**, 2904 (2011).

[64] G.A. Crawford, N. Chawla, J.E. Houston, *J. Mech. Behav. Biomed. Mater.*, **2**, 580 (2009).

[65] M. W. Park, K.Y. Chun, *Electron. Mater. Let.,* **5**, 7 (2009).

[66] V. Zwilling, E. Darque-Ceretti, A. Boutry-Forveille, D. David, M.Y. Perrin, M. Aucouturier, *Surf. Interf. Anal.,* **27**, 629 (1999).

[67] M. Macak, H. Tsuchiya, L. Taveira, S. Aldabergerova, P. Schmuki, *Angew. Chem. Int. Ed.*, **44**, 7463 (2005).

[68] A. Ghicov, S. P. Albu, J. M. Macak, P. Schmuki, *Phys. Status Solidi Rapid Res. Lett.,* **1**, R65 (2007).

[69] A. Ghicov, H. Tsuchiya, J. M. Macak, P. Schmuki, *Electrochem. Commun.*, **7**, 505 (2005).

[70] H. Tsuchiya, J.M. Macak, L. Taveira, E. Balaur, A. Ghicov, K. Sirotna, P. Schmuki, *Electrochem. Commun.*, **7**, 576 (2005).

[71] F. Muratore, A. Baron-Wiechec, A. Gholinia, T. Hashimoto, P. Skeldon, G.E. Thompson, *Electrochim. Acta*, **58**, 389 (2011).

[72] A. Valota, D.J. LeClere, P. Skeldon, M. Curioni, T. Hashimoto, S. Berger, J. Kunze, P. Schmuki, G.E. Thompson, *Electrochim. Acta*, **54**, 4321 (2009).

[73] S. Berger, Sergiu P. Albu, Felix Schmidt-Stein, Helga Hildebrand, Patrik Schmuki, John S. Hammond, Dennis F. Paul, Stefan Reichlmaier, *Surf. Sci.*, **605**, L57 (2011).

[74] H. Habazaki, K. Fushimi, K. Shimizu, P. Skeldon, G.E. Thompson, *Electrochem. Commun.*, **9**, 1222 (2007).

[75] S. P. Albu, A. Ghicov, S. Aldabergenova, P. Drechsel, D. LeClere, G.E. Thompson, J.M. Macak, P. Schmuki, *Adv. Mater.*, **20**, 4135 (2008).

[76] H. E. Prakasam, O. K. Varghese, M. Paulose, G. K. Mor, C. A. Grimes, *Nanotechnol.*, **17**, 4285 (2006).

[77] S. P. Albu, A. Ghico, P. Schmuki, *Phys. Status Solidi Rapid Res. Lett.*, **3**, 64 (2009).

[78] K. Mohapatra, S. E. John, S. Banerjee, M. Misra, *Chem. Mater.*, **21**, 3048 (2009).

[79] R. R. Rangaraju, A. Panday, K. S. Raja, M. Misra, *J. Phys. D: Appl. Phys.*, **42**, 135303 (2009).

[80] H. Habazaki, Y. Konno, Y. Aoki, P. Skeldon and G. E. Thompson, *J. Phys. Chem. C*, **114**, 18853 (2010).

[81] R. R. Rangaraju, K. S. Raja, A. Panday, M. Misra, *Electrochim. Acta*, **55**, 785 (2010).

[82] Y. Konno, S. Yang, E. Tsuji, Y. Aoki, P. Skeldon, G. E. Thompson, H. Habazaki, *ECS Trans.*, **50**, 183 (2013).

[83] K. L. Hardee, A. J. Bard, *J. Electrochem. Soc.*, **123,** 1024 **(**1976).

[84] N. Beermann, L. Vayssieres, S. E. Lindquist, A. Hagfeldt, *J. Electrochem. Soc.*, **147** 2456 (2000).

[85] J. H. Kennedy, K. W. Frese, *J. Electrochem. Soc.*, **125** 709 (1978).

[86] H. T. Sun, C. Cantalini, M. Faccio, M. Pelino, *Thin Solid Films*, **269**, 97 (1995).

[87] M. Pelino, C. Cantalini, H. T. Sun, M. Faccio, *Sensors and Actuators B-Chemical*, **46**, 186 (1998).

[88] F. Jiao, B. Yue, K. Zhu, D. Y Zhao, H. Y. He, *Chem. Let.*, **32**, 770 (2003).

[89] S. Piazza, M. Sperandeo, C. Sunseri, F. Di Quarto, Corros. Sci., **6**, 831 (2004).

[90] K. S. Raja, M. Misra, V. K. Mahajan, T. Gandhi, P. Pillai and S. K. Mohapatra, *J. Power Sources,* **161,** 1450 (2006).

[91] M. Santamaria, S. Terracina & Y. Konno & H. Habazaki & F. Di Quarto, *J Solid State Electrochem.*, **17**, 3005 (2013).

[92] M. M. Avedesian, H. Baker, ASM specialty handbook, Magnesium and Magnesium Alloys, ASM International (1999).

[93] G. G. Perrault, *Journal of Electroanal. Chem.,* **51**, 107 (1974).

[94] G. L. Makar, J. Kruger, *International Materials Reviews*, **38 (3)**, 138 (1993).

[95] H. Alves, U. Koster, E. Aghion, D. Eliezer, *Materials Technology: Advanced Performance Materials,* **16 (2)**, 110 (2001).

[96] L. Zhu, G. Song, *Surf. Coat. Technol. Reviews Advanced*, **200**, 3834 (2006).

[97] C. Blawert, W. Dietzel, E. Ghali, G. Song, *Adv. Eng. Mater.,* **8**, 511 (2006).

[98] M. Santamaria, F. Di Quarto, S. Zanna, P. Marcus, *Electrochim. Acta*, **56**, 10533 (2011).

[99] M.-C. Zhao, M. Liu, G.L. Song, A. Atrens, *Corros. Sci.*, **50**, 3168 (2008).

[100] A. Yabuki, M. Sakai, *Corros. Sci.,* **51**, 793 (2009).

[101] S. Ono, K. Asami, T. Osaka, N. Masuko, *J. Electrochem. Soc.*, **143**, L62 (1996).

[102] O. Khaselev, D, Weiss, J, Yahalom, *J. Electrochem. Soc.*, **146**, 1757 (1999).

[103] Y. Liu, Z. Wei, F. Yang, Z. Zhang, *J. Alloys Compd.,* **509**, 6440 (2011).

[104] M. Paulose, H. E. Prakasam, O. K. Varghese, L. Peng, K. C. Popat, G. K. Mor, T. A. Desai, C. A. Grimes, *J. Phys. Chem. C,* **111**, 14993 (2007).

[105] F. Beck, R. Kaus, M. Oberst, *Electrochim. Acta,* **30(2)**, 173 (1985).

[106] K. Y. Xie, M. Guo, H. T. Huang, Y. X. Liu, *Corros. Sci.*, **88**, 66 (2014).

[107] G. Song, D. StJohn, *Mater. Corros.,* **56**, 15 (2005).

[108] H. Habazaki, F. Kataoka, K. Shahzad, E. Tsuji, Y. Aoki, S. Nagata, P. Skeldon, G.E. Thompson, *Electrochim. Acta*, **179**, 402 (2015).

Chapter 2

Experimental Methods and Materials

2.1 Introduction

This chapter expounds the experimental methods and materials employed for anodizing and the characterization techniques used. The materials preparation prior to and after anodizing as well as specimens cleaning techniques are also discussed. A brief description and purpose of the characterization techniques for the analysis of anodic films on iron and magnesium, such as glow discharge optical emission spectroscopy (GDOES), Rutherford backscattering spectroscopy (RBS), X-ray diffraction (XRD), transmission electron microscopy (TEM), and scanning electron microscopy (SEM) are also included in this chapter.

2.2 Materials used for anodizing

Thin iron sheet and magnetron-sputtered thin films of iron and magnesium were used as a substrate for the growth of barrier-type and porous-type anodic films. The substrates used for the sputter deposition were glass and anodized aluminum substrates, which were prepared carefully to produce clean and flat surface. Glass substrate of dimensions 60 x 80 mm was cleaned in an organic degreasing solution by heating the solution to ~333 K for 15 minutes, followed by rinsing in water for 15 minutes and finally dried. Electropolishing of aluminum sheet was performed in a solution of perchloric acid (60 %)/ethanol (99.5%) purchased from Kanto Chemical Co., Inc. and then subsequent anodizing in ammonium pentaborate solution. Details are described below.

2.2.1 Electropolishing of aluminum sheet

Electropolishing of ultrasonically cleaned aluminum sheet was carried out in 60 % perchloric acid/ethanol solution in 1:4 volume ratio. This solution is vulnerable due to its aggressiveness and oxidizing nature and should be used below 283 K. About 800 mL of ethanol was obtained in 1 L beaker containing magnetic stirrer and surrounded by ice in a bath to maintain the temperature of the beaker below 283 K. 200 mL of perchloric acid was slowly added to a beaker containing ethanol and magnetic stirrer. The electropolishing was carried out in a two electrode-cell in a fume cupboard with aluminum sheets serving as working and counter electrode. Electropolishing was performed at optimized 20V applied from a power source. Stirring of the solution was also performed during electropolishing. The temperature of the solution was maintained below 283 K during electropolishing. The temperature of electropolishing was carefully measured with conventional thermometer immersed in the solution. Electropolishing was suspended when the temperature of the solution was raised to 283 K and restarted when the solution temperature was reached to 273 K. Electropolishing was carried out for 4-5 minutes. After electropolishing, the specimen was removed and rinsed thoroughly first in ethanol and then in deionized water and dried in a cool air stream. The schematic of electropolishing setup is shown in **Fig. 2.1**.

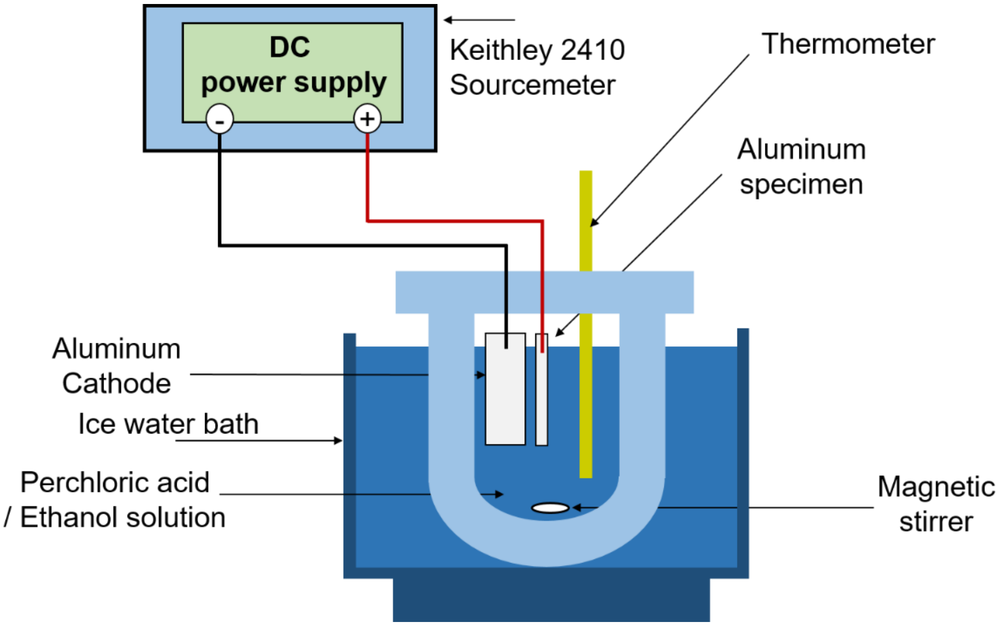

Figure 2.1 Schematic representation of electropolishing of aluminum.

2.2.2 Anodizing of aluminum in ammonium pentaborate solution

After electropolishing, anodizing of aluminum sheets was conducted in 0.1 mol dm^{-3} ammonium pentaborate solution to 200 V employing a current density of 50 A m^{-2} at 293 K. The voltage-time responses recorded during anodizing indicating reproducibility are shown in **Fig. 2.2**.

The potential rose linearly to 200 V with a slope of ~ 2.3 V s^{-1}. Anodizing was performed in two electrode-cell with aluminum as working and counter electrode. After anodizing, the specimen was rinsed thoroughly with deionized water and then dried in a stream of air.

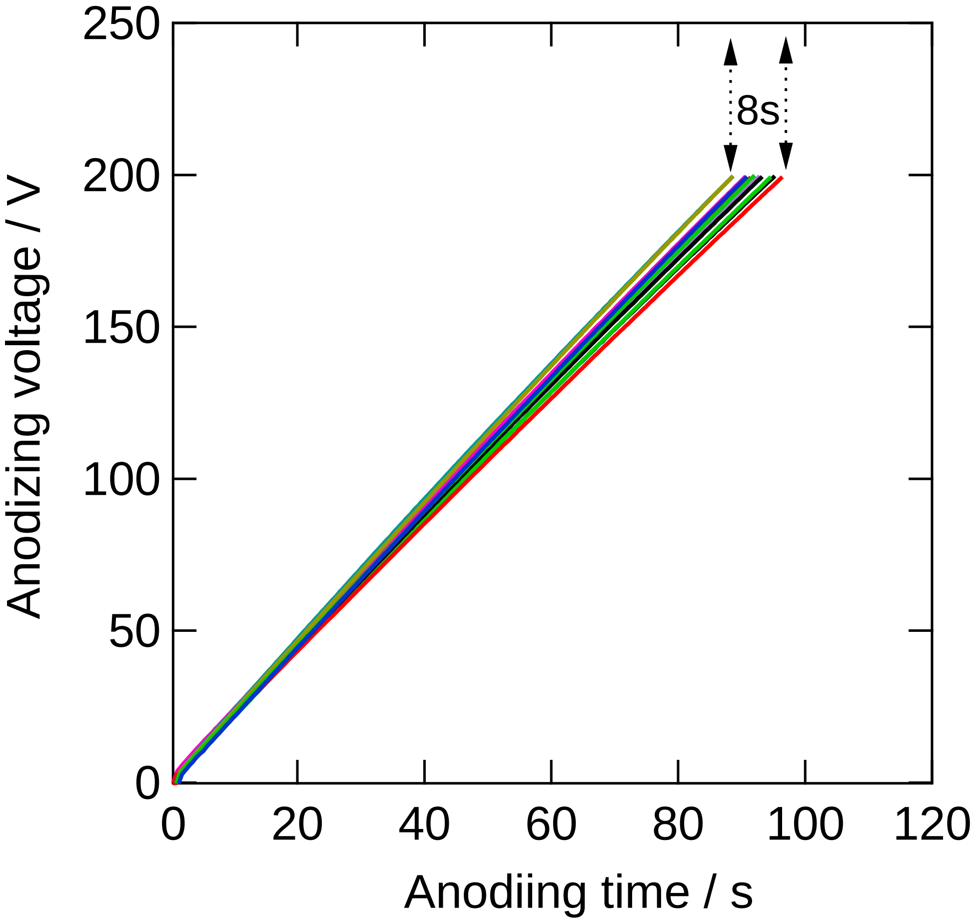

Figure 2.2 *V-t* responses for electropolished aluminum substrate anodized to 200 V at 50 Am^{-2} in 0.1 M ammonium pentaborate solution at 293 K.

2.2.3 DC magnetron sputtering of iron and magnesium metals

DC magnetron sputtering is a technique of depositing a thin film of metal, alloy or compound. This physical vapor deposition process controllably transfers atoms from a source (target) through a gas phase to a substrate where film formation and growth proceed atomistically. The process involves ejection of atomized materials from target owing to bombardment by gaseous ions or neutral particles and subsequent deposition of atomized material onto a suitable substrate. A schematic representation of DC sputtering process is shown in **Fig. 2.3**.

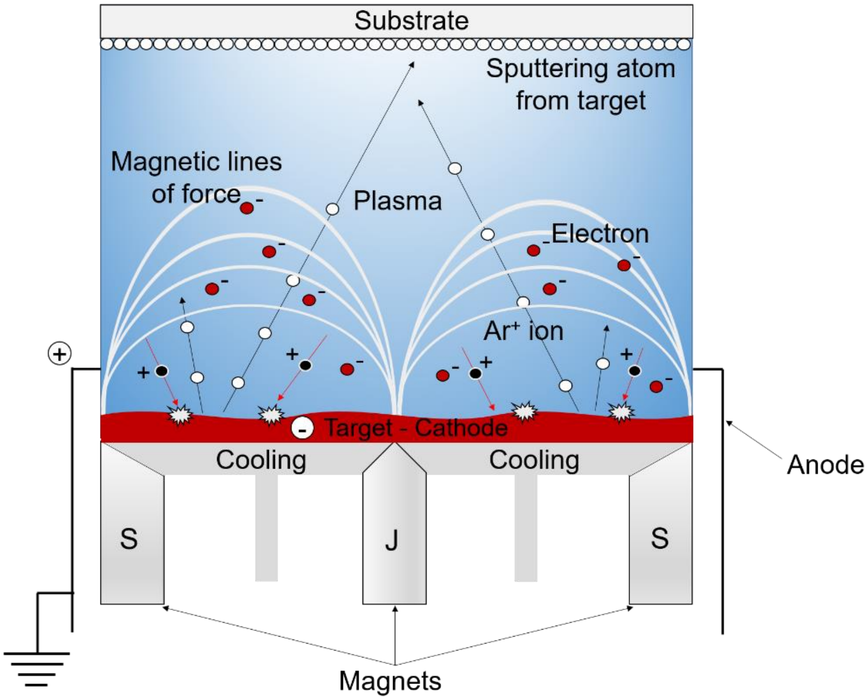

Figure 2.3 Diagram showing the magnetron sputtering [1].

The main purpose of the use of magnetron-sputtered films instead of bulk iron and magnesium metals was to avoid the influence of second phase elements present in bulk magnesium and iron and to simplify the characterization of the anodized specimens. As sputtering is performed under high vacuum, it eliminates the possibility of inclusion of any impurity and produces very high purity single phase metal. Iron and magnesium thin films were magnetron-sputtered employing a Shimadzu, SP-2C DC magnetron sputtering facilities onto the glass or anodized aluminum substrates. The latter substrate was used for RBS and TEM analysis. Sputtering was carried out employing a magnesium target (99.99 % purity) and 6 mm in thickness and 100 mm in diameter or an iron disk of 99.99% purity of 0.5 mm thickness and 100 mm diameter bonded on a copper backing plate.

DC magnetron sputtering was performed at 0.5 A under an argon pressure of ~3 Pa after evacuating the chamber to 5 x 10^{-5} Pa. The thicknesses of magnetron-sputtered iron and magnesium films were controlled by the time of sputtering. Iron and magnesium films were deposited at a rate of ~ 45 nm min^{-1} and ~75 nm min^{-1} respectively on respective substrates. After required time of sputtering, the current applied to target materials was switched off, and substrate was then cooled in vacuum. The chamber pressure was raised to atmospheric pressure by the introduction of nitrogen gas and the specimens were removed from the sputtering chamber and transferred to vacuum desiccator in order to protect the films from moisture.

2.2.4 Mechanical polishing of iron sheet

Iron sheet of 0.3 mm thickness and purity of 99.99% was obtained from the Nilaco Corporation, Japan. The high purity iron sheet was cut to the size of 10 x 20 mm using a Sunhayato PC-210 hand cutter. Then, the surface of the iron sheet was mechanically polished with 1500 grit SiC paper followed by polishing using Al_2O_3 abrasives of 3 µm diameter and ultrasonically degreased in acetone.

2.3 Anodizing of iron and magnesium

2.3.1 Iron anodizing

Anodic films on mechanically polished and magnetron-sputtered iron were formed either by potentiodynamic anodizing (by varying the sweep rate) or galvanostatically (constant current) to the selected voltages or current densities, respectively, in ethylene glycol (EG) electrolytes containing small amounts of water and ammonium fluoride. Potentiodynamic anodizing of iron specimens was carried out in two electrode system with a platinum sheet as a cathode and iron specimen as an anode. The voltage-dependent current and time-dependent voltage behavior was recorded employing a Keithley 2410 sourcemeter, which was also used as a power source. The temperature of the electrolyte was usually kept at 293 K. After anodizing, the specimens were ultrasonically washed in ethylene glycol, followed by rinsing in acetone and then dried in an air stream. A schematic of the anodizing process is shown in **Fig. 2.4**.

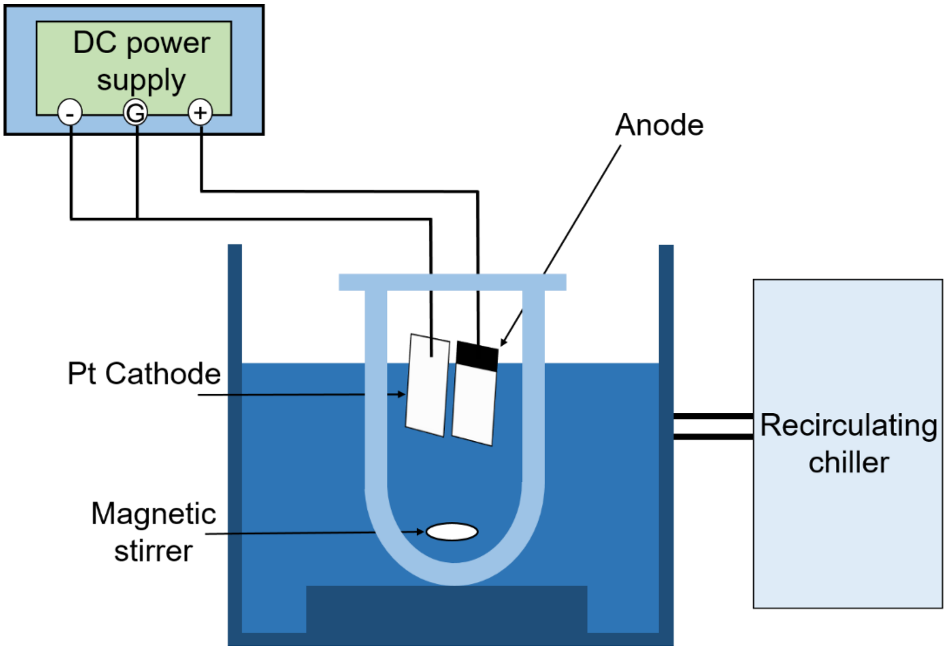

Figure 2.4 Schematic illustration of the anodizing apparatus used in this study, indicating two electrodes anodizing cell in a large cooling vessel and chiller.

2.3.2 Magnesium anodizing

Magnesium anodizing for the growth of barrier-type anodic film was performed on magnetron-sputtered magnesium thin films. Anodizing of the deposited magnesium films was carried out in a two electrode-cell with a platinum sheet as a counter electrode at a constant current density of 10 Am^{-2} to the selected voltages. The electrolytes used were ethylene glycol containing 0.1 mol dm^{-3} ammonium fluoride and various concentrations of water with or without the addition of 0.1 mol dm^{-3} dipotassium hydrogen phosphate for the growth of barrier-type films at 293 K.

2.4 Characterization techniques

2.4.1 Glow discharge optical emission spectrometry

Glow discharge optical emission spectroscopy (GDOES) is an important technique for chemical analysis of bulk solids, for elemental surface analysis and for the depth profiling of thin films. The rapid analysis without using an ultrahigh vacuum, high sensitivity to all elements of periodic table including hydrogen, high accuracy, and with excellent depth resolution, it is possible to obtain the information from nanometers to the few micrometers of film materials. GDOES has also proven its capability of rapid analysis of film thickness from a few nanometers up to several hundred micrometers, being suitable for depth profile analysis of both barrier-type and porous-type anodic films. A schematic illustration of GDOES process is shown in **Fig. 2.5**.

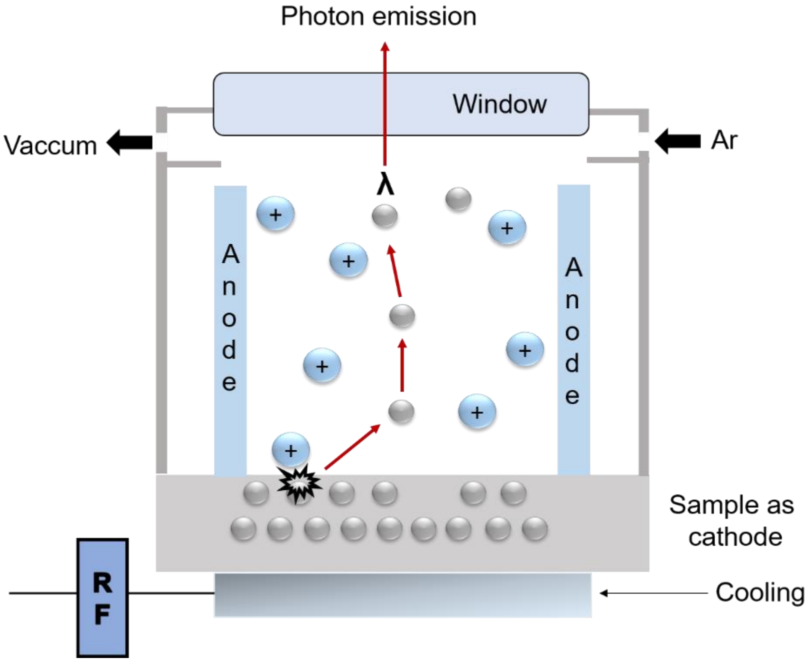

Figure 2.5 Schematic diagram illustrating GDOES sputtering and emission process.

In the present study, elemental depth profile analysis was performed using a Jobin-Yvon 5000 RF GDOES analyzer. The RF power of 13.56 MHz and 35 W was used for elemental depth profile analysis of anodized films formed on iron at various water concentrations. It is well known that fluorine atomic lines (F-I) as well as ionic lines (F-II) are hardly observed in the argon-glow discharge plasma, whereas they can be emitted by using neon plasma [2]. Therefore, porous anodic films on bulk iron were sputtered in a neon atmosphere of 1100 Pa to excite the most intense fluorine line of 685.6 nm instead of normally used argon gas when depth profile of fluorine was needed at a power of 50 W, with a data acquisition time of 0.05s. A copper anode of 4 mm diameter and a polychromator was employed for the detection of emission intensity from the sputtered elements. The wavelengths of the spectral lines used were 121.567, 165.701, 685.602, 130.217, 385.991 nm for hydrogen, carbon, fluorine, oxygen, iron respectively [3, 4].

2.4.2 Rutherford backscattering spectroscopy (RBS)

Rutherford backscattering spectroscopy (RBS) was used for quantitative analysis of film composition, density, thickness, and depth profiles of thin films near the surface region. The technique involve imposing a high energy alpha-particles usually helium (He^{2+}) at target (film) and measuring the energies of back scattered *He* ions. The following equations relates the energy of emergent ions to that of incident ions.

(2-1)

Where E_1 and E_o are the energy of emergent and incident ions and K_M is the kinematic factor.

(2-2)

It is obvious that energy ratio E_1/E_o or the kinematic factor after scattering depends only on the mass M_o of the projectile, the mass M of the target and the scattering angle θ. A schematic representation of RBS analysis is shown in **Fig. 2.6**, which shows that a beam of energetic ions, E_o is directed at the target, and the energies E_1, E_2, and E_3 of back-scattered ions are analyzed by means of a detector. In **Fig. 2.7a**, 400 nm thin iron-fluoride film, which undergoes He^{2+} ions bombardment and schematic of energy changes with depth are shown. Energy changes ($E_o \rightarrow E_1$) for scattering from iron and fluorine surface atoms are shown in **Fig. 2.7b**. The majority of helium ions penetrate the below the surface film and continuously lose energy at a linear rate ($E_o \rightarrow E_2$) with distance traversed. At any film depth, helium ions suffer an atomic collision. After the measurement of the number and energy of backscattered He^{2+} ion, information regarding the nature of elements present, their concentration, and depth distribution can be obtained without appreciably damaging the specimen.

In the present study, film compositions, thickness, densities, and current efficiencies estimated by RBS simulation of the anodic films formed on iron and magnesium were analyzed. Film thickness is first determined from TEM using the FIB-treated cross section of anodic film and then this film thickness was simulated by using RBS from atomic density (atom cm^{-3}) and TEM film thickness. RBS analysis was conducted by employing He^{2+} ion of 2.0 MeV energy supplied by a tandem-type accelerator at Tohoku University. Back-scattered ions were detected at

170° to the incident beam direction. The RBS data was simulated using XRUMP software [5, 6, 7].

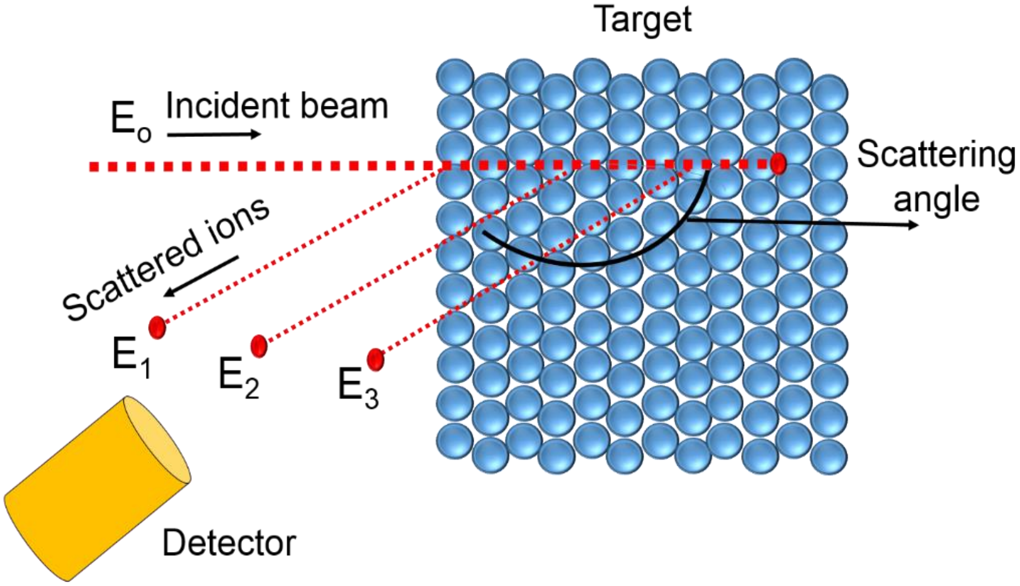

Figure 2.6 Schematic diagram of RBS analysis.

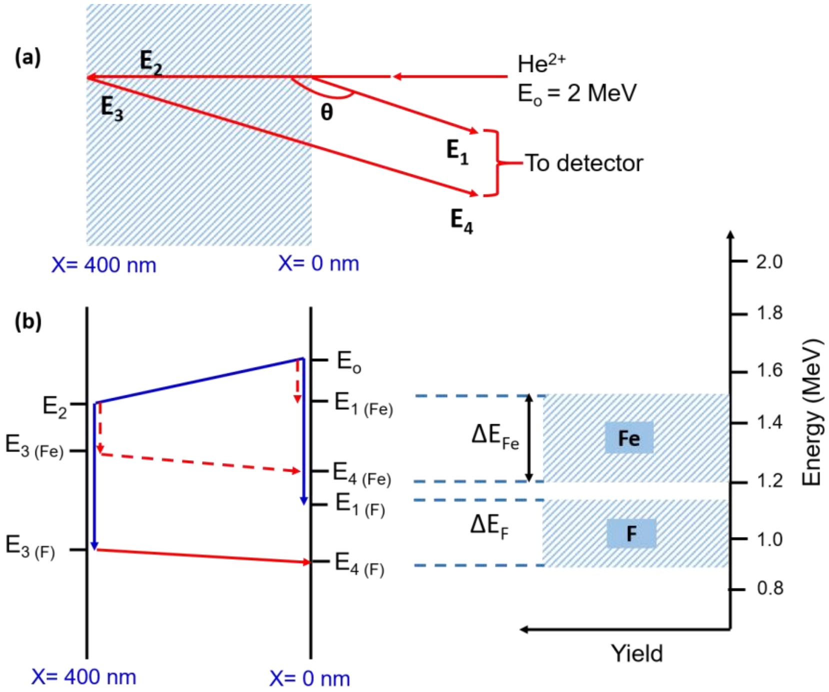

Figure 2.7 (a) Schematic illustration of geometry of scattering and notation of energies at front and back surfaces of a 400 nm-thin iron fluoride film and (b) change in the energy of He^{2+} ions during traveling a 400 nm-thin iron fluoride thin film.

2.4.3 X-ray diffraction (XRD)

The phases in the anodic films were identified by a Rigaku, RINT-2000 X-ray diffractometer using Cu Kα irradiation (λ = 0.15418 nm). The diffraction occurs only under conditions of constructive interference when Bragg's law is satisfied. In bulk XRD mode, also known as θ-2θ or Bragg-Brentano geometry, the incident angle of X-ray onto the specimen surface is maintained at the same angle as the detecting angle. However, this mode produces a weak signal from a surface thin film and the intense signal from the substrate. For the analysis of thin anodic films in this study, grazing incidence XRD (GIXRD) was used to minimize the contribution of the substrate material, in which the incidence angle (alpha) is fixed at a small value and only the detecting angle (2θ) was varied [8, 9]. **Fig. 2.8** shows the schematic of thin film and bulk modes of XRD. In the present study, both θ-2θ and α-2θ (α = 1°) modes were employed to obtain information of the individual phases within the film material.

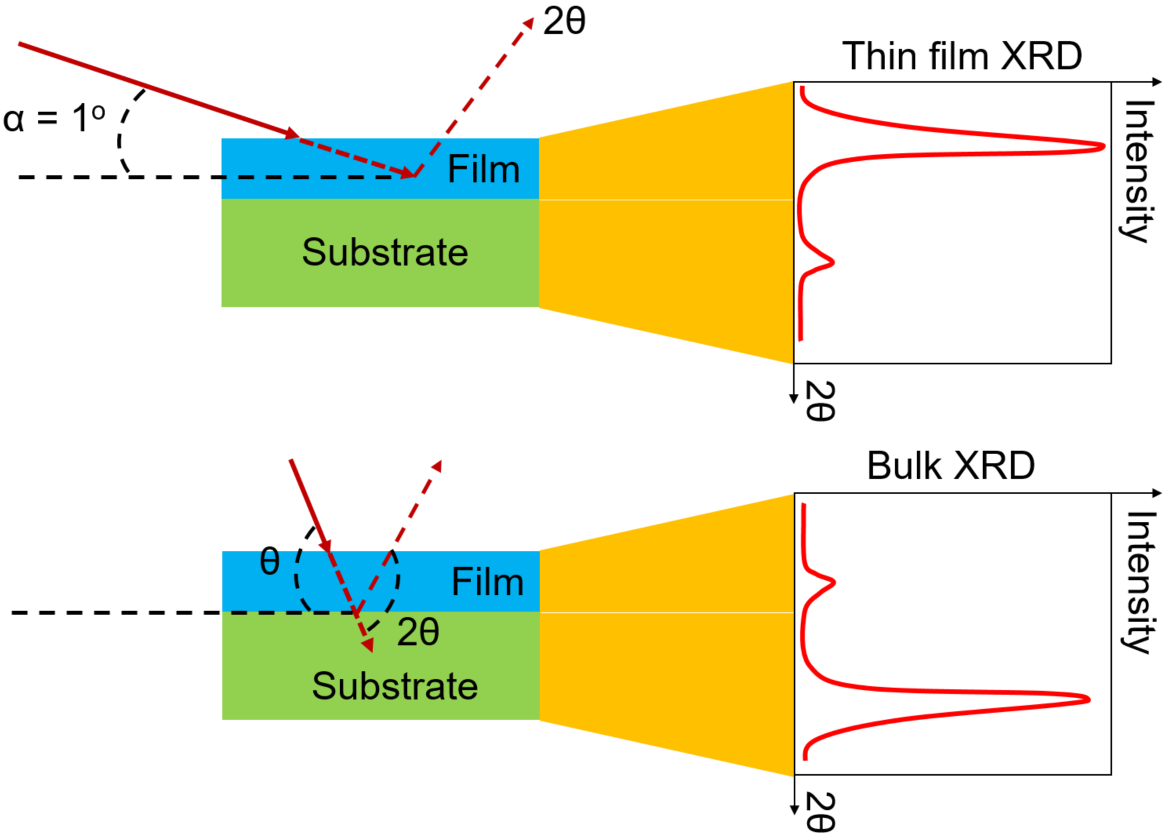

Figure 2.8 Schematic diagram illustrating the glazing incidence and bulk modes of X-ray diffraction measurements.

2.4.4 Scanning electron microscopy

Scanning electron microscopy (SEM) is mainly used to study the surface features or topography of a specimen employing a high-energy beam of electrons directed at the specimen surface. This beam of electrons produces various signals at the specimen surface. The high magnification, greater resolution, and ease of specimen examination make the SEM one of most widely employed microscopy techniques for the characterization of anodic films [10].

The surfaces and cross-section morphologies of barrier and porous type anodic films on magnesium and iron were examined by employing a JOEL JSM-6500F field emission scanning electron microscope operating at an accelerating voltage of 10-15 kV and working distance of 10 mm. Prior to SEM observation, the specimen was coated with platinum to produce electrical conducting surface at a current of 10 mA for 90 s under a vacuum of 4 Pa. For cross-section images, specimens were scratched from the back side with a diamond cutter to produce a notch, followed by immersion in liquid nitrogen for 20 minutes and finally cut employing tweezers. In examining both the surface and cross-section morphologies, images were taken employing secondary electrons mode.

2.4.5 Transmission electron microscopy

Transmission electron microscopy (TEM) is a technique used to provide sub-micrometer, the internal fine structure of materials. When combined with EDS, it is possible to determine the elemental composition of individual points or to map out the lateral distribution of elements from the imaged area. The technique primarily involves passing a beam of high-energy electrons through a thin specimen. TEM is a useful technique in the examination of crystal structure, morphology and thickness of anodic films on valve metals [11]. In the present study, the cross-sections of the anodized magnesium specimens were observed by a JEOL, JEM-2000FX transmission electron microscope operated at 200 kV. Specimen for TEM observation should be very thin, therefore, focused ion beam (FIB) was employed to prepare electron transparent thin specimens for direct TEM examination. FIB is mainly used to create very precise cross-sections of a specimen for subsequent characterization by SEM, TEM or STEM by employing a finely focused beam of ions (usually gallium) and sputters a small amount of material. Electron transparent sections were prepared employing a Hitachi FB2100 focused ion beam system. **Fig. 2.9** shows the sectioning of film material by FIB. Fluoride enrichment study of porous and nanotubular anodic films formed on iron was also examined by JEOL, JEM-ARF-200F atomic resolution analytical electron microscope. The machine is used owing to its unprecedented high resolution for the detection of light elements.

2.4.6 Electrochemical impedance spectroscopy (EIS)

Electrochemical impedance spectroscopy (EIS) has been used extensively as a laboratory-based research tool to characterize intrinsic electrical properties of any material and its interface [12, 13]. In recent years, the EIS technique has been used in routine laboratory testing for investigating the semi-conducting properties, ionic, electronic, protonic conductivities, and corrosion studies of metallic materials [14]. Further, the physicochemical characteristics of the electrode/electrolyte interface including electron transfer, mass transport and chemical reactions in an electrochemical system influence the impedance of the interface. The impedance of this interface depends on the charge of species adsorbed or present at the electrode/electrolyte interface, the composition of the electrolyte, and also the texture and nature of the electrodes. Therefore, EIS allows a complete description of such electrode/electrolyte interfaces with equivalent circuits for a given electron-transfer reactions under given experimental conditions.

EIS was performed employing IVIUMSTAT electrochemical interface for the magnetron-sputtered magnesium films anodized on to several voltages in the frequency range from 10^5 Hz to 0.1 Hz with an ac amplitude of 0.1 V in phosphate-containing and phosphate-free ethylene glycol electrolytes containing 0.1 mol dm^{-3} ammonium fluoride. The conductivities of phosphate-containing and phosphate-free electrolytes at various water concentrations were also evaluated by EIS.

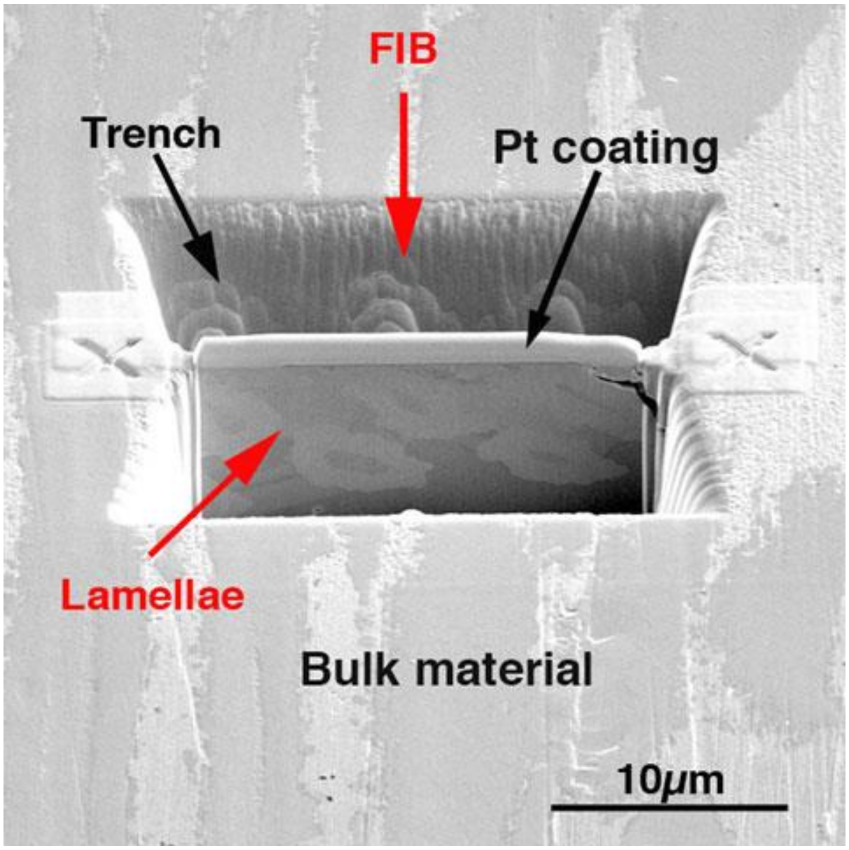

Figure 2.9 Sectioning of film material by FIB [15].

References:

[1] Fan Zhou, Thesis, *University of Manchester* (2011).

[2] K. Wagatsuma, K. Hirokawa, N. Yamashita, *Anal. Chim. Acta,* **324**, 147 (1996).

[3] K. Shimizu, H. Habazaki, P. Skeldon and G. E. Thompson, *Surf. Interface anal.,* **35**, 564 (2003).

[4] H. Bubert and H. Jennet, *Surface and Thin Film Analysis, Principles, Instrumentation and Applications,* Wiley-VCH Verlag GmbH (2002).

[5] L. R. Doolittle, *Nucl. Instr. Meth. Phys. Res.,* **B9**, 344 (1985).

[6] A. Climent-Font, V. Watjen, H. Bax, *Nucle. Instr. and Meth,* **B71**, 81 (1992).

[7] F. Brownand, W. D. Mackintosh, *J. Electrochem. Soc.,* **20**, 1973 (1096-1102).

[8] T. L. Alford, L. C. Feldman, J. W. Mayer, *Fundamentals of nanosclae film analysis, Springer* (2007).

[9] B. D. Cullity, *Elements of X-Ray Diffraction,* Addison-Wesley Publishing Company, Inc. (1956).

[10] P. J. Goodhew, J. Humphresy, R. Beanland, *Electron Microscopy and Analysis,* third edition, Taylor and Francis (2001).

[11] G. E. Thompson, R.C. Furneaux, J. S. Goode, G.C. Wood, *Trans. Inst. Metal Finishing,* **56**, 159 (1978).

[12] R. Scully, D.C. Silverman, M. W. Kending, *Electrochemical Impedance: Analysis and Interpretation,* ASTM, **99**, 253 (1993).

[13] E. Palibroda, A. Lupsan, S. Pruneanu, M. Savos, *Thin Solid Films,* **256**, 1001 (1995).

[14] K. Shimizu, G. E. Thompson, G. C. Wood, *Thin Solid Films,* **77**, 313 (1981).

[15] J. Ayache, L. Beaunier, J. boumendil, G. Ehret, D. Laub, *Sample preparation handbook for transmission electron microscopy,* Springer, (2010).

Chapter 3

Critical factors influencing on morphology and growth mechanism of anodic films on iron

3.1 Introduction

It is now possible to form both nanoporous and nanotubular anodic films on iron depending on the anodizing conditions in ethylene glycol (EG) electrolytes containing small amount of water and ammonium fluoride. Recently, it is reported that galvanostatic growth of the anodic films on iron was significantly influenced by the concentration of water in the EG electrolyte [1]. At low water concentrations, an unusual flat metal/film interface with the thicker barrier layer compared with an average interpore distance was developed. Thus, the film morphology did not resemble those of typical porous anodic alumina films [2]. Similarly, recent studies on anodic titania and zirconia nanotubes formed in fluoride-containing electrolytes disclosed that water and fluoride concentrations significantly influenced the nanotubular morphology [3-6]. Rangaraju *et al.* recently found that the transition from nanoporous to nanotubular structure on iron is critically controlled by anodizing voltage, fluoride and water concentrations in EG electrolyte. They proposed the preferential dissolution of fluoride-rich layer at the cell boundaries, forming nanotube morphology, although they did not observe such fluoride-rich layer [7]. La Tempa *et al*. reported that electrolyte temperature is critical for the formation of nanotube arrays on iron and for the increased growth rate of nanotubes [8]. Schmuki and coworkers proposed that nanotubes formation on iron occurs due to preferential dissolution of fluoride-rich layer similar to anodic titania nanotubes [9]. Schmuki *et al.* also suggested that anodizing potential affects the pore to tube transition for titania nanotubes because of field effect on fluoride ion mobility (faster or slower accumulation) and stress, which in turns affects the viscous oxide flow and the fluoride layer [10]. They also suggested that voltage influences the dissolution in the early stage of anodizing, while the pH in the pores affects the transition from nanoporous to nanotubular morphology [11-12]. However, information on critical factors controlling the growth of nanoporous and nanotubular films and their co-relation with structure, composition and film morphology is still very limited in anodizing of iron.

In the present study, the effect of water concentration on film morphology, composition, and structure of the anodic films formed potentiodynamically on iron in the EG electrolyte containing ammonium fluoride and water was first examined for a better understanding of porous anodic film growth on iron. In addition, the effects of formation voltage and current density on the formation and film morphology were also investigated at an optimum water concentration. The fluoride enrichment, which must be critical to control the film morphology, in the anodic films was examined by scanning transmission electron microscopy with EDS imaging.

3.2 Influence of water concentration

3.2.1 *i-V* and *i-t* responses

Fig. 3.1 shows the current-voltage responses during potentiodynamic anodizing of the bulk iron sheet at a sweep rate of 1.0 V s^{-1} to 50 V in the EG electrolytes containing various concentrations of water. As already shown in the previous chapter, a current maximum appears at 14 V at 0.1 mol dm^{-3} water, followed by a gradual current decrease up to 25 V, above which a steady-state current of 55 A m^{-2} is observed. The maximum current increases with an increase in the water concentration up to the water concentration of 1.0 mol dm^{-3}. At the water concentrations above 1.0 mol dm^{-3}, no current maximum appears and the current increases continuously with anodizing voltage. It is interesting that the current density during initial linear voltage rise in the low voltage region is not dependent upon the water concentration. In contrast, the current density at 50 V increases with an increase in the water concentration, from ~ 55 to ~ 240 A m^{-2}. **Fig. 3.2** shows the current-time curves during subsequent constant-voltage anodizing at 50 V for 15 min. It is obvious that current density gradually changes to a steady-state value after reaching to 50 V at all water concentrations. Again, the current density increases with an increase in water concentration during the constant-voltage anodizing at 50 V.

Fig. 3.3 shows the total electric charge passed during potentiodynamic anodizing to 50 V and subsequent potentiostatic anodizing at this voltage for 15 min. as a function of water

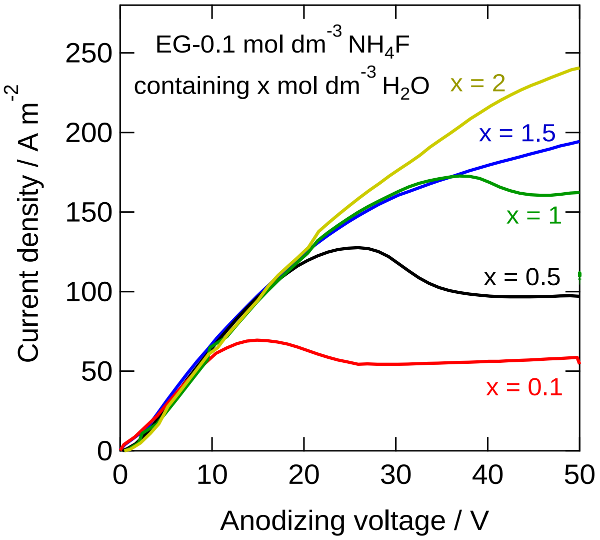

Figure 3.1 Potentiodynamic *i*-*V* curves of iron during anodizing to 50 V at 1 V s^{-1} in ethylene glycol electrolyte containing 0.1 mol dm^{-3} ammonium fluoride and various concentrations of water at 293 K.

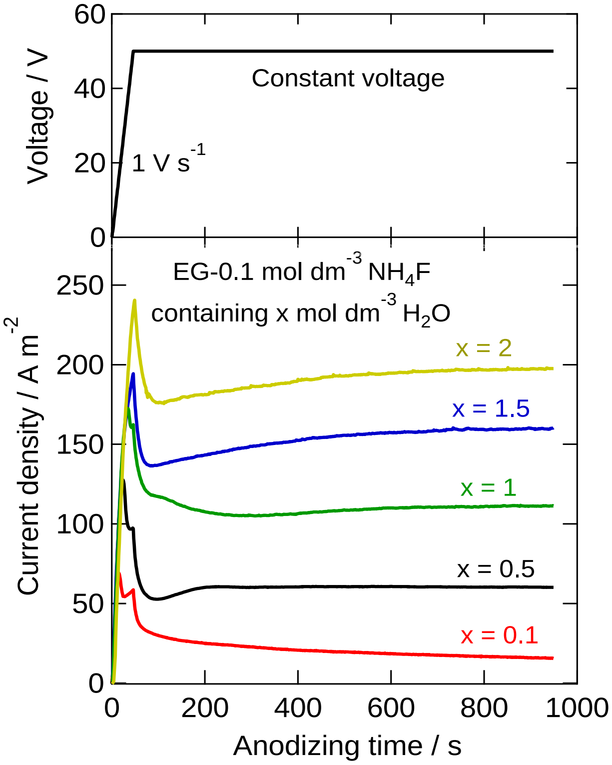

Figure 3.2 Current-time and voltage-time curves of iron during anodizing to 50 V at 1 V s^{-1} and subsequent constant-voltage anodizing in ethylene glycol electrolyte containing 0.1 mol dm^{-3} ammonium fluoride and various concentrations of water at 293 K.

concentration. The electric charge increases linearly with water concentration. As a consequence of this increase in the electric charge during anodizing, the thickness of the anodic film also increases with water concentration up to 1.5 mol dm^{-3} **(Fig. 3.4)**. However, at the water concentration of 2.0 mol dm^{-3}, the thickness of the anodic film remarkably reduced even though the electric charge is further increased. The reduced film thickness may be associated with enhanced chemical dissolution and gas evolution during anodizing at higher water concentrations. The enhanced gas generation during anodizing at 50 V by an increase in the water concentration is clearly seen in the photos shown in **Fig. 3.5**. On the surface of the specimens, which are located at the top-left side of the each photo, the number and size of gas bubbles on the specimen surface increase with the water concentrations.

3.2.2 Film morphology

The surfaces and cross-sections of the anodized specimens at various water concentrations were examined by scanning electron microscopy. Figs. **3.6a** and **3.6f** show the surface and cross-

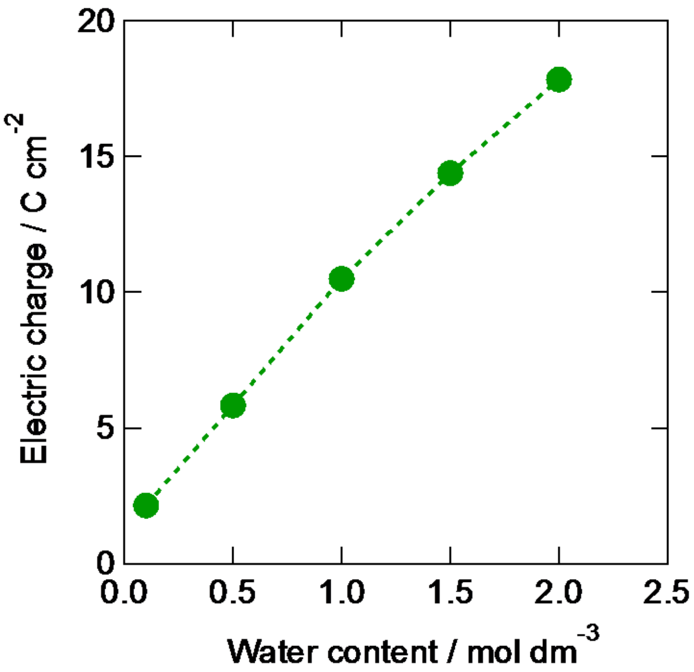

Figure 3.3 Changes in electric charge passed as a function of water concentration during anodizing of iron sheet at a sweep rate of 1 V s^{-1} to 50 V and then potentiostatically for 15 minutes in the EG electrolyte containing 0.1 mol dm^{-3} ammonium fluoride at 293 K.

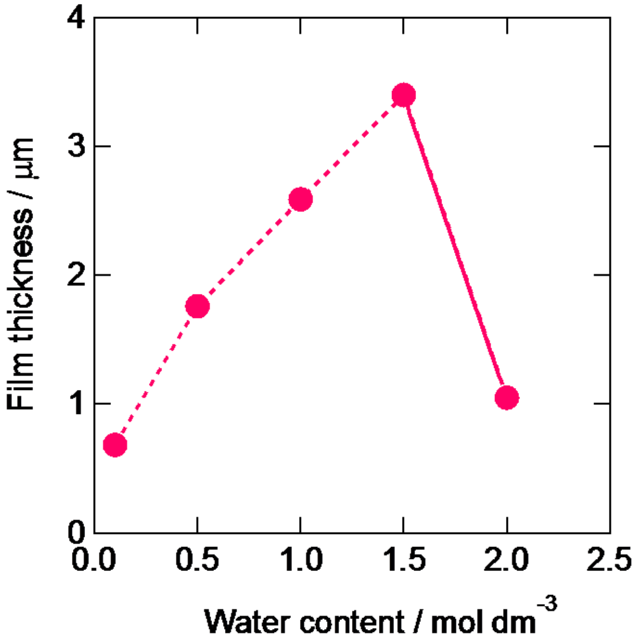

Figure 3.4 The thickness of anodic film with water concentration during anodizing initially potentiodynamically and then potentiostatically at 50 V for 15 minutes in the EG electrolyte containing 0.1 mol dm^{-3} ammonium fluoride at 293 K.

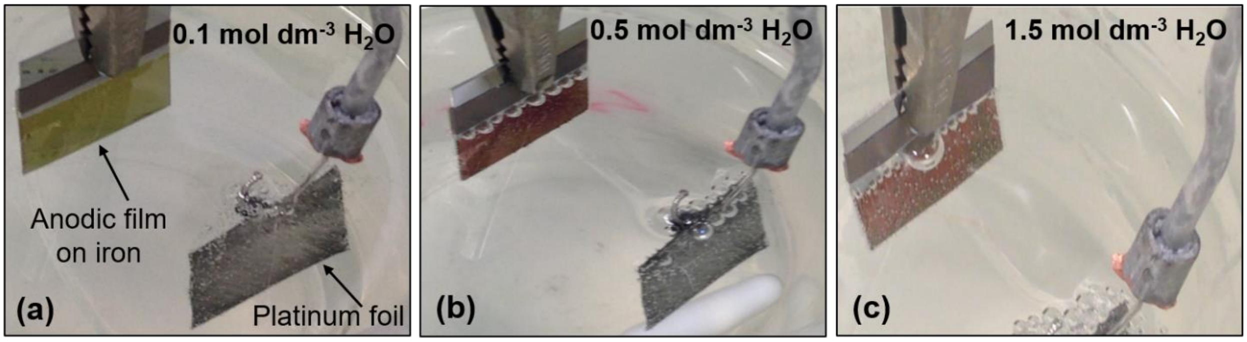

Figure 3.5 Images of gas evolution during anodizing of iron anodized at 50 V for 15 min in ethylene glycol electrolyte containing 0.1 mol dm^{-3} ammonium fluoride and (a) 0.1, (b) 0.5, and (c) 1.5 mol dm^{-3} water at 293 K.

section images, respectively, of the iron anodized at 50 V in the electrolyte with the lowest water concentration (0.1 mol dm^{-3}). The porous anodic film is developed, but the pore size is rather small and some cylindrical pores are not clearly seen in the cross-section images. The thickness of the anodic film is 0.68 μm and that of the barrier layer, located between the outer porous layer and iron substrate, is 120 nm. The anodic films were detached from the metal substrate in the cross-sectional scanning electron micrographs **(Figs. 3.6f-3.6j)**, which probably occurred during fracturing of the anodized specimens for SEM observations. When the water concentration in the electrolyte is increased, cylindrical pore channels, which are normal to the metal/film interface, are more clearly seen in both surface and cross-section scanning electron micrographs. Many pores penetrate from the film surface to the barrier layer. The pore size observed at the film surface appears to increase with water concentration, probably associated with the increased chemical dissolution of pore walls during anodizing at higher water concentrations. Because of increased chemical dissolution with water concentration, the surface and outer part of the anodic films become rough and irregular, as seen in **Figs. 3.6e and 3.6j** at 2.0 mol dm^{-3} water. The thickness of the barrier layer and the ratio of interpore distance to barrier layer (D_c/D_b) also change with water concentration as shown in **Fig. 3.7**. As described above, the thickness of the barrier layer is 120 nm at 0.1 mol dm^{-3} water, which reduced to ~95 nm and 90 nm at 0.5 and 1.0 mol dm^{-3} water respectively and further to ~80 nm (1.5 mol dm^{-3} water) and ~60 nm (2.0 mol dm^{-3}). Another important feature is the morphology of the metal/film interface. It is well known that porous anodic alumina films developed in aqueous acid electrolytes, such as sulfuric acid, oxalic acid, and phosphoric acid, show scalloped metal/film interface, and the film morphology is described by a Keller-Hunter-Robinson model [13]. Similar scalloped interface is developed when the water concentration in the electrolyte is relatively high (1.5 and 2.0 mol dm^{-3}) as shown in **Fig. 3.8**, but the interface is rather flat at the lower water concentrations (**Figs. 3.6f-3.6h**). These findings suggest the change in growth mechanism with water concentration in electrolyte.

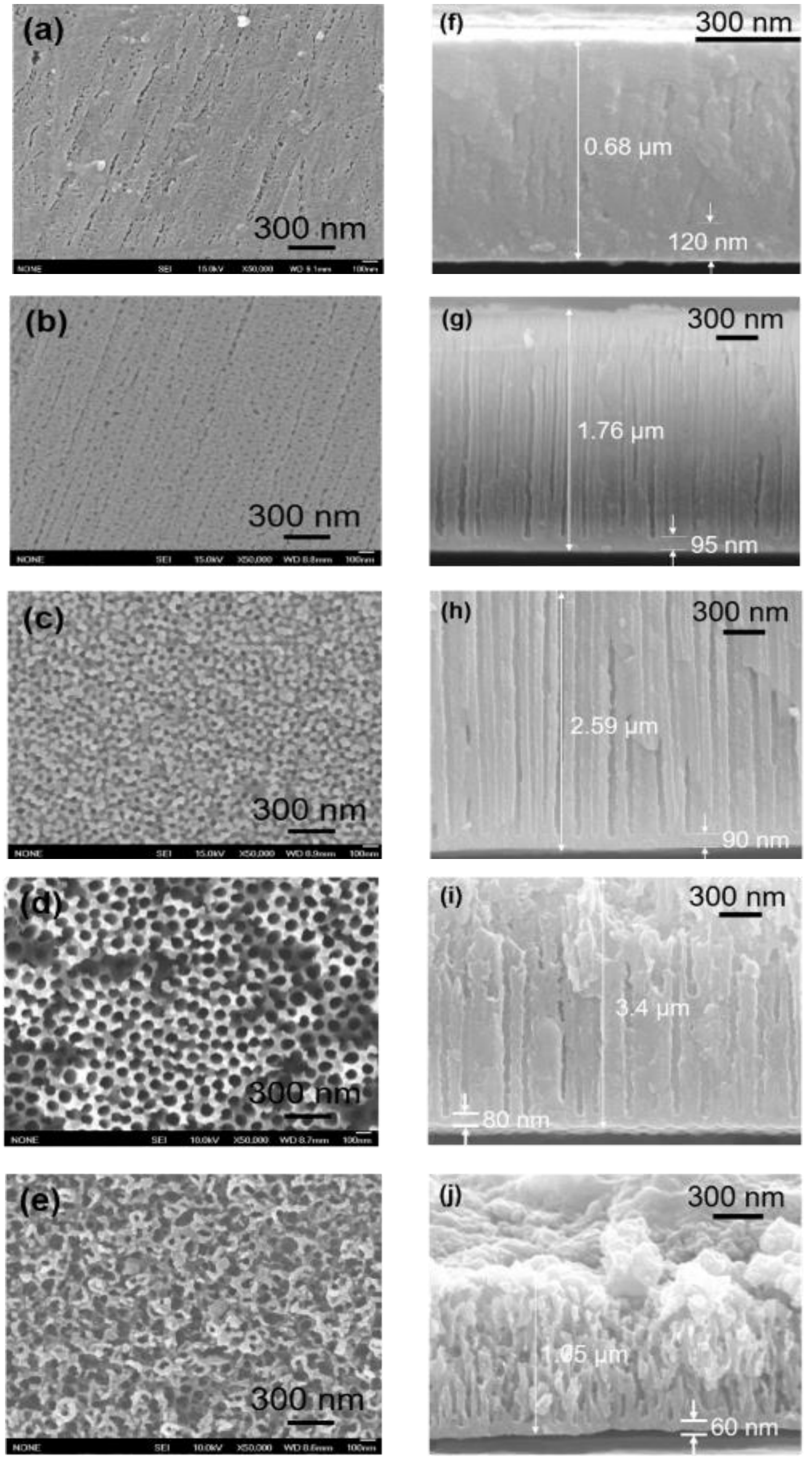

Figure 3.6 Scanning electron micrographs of (a-e) surfaces and (f-j) cross-sections of iron sheet anodized at 50 V for 15 min in ethylene glycol electrolyte containing 0.1 mol dm^{-3} ammonium fluoride and (a, f) 0.1, (b, g) 0.5, (c, h) 1.0, (d, i) 1.5 and, (e, j) 2.0 mol dm^{-3} water at 293 K.

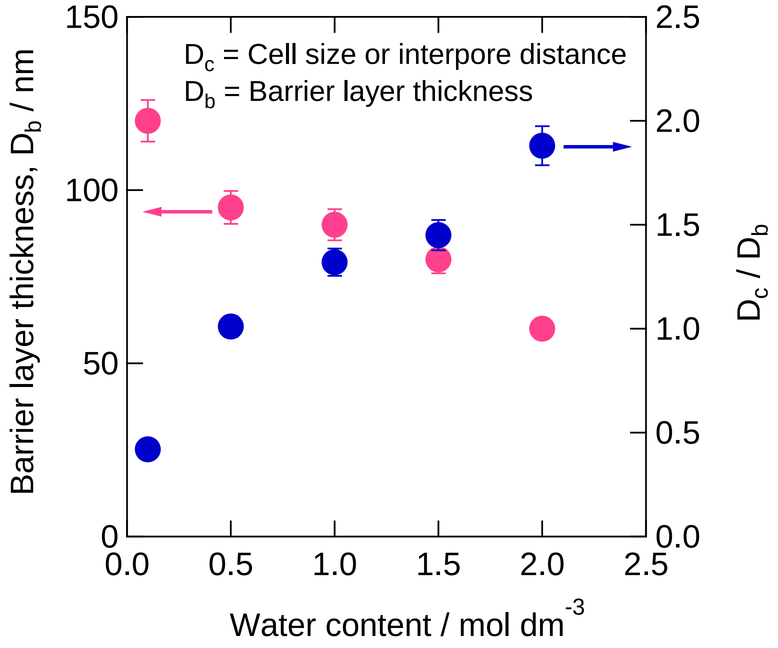

Figure 3.7 Correlation of barrier layer thickness and interpore distance with water concentration during anodizing of anodic films at 50 V for 15 minutes in ethylene glycol electrolyte containing 0.1 mol dm^{-3} ammonium fluoride at 293 K.

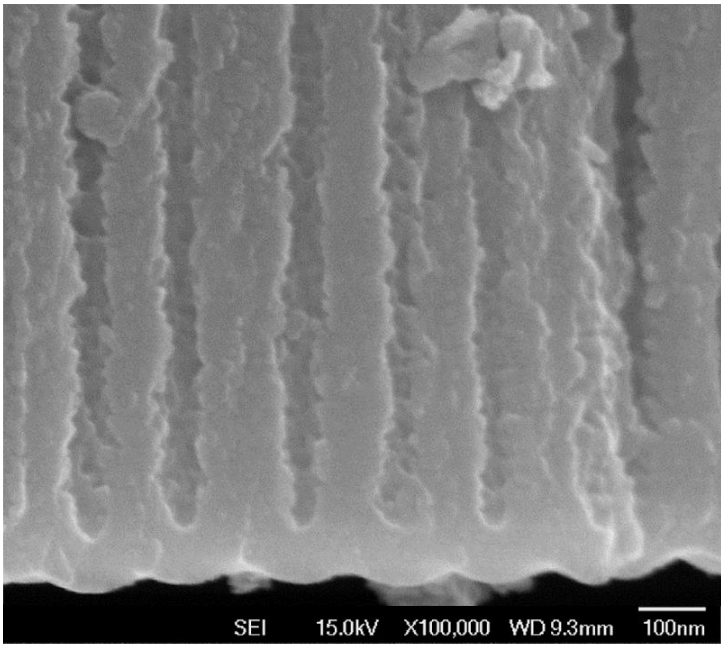

Figure 3.8 Enlarged cross-section of anodic film of iron sheet anodized to 50 V for 15 min in ethylene glycol electrolyte containing 0.1 mol dm^{-3} ammonium fluoride and 1.5 mol dm^{-3} water at 293 K.

3.2.3 Film composition

The change in the barrier layer thickness and the film and interface morphologies with water concentration may be associated with compositional change of the anodic films. Therefore, the composition of anodic films at various water concentrations was examined qualitatively by GDOES elemental depth profile analysis. **Figs. 3.9a-3.9c** shows the intensity ratio of carbon, oxygen, and fluorine to the iron emission of the specimens anodized at 50 V in 0.1, 0.5, and 1.5 mol dm^{-3} water. The intensity ratios of all carbon, oxygen, and fluorine to iron are higher in the anodic film formed at 0.1 mol dm^{-3} water and decreases with an increase in water concentration. A steep intensity reduction for fluorine, oxygen, and carbon at sputtering time of 13s, 27s, and 35s at water concentrations of 0.1, 0.5, and 1.5 mol dm^{-3} respectively indicates the location of the metal/film interface. The sputtering time to the metal/film interface is shorter for the anodic film formed in 0.1 mol dm^{-3} water in comparison with that formed in 0.5 and 1.5 mol dm^{-3} water, in agreement with their film thicknesses shown in **Fig. 3.4**. The anodic films contain iron, fluorine, derived from fluoride species in the electrolyte, and carbon species, derived from EG, in addition to oxygen, which may be originated from water added in the electrolyte. The excess amounts of electrolyte species are incorporated in the anodic films formed at lower water concentrations, probably influencing the field strength of the barrier layer in the growing anodic films.

3.2.4 Film structure

The phases in the anodic films also change with the water concentration. **Fig. 3.10** shows XRD patterns of the iron specimens anodized in different water concentrations. At the high water concentration of 1.5 and 2.0 mol dm^{-3}, $FeF_3 \cdot 0.5H_2O$ phase with a pyrochlore structure is clearly identified. In contrast, poorly crystalline anodic films are formed at lower water concentrations. At 0.5 mol dm^{-3} water, very weak reflections of the $FeF_3 \cdot 0.5H_2O$ phase are found. Further reduction of water concentration to 0.1 mol dm^{-3} results in the phase change to FeF_2. It is unlikely that the hydrated fluoride phase is developed during anodizing under the high electric field. The hydration of a fluoride phase may occur during post-treatments of the anodized specimens. However, the formation of hydrated fluoride only at high water concentrations suggests that the actual phase formed during anodizing is also dependent upon the water concentration.

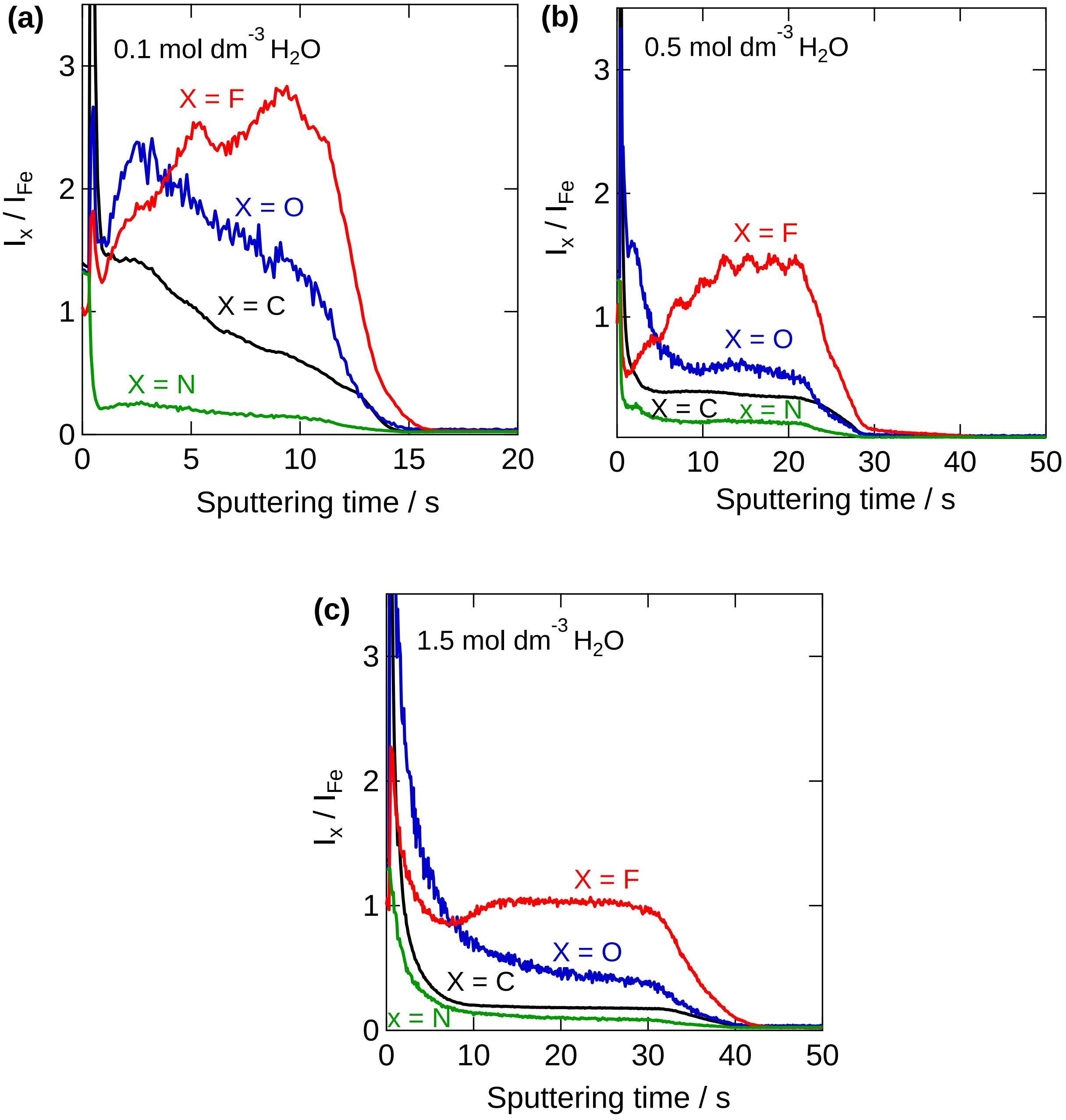

Figure 3.9 GDOES elemental depth profiles of iron anodized at 50 V for 15 min. in ethylene glycol electrolyte containing 0.1 mol dm^{-3} ammonium fluoride and (a) 0.1, (b) 0.5 and, (c) 1.5 mol dm^{-3} water at 293 K.

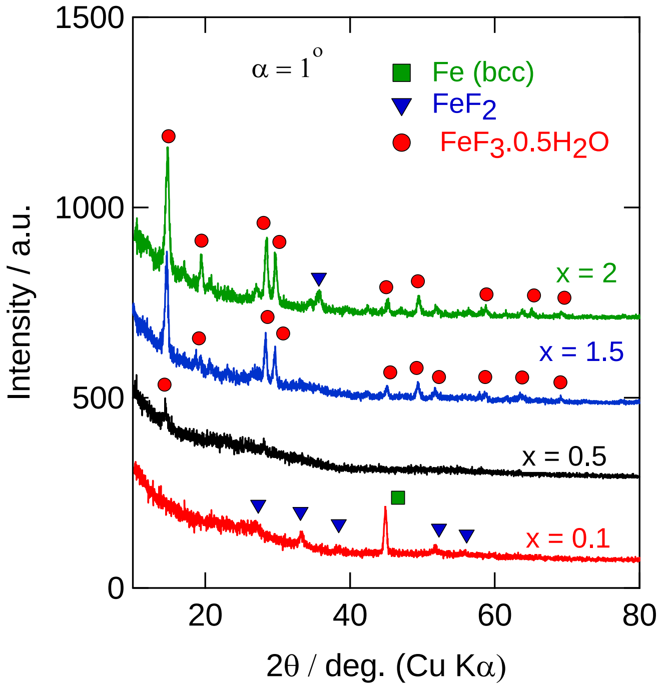

Figure 3.10 XRD patterns of iron anodized at 50 V for 15 min in ethylene glycol electrolyte containing 0.1 mol dm^{-3} ammonium fluoride and 0.1, 0.5, and 1.5 mol dm^{-3} water at 293 K.

3.2.5 Discussion

The present study discloses that the anodizing behavior and film morphology change with water concentration in the EG-containing fluoride electrolytes. A scalloped metal/film interface, typical of porous anodic alumina films, is developed on iron only at high water concentrations of 1.5 and 2.0 mol dm^{-3}. The formation of relatively flat metal/film interface at lower water concentrations suggests the change in the growth mechanism of the anodic films with water concentrations. It is obvious from **Fig. 3.7** that the thickness of the barrier layer reduces and the interpore distance is enlarged with an increase in water concentration. As a consequence, the ratio of the interpore distance to the barrier layer thickness increases from ~0.42 at 0.1 mol dm^{-3} water to ~2.0 at 2.0 mol dm^{-3} water. The ratio approaches the typical value of 2.5 for porous anodic alumina films formed in sulfuric acid, oxalic acid, and phosphoric acid by increasing water concentration [14].

As discussed earlier, the two important mechanisms for growth of porous anodic films on aluminum: a field-assisted dissolution model and a field-assisted flow model. The field-assisted oxide dissolution has been recently confirmed experimentally by Oh and Thompson [15] by devising discontinuous anodizing approach, in which they re-anodized planar pre-formed alumina barrier film on aluminum in phosphoric acid electrolyte and found enhanced dissolution of the barrier layer by increasing the applied electric field. They also suggested that at sufficiently high electric field incipient pores are formed, associated with the field-induced instability at the film/electrolyte interface. The morphology of the anodic films with the incipient pores resembles those formed on iron at lower water concentrations. Thus, it is likely that field-assisted dissolution is predominant to develop porous anodic films on iron in the EG electrolytes containing the lower concentrations of water, while flow of film material may contribute to the formation of anodic films on iron with scalloped metal/film interface at the high water concentrations. It has been also reported that incorporation of electrolyte anion species into anodic alumina, i.e., the composition of alumina films, is crucial importance for flow of film material in growing porous alumina films [16-17]. As shown in **Fig. 3.9**, the composition of the anodic films on iron changes with water concentration in electrolyte. In addition, the crystallinity of the anodic films is influenced by water concentration for anodized iron. These factors may have influenced the growth mechanism of the anodic films on iron.

3.3 Influence of formation voltage

Since porous morphology with typical scalloped metal/film interface was developed at 1.5 mol dm^{-3} water concentration, further investigation of the formation of anodic films at various anodizing voltages was carried out at this water concentration. **Fig. 3.11** shows the current-time curves during potentiodynamic/potentiostatic anodizing of iron from 30 to 100 V in the ethylene glycol electrolyte containing 1.5 mol dm^{-3} water at 293 K. Current density increases continuously without showing a current maximum during initial potentiodynamic anodizing at a sweep rate of 1 V s^{-1}. During subsequent potentiostatic anodizing for 15 minutes, the current density is almost steady state at and below 60 V, while the current density increases continuously above 60 V. In addition to current density, bath temperature also increased during anodizing at higher voltages due to Joule heating. In order to account for this effect, the variation of temperature with time during anodizing at 40 and 100 V is also recorded (**Fig. 3.12**). It is obvious from **Fig. 3.12** that the temperature rises continuously during anodizing at 100 V, while the temperature remained constant at 40 V. The rise of the temperature may primarily contribute to the continuous increase in the current density during anodizing at 100 V.

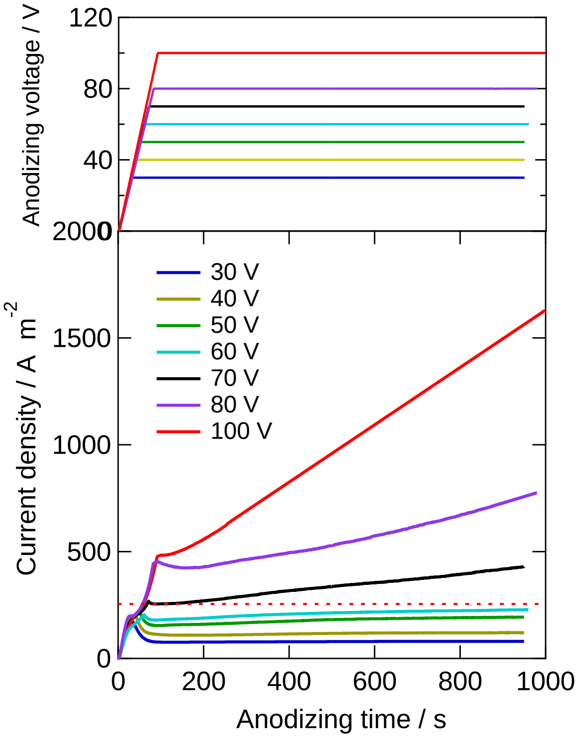

Figure 3.11 Current-time responses of anodic films on bulk iron specimens anodized to the selected voltages at a sweep rate of 1 V s^{-1} at which voltage is kept constant for 15 minutes in the ethylene glycol electrolyte containing 1.5 mol dm^{-3} water and 0.1 mol dm^{-3} ammonium fluoride at 293 K.

Figs. 3.13 and 3.14 show the surface and cross-section morphologies of the anodic films formed at 1.5 mol dm^{-3} water concentration at the several voltages. Surface morphologies, shown in **Fig. 3.13**, demonstrate that a nanoporous morphology is developed at and below 50 V and the pore size increases with anodizing voltage. When the anodizing voltage raised to 60 V or higher, film morphology transforms from nanoporous to nanotubular. However, the cross-section images show that a porous morphology is always present without separation into individual tubes at the inner part of the anodic films (**Figs. 3.14c-d**). The formation of nanotubes will be discussed later in detail. Cylindrical pores are evident from cross-section images from 40 V to 100 V in **Fig. 3.14**

and are aligned normal to film surface. A scalloped metal/film interface is obvious, regardless of anodizing voltage and mainly depends on water concentration as mentioned above.

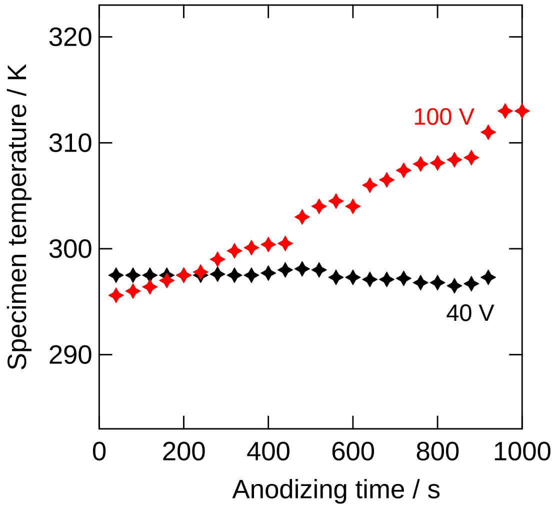

Figure 3.12 Variation in the temperature during anodizing at 40 V and 100 V in the ethylene glycol electrolyte containing 1.5 mol dm^{-3} water and 0.1 mol dm^{-3} ammonium fluoride at 293 K.

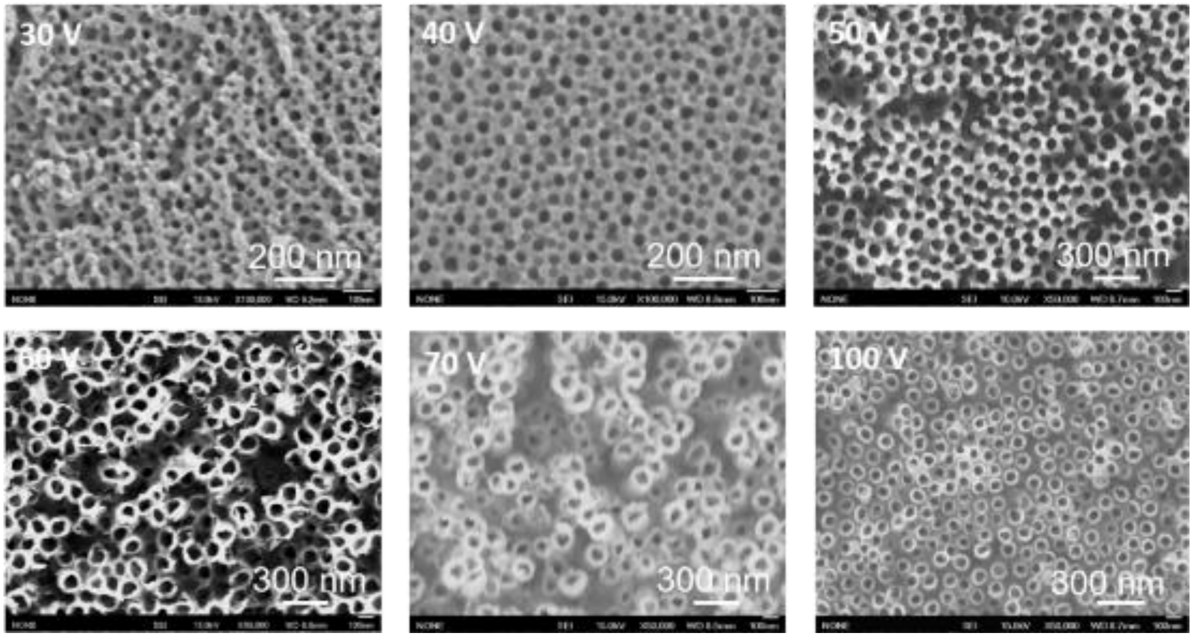

Figure 3.13 Scanning electron micrographs of the anodic films formed on bulk iron sheet to the selected voltages at a sweep rate of 1 V s^{-1} in the ethylene glycol electrolytes containing 1.5 mol dm^{-3} water and 0.1 mol dm^{-3} ammonium fluoride at 293 K.

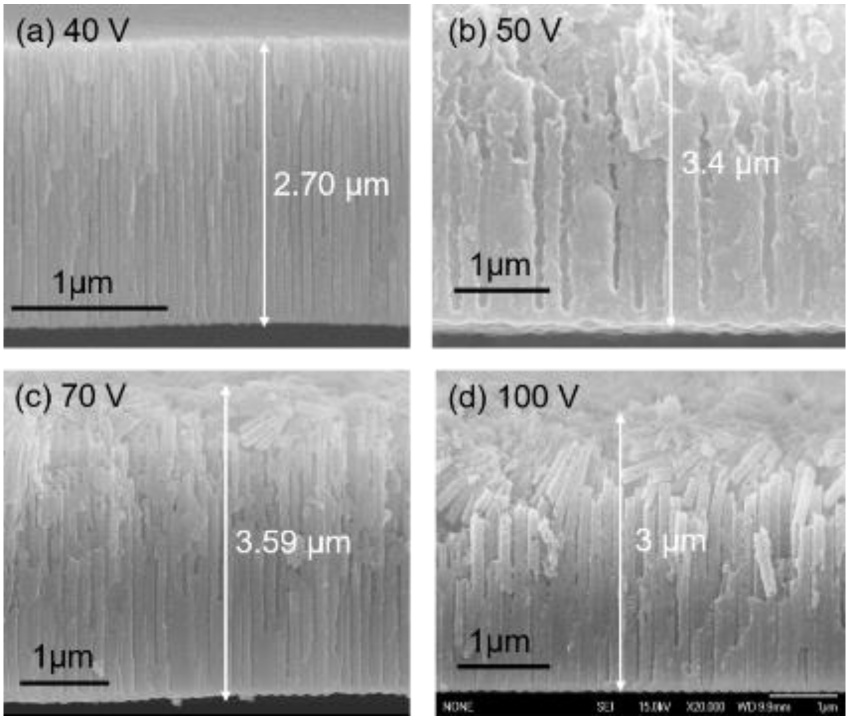

Figure 3.14 Scanning electron micrographs of the cross-sections of anodic films formed on bulk iron sheet at a sweep rate of 1 V s^{-1} in the ethylene glycol electrolyte containing 1.5 mol dm^{-3} water and 0.1 mol dm^{-3} ammonium fluoride (a) 40 V, (b) 50 V, (c) 70 V, and (d) 100 V at 293 K.

The thickness of the anodic films also increases with anodizing voltage up to 70 V from 2.7 μm at 40 V to 3.6 μm at 70 V due to increasing in the electric charge. However, the film thickness reduces to ~3 μm, even though the electric charge is remarkably increased at 100 V. The variation of film thickness with the quantity of electricity is shown in **Fig. 3.15**, which shows that film thickness and hence the growth rate increases sharply with electric charge from 40 to 70 V, thereafter, growth rate decreases with further increase in anodizing potential. A rapid gas evolution was observed with the naked eye at higher anodizing potential, but it became less significant with the reduction in anodizing voltage. The enhanced gas evolution, as well as increased chemical dissolution during anodizing, may cause the thickness reduction at 100 V. Such reduction of barrier layer thickness and tube length by chemical dissolution in acidic electrolytes are typical of titania nanotubes [18-19].

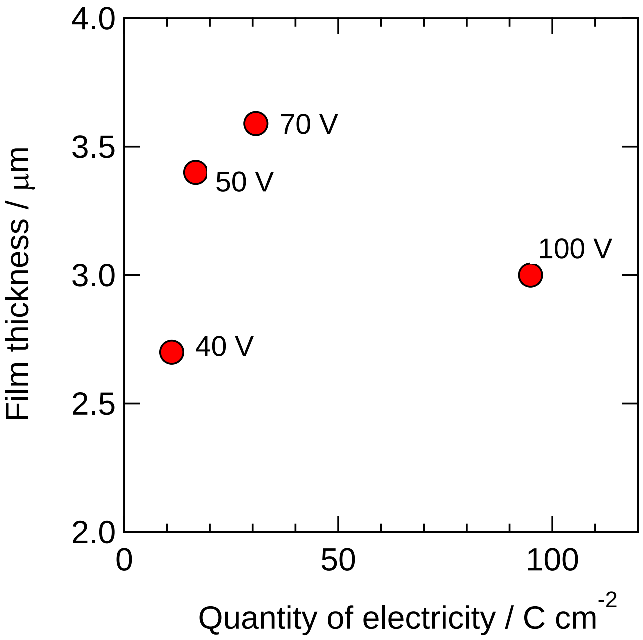

Figure 3.15 Film thickness as a function of quantity of electricity of the anodic films formed on bulk iron sheet to the selected voltages at a sweep rate of 1 V s^{-1} in the ethylene glycol electrolyte containing 1.5 mol dm^{-3} H_2O and 0.1 mol dm^{-3} ammonium fluoride at 293 K.

The change in the interpore distance and barrier layer thickness with formation voltage was examined. Since the resistance of the organic electrolyte used in this study was relatively high. The voltage drop by the electrolyte may not be neglected at high current density. Thus, the voltage drop by the electrolyte during anodizing was estimated from Ohm's law employing solution resistance as well as from the initial voltage surge as shown later in **Fig. 3.17** at various current densities. The solution resistance is measured by means of electrochemical impedance spectroscopy in a two electrodes system employing platinum foil as cathode and anode. As shown in **Fig. 3.16a** the voltage drop increases almost linearly with current density, suggesting that actual voltage across the anodic film is largely different than the applied anodizing voltage. **Fig. 3.16b** shows that barrier layer film thickness increases linearly with anodizing voltage after IR compensation by the electrolyte. As can be seen in **Fig. 3.16a**, the voltage drop at high current density significantly influences the anodizing voltage, therefore, barrier layer at 100 V reduces to 63 nm which is close to the barrier layer film thickness at 50 V. **Fig. 3.16c** shows that interpore distance also increases almost linearly with anodizing voltage after IR compensation. Generally, the interpore distance increases linearly with anodizing potential with a proportionality constant of approximately 2.5 nm V^{-1} for typical porous anodic alumina.

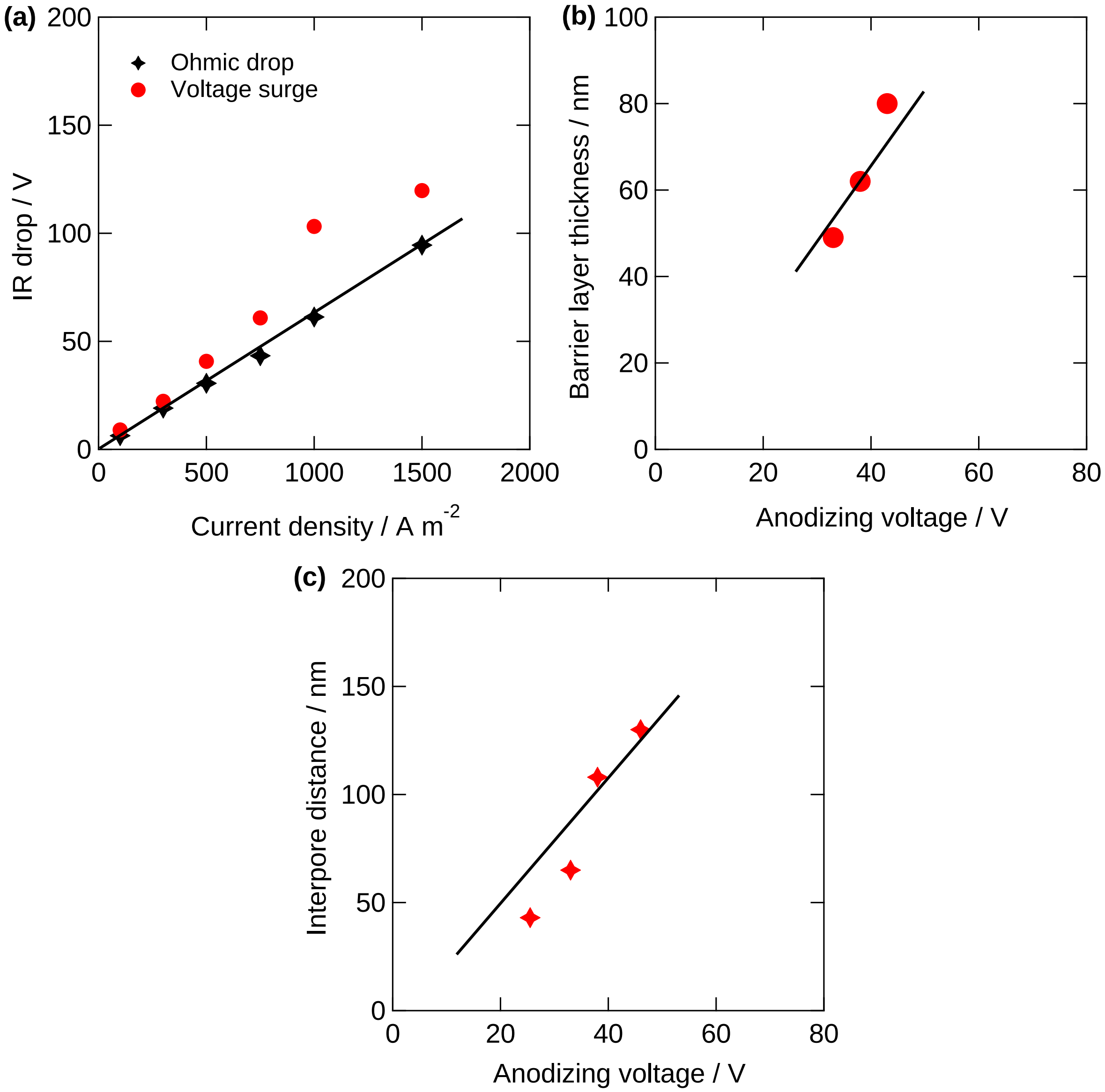

Figure 3.16 (a) Ohmic drop during anodizing as a function of current density, (b) dependence of barrier layer film thickness on anodizing voltage after IR compensation, and (c) variation of interpore distance with anodizing voltage in the EG electrolyte containing 1.5 mol dm^{-3} water and 0.1 mol dm^{-3} ammonium fluoride at 293 K.

3.4 Influence of current density

Fig. 3.17 shows the voltage-time responses at selected current densities ranges from 100 to 1500 A m^{-2} for 900 s at 1.5 mol dm^{-3} H_2O concentration. Higher current densities lead to higher anodizing voltages. At the very beginning of anodizing, voltages rises sharply with current density and initial voltage peak appears at and above 750 A m^{-2} followed by sharp voltage reduction before the voltage decline to a final steady-state voltage.

Scanning electron micrographs in **Figs. 3.18a-c** reveal that nanoporous films are obtained at ≤500 A m^{-2}, and the pore size increases as the current density increases from 100 to 500 A m^{-2} due to increase in voltage. Above 500 A m^{-2}, nanotubular morphology is observed (**Figs. 3.18d-f**). In potentiostatic anodizing, nanotubular films were formed at and above 60 V. This voltage exceeds at 500 A m^{-2} in galvanostatic anodizing, but still a nanoporous film is formed at this current density. Thus, it is unlikely that there is a critical formation voltage to form nanotubular anodic films.

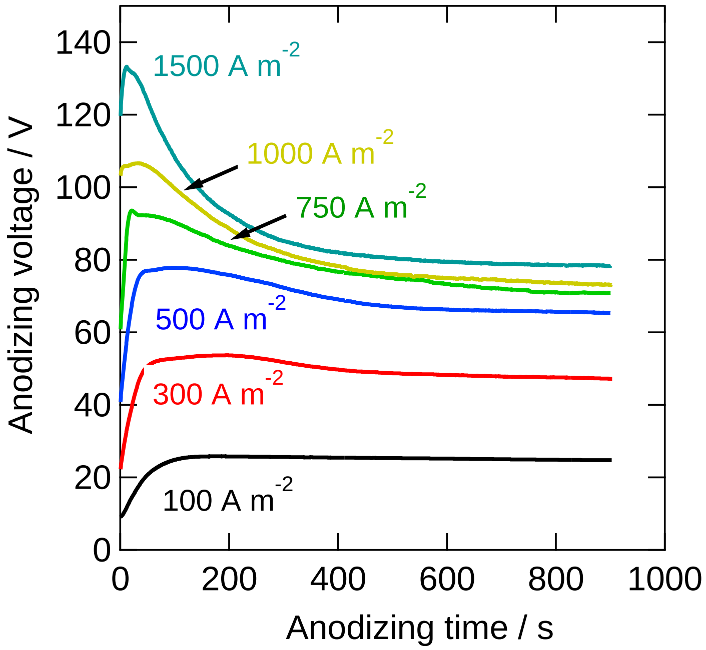

Figure 3.17 Voltage-time curves of anodic films on bulk iron specimens anodized to the selected current densities for 15 min in the ethylene glycol electrolyte containing 1.5 mol dm^{-3} water and 0.1 mol dm^{-3} ammonium fluoride at 293 K.

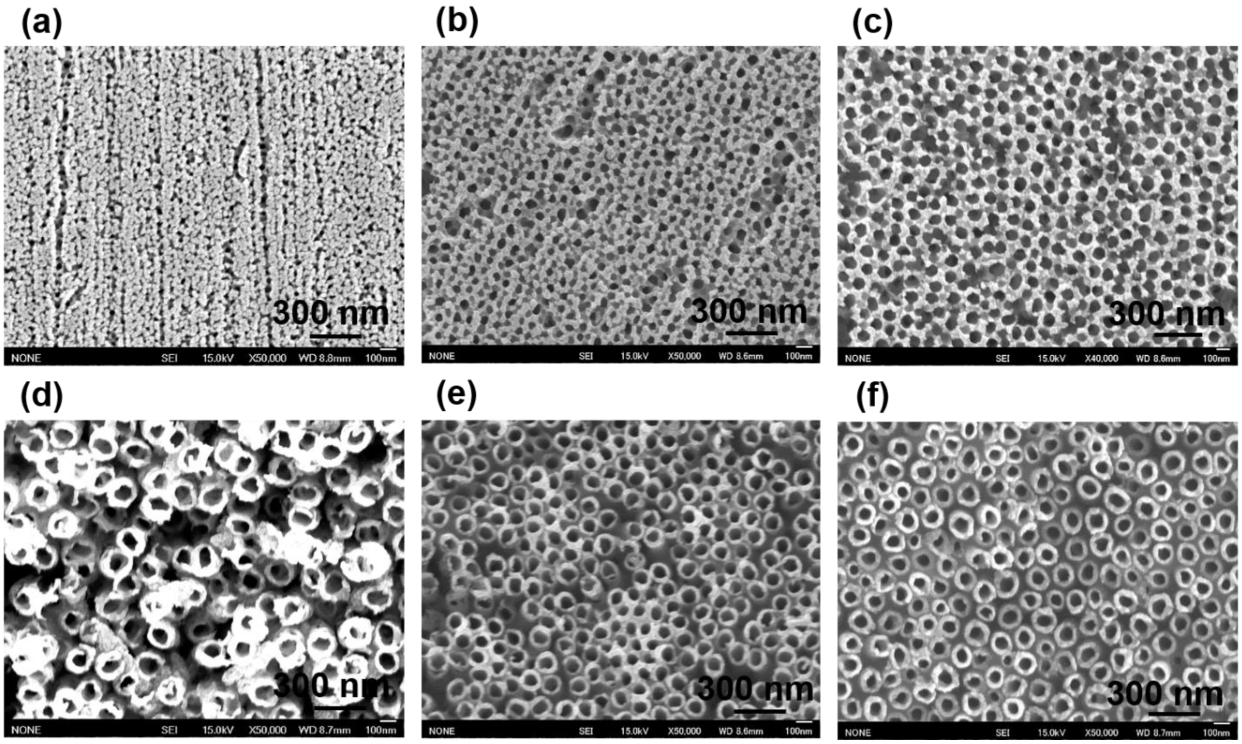

Figure 3.18 Scanning electron micrographs of the surfaces of the anodic films formed on bulk iron sheet (a) 100 A m^{-2}, (b) 300 A m^{-2}, (c) 500 A m^{-2}, (d) 750 A m^{-2}, (e) 1000 A m^{-2}, and 1500 A m^{-2} in the ethylene glycol electrolyte containing 1.5 mol dm^{-3} water and 0.1 mol dm^{-3} ammonium fluoride at 293 K.

3.5 Distribution of fluoride in the anodic films

Potentiostatic anodizing discloses that nanoporous films are formed at low formation voltage, while the film structure was transformed to tubular at high anodizing voltage. As mentioned in chapter 1, it is known that nanotubular anodic films are formed on titanium and the nanotubular structure is developed by preferential dissolution of cell boundaries where fluoride species enrich. The fluoride enrichment at cell boundaries occurs as a consequence of the faster migration of fluoride species rather than oxide ions inwards during film growth [20-21]. Accumulation of fluoride-rich layer at the cell boundaries leads to chemical sensitization of these regions due to the solubility of the fluoride-rich region in the electrolytes, thus, these regions are key in the formation of nanotubes. It is, therefore, necessary to get further insight of the origin of tube formation on iron by exploring the fluoride distribution in the anodic films at nanometer resolution. For this study, two anodizing specimens, one with nanoporous morphology at low voltage and other with nanotubular morphology at higher voltage were chosen and anodic films were formed potentiodynamically at a sweep rate of 1 V s^{-1} at 40 V and 100 V in 1.5 mol dm^{-3} H_2O, followed by constant voltage anodizing for 900s. For comparison, two specimens formed at 50 V in 0.1 and 0.5 mol dm^{-3} H_2O concentrations for 900 s were also examined.

Fig. 3.19 shows the general TEM appearance of the anodic films formed at 100 V at a water concentration of 1.5 mol dm^{-3}. The thickness of anodic films was ~ 3.13 µm and is consistent with the SEM observation (**Figs. 3.14d**). The outer part of the anodic film appears to be damaged at 100 V by FIB. Cylindrical pore channels are also evident from TEM cross-section similar to SEM.

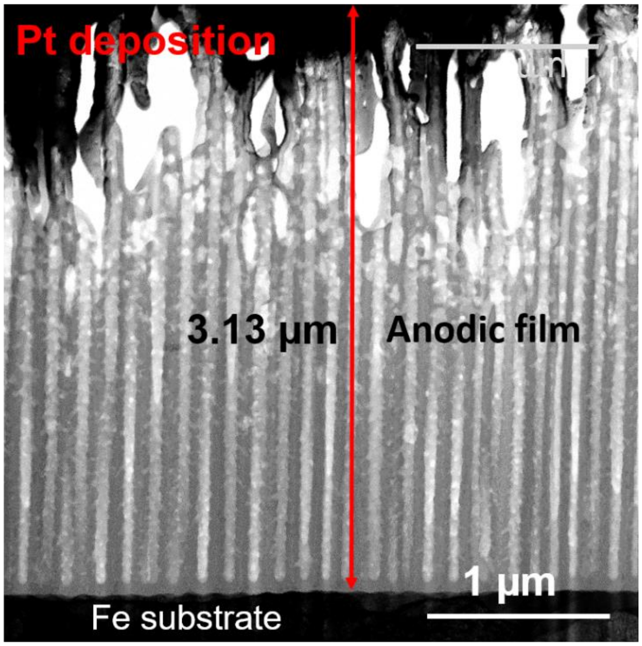

Figure 3.19 Transmission electron micrograph of FIB-cross-section of anodic film formed potentiodynamically on iron at 100 V in the ethylene glycol electrolyte containing 1.5 mol dm^{-3} water and 0.1 mol dm^{-3} ammonium fluoride at 293 K.

Figs. 3.21-3.22 display the bright field (BF) and corresponding EDS maps at 100 V, which reveal the fluorine, oxygen, and iron at the bottom, middle, and outer regions of anodic films.

Fluoride enrichment at the cell boundaries can be clearly seen in these images. Assuming faster migration of fluorine species compared with oxide ions, the film formed at cell boundaries should consists of iron fluoride and the outer region containing fluorine species, oxygen, and iron. Scalloped metal/film interface can be clearly seen from these EDS/BF images (**Fig. 3.20**). It is obvious that fluoride enriched layer of uniform thickness is present at the metal/film interface and at the cell boundaries in the bulk part. However, the outer region of the anodic film appears to be fluoride depleted because of accelerated chemical etching (**Fig. 3.22**). This is more obvious in the superimposed EDS image of oxygen and fluorine, indicating that nanotubes are formed by the preferential chemical dissolution of the fluoride-rich layer at the outer part of the anodic film (**Fig. 3.22**). As outer part of the film is formed during early stages of anodizing and is exposed for a longer time to the electrolyte, it is likely that preferential chemical dissolution of the fluoride-rich layer is only limited to the outer part, thus forming the nanotubes at 100 V.

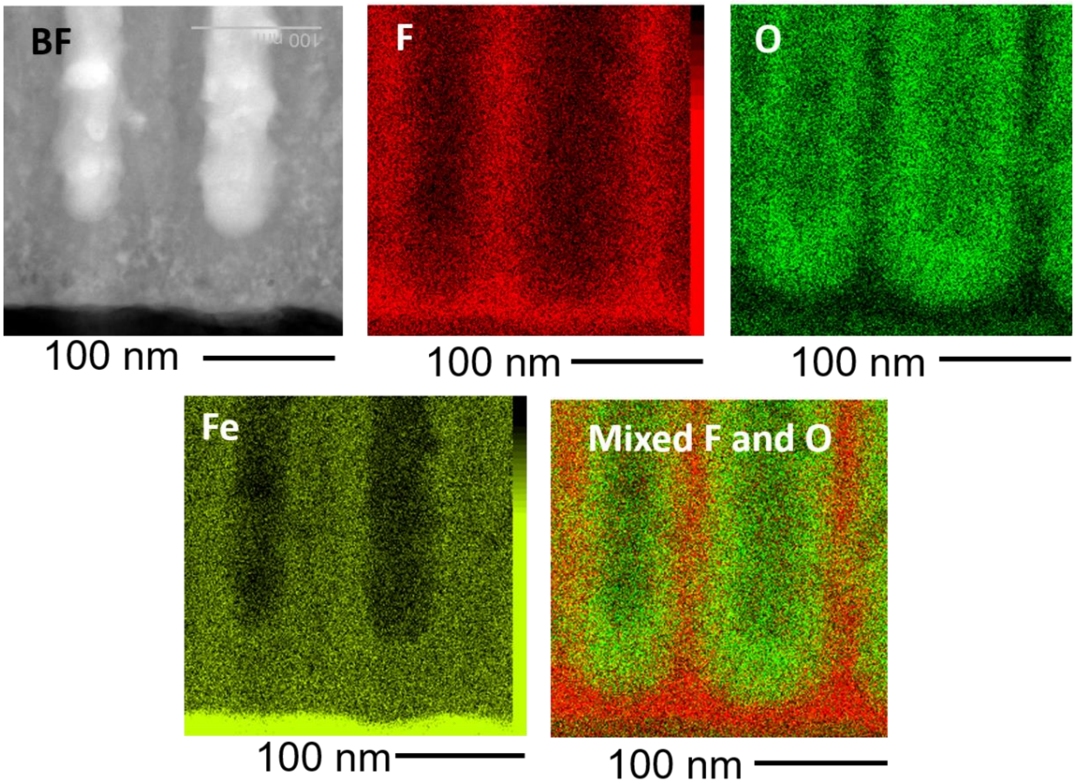

Figure 3.20 Bright field image and corresponding EDS maps of the bottom region of FIB-treated anodic film formed on iron at 100 V in the ethylene glycol electrolyte containing 1.5 mol dm^{-3} water and 0.1 mol dm^{-3} ammonium fluoride at 293 K.

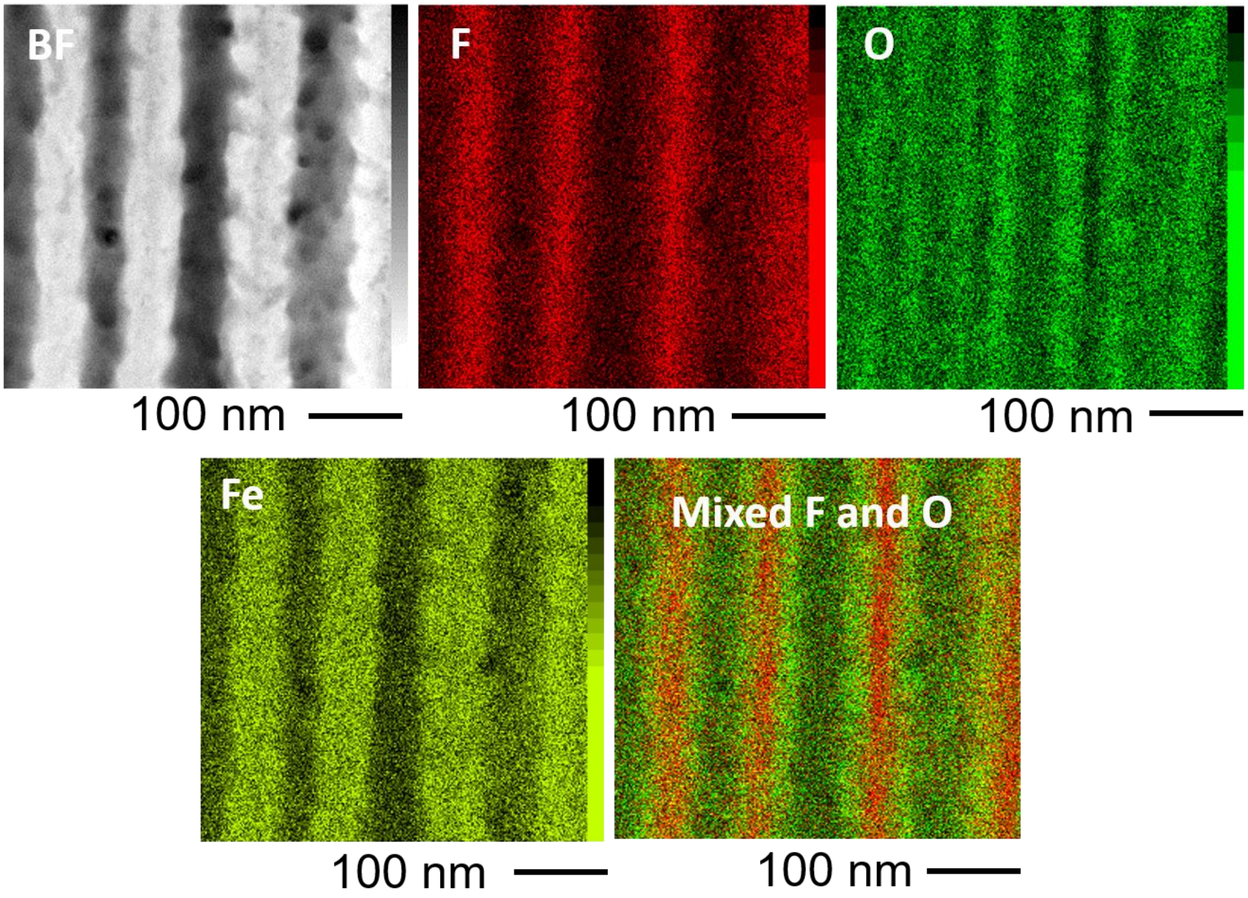

Figure 3.21 Bright field image and corresponding EDS maps of the middle region of FIB-treated anodic film formed on iron at 100 V in the ethylene glycol electrolyte containing 1.5 mol dm^{-3} water and 0.1 mol dm^{-3} ammonium fluoride at 293 K.

The TEM cross-sectional image of FIB treated anodic films at 40 V in the same electrolyte is shown in **Fig. 3.23**. The thickness of the anodic film is 2.71 μm. The bright field and EDS images in **Figs. 3.24 and 3.25** reveal that fluoride-rich cell boundaries are also formed at 40 V near the metal film/interface and in the bulk part of the anodic film. However, this enrichment is not clear at the outer disordered part of the anodic film as can be seen from the highlighted EDS image of fluorine in **Fig. 3.26**, therefore, nanoporous morphology instead of the nanotubular structure is developed at 40 V.

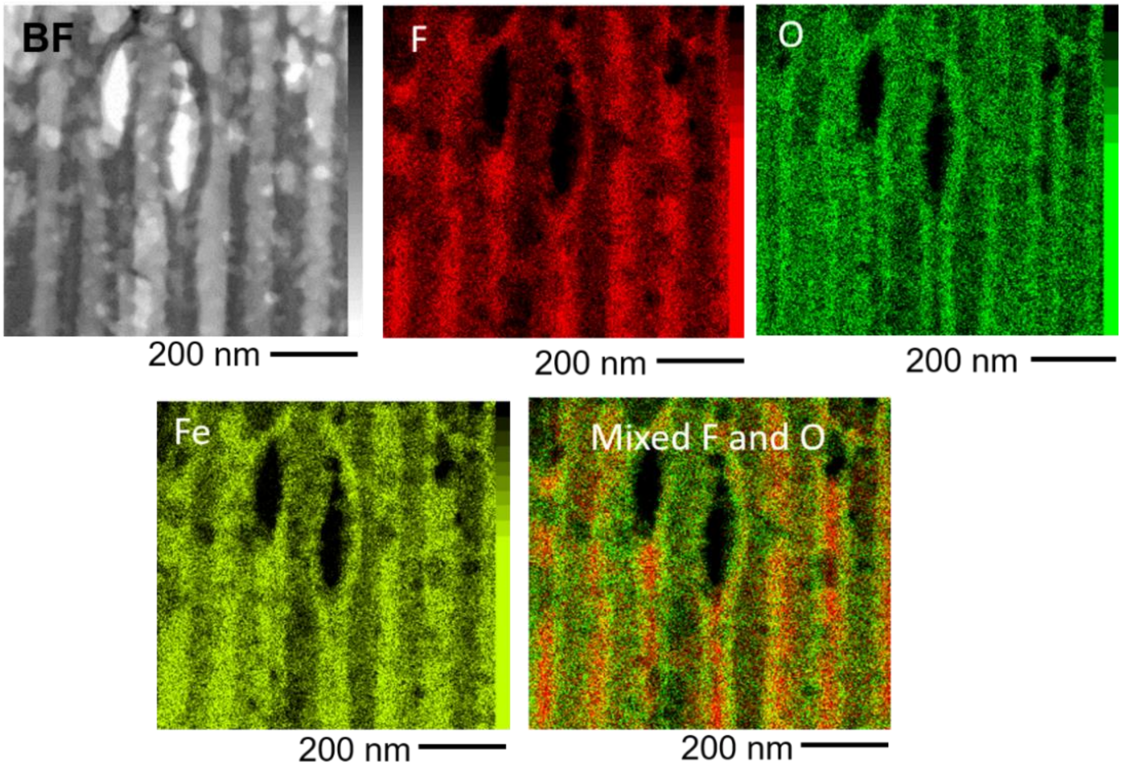

Figure 3.22 Bright field image and corresponding EDS maps of the outer region of FIB-treated anodic film formed on iron at 100 V in the ethylene glycol electrolyte containing 1.5 mol dm^{-3} water and 0.1 mol dm^{-3} ammonium fluoride at 293 K.

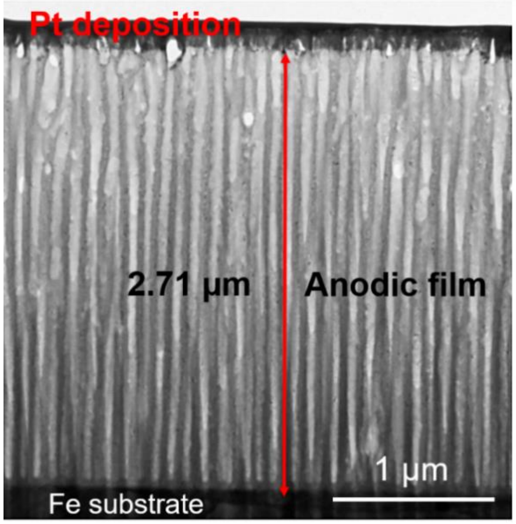

Figure 3.23 Transmission electron micrograph of FIB-treated anodic film formed potentiodynamically on iron at 40 V in the ethylene glycol electrolyte containing 1.5 mol dm^{-3} water and 0.1 mol dm^{-3} ammonium fluoride at 293 K.

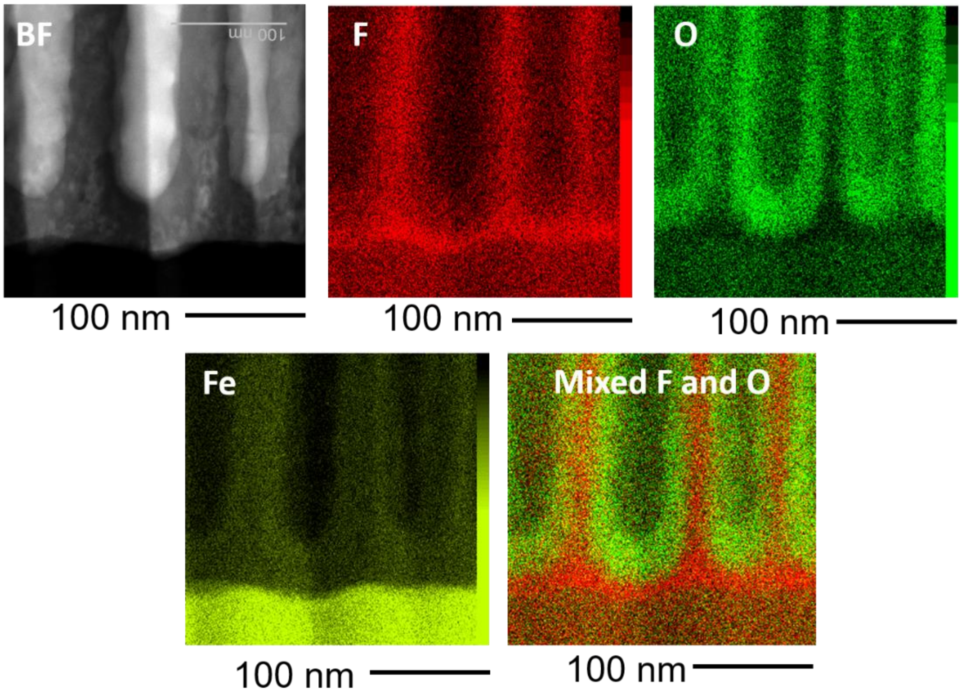

Figure 3.24 Bright field image and corresponding EDS maps of the bottom region of FIB-treated anodic film formed on iron at 40 V in the ethylene glycol electrolyte containing 1.5 mol dm^{-3} water and 0.1 mol dm^{-3} ammonium fluoride at 293 K.

As discussed above, porous film with flat metal/interface was developed below 1.5 mol dm^{-3} H_2O concentration. Distribution of fluoride-rich layer is further investigated at lower water concentrations of 0.1 and 0.5 mol dm^{-3} at 50 V as shown by TEM and EDS images in **Figs. 3.27** and **3.28**. The TEM cross-sections (**Figs. 3.27a and b**) show the barrier-type films sandwiched between the Fe substrate and porous-layer, while the outer light-region above the porous layer shows the platinum deposition prior to FIB. In agreement with SEM observations (**Fig. 3.6**), similar barrier layer thicknesses of ~120 nm and ~95 nm are examined at 0.1 mol dm^{-3} H_2O and 0.5 mol dm^{-3} H_2O concentrations respectively and cylindrical pore channels are not clearly seen at 0.1 mol dm^{-3} H_2O. Thus, it is difficult to precisely determine the barrier layer thickness at 0.1 mol dm^{-3} H_2O. From **Fig. 3.28a**, it is obvious that fluoride-rich layer is mainly accumulated near the metal/film interface beneath the pore bottom at 0.1 mol dm^{-3} H_2O concentration and is not present in the bulk of anodic film, while the fluoride-rich layer appears to be found at the cell boundaries and in the bulk film at 0.5 mol dm^{-3} H_2O concentration (**Fig. 3.28b**).

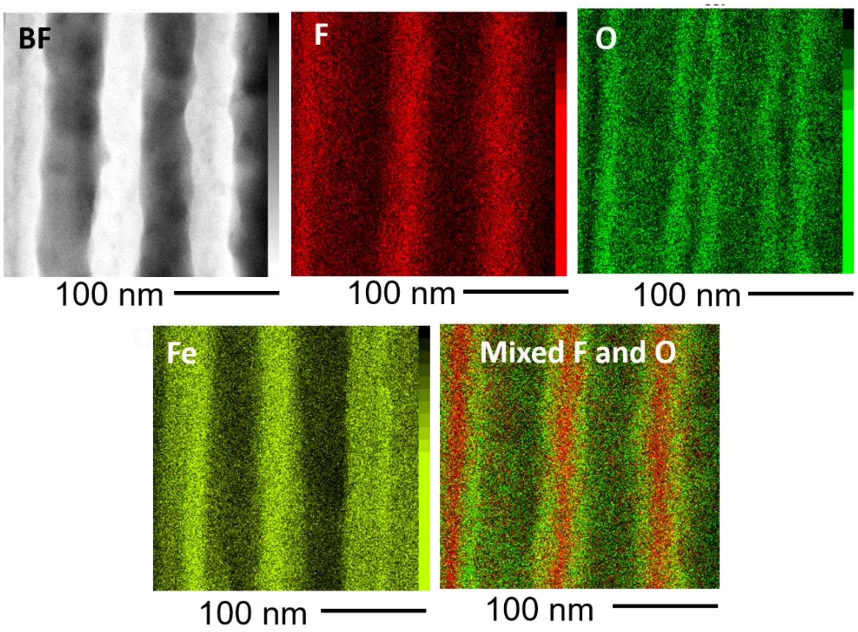

Figure 3.25 Bright field image and corresponding EDS maps of the middle region of FIB-treated anodic film formed on iron at 40 V in the ethylene glycol electrolyte containing 1.5 mol dm^{-3} water and 0.1 mol dm^{-3} ammonium fluoride at 293 K.

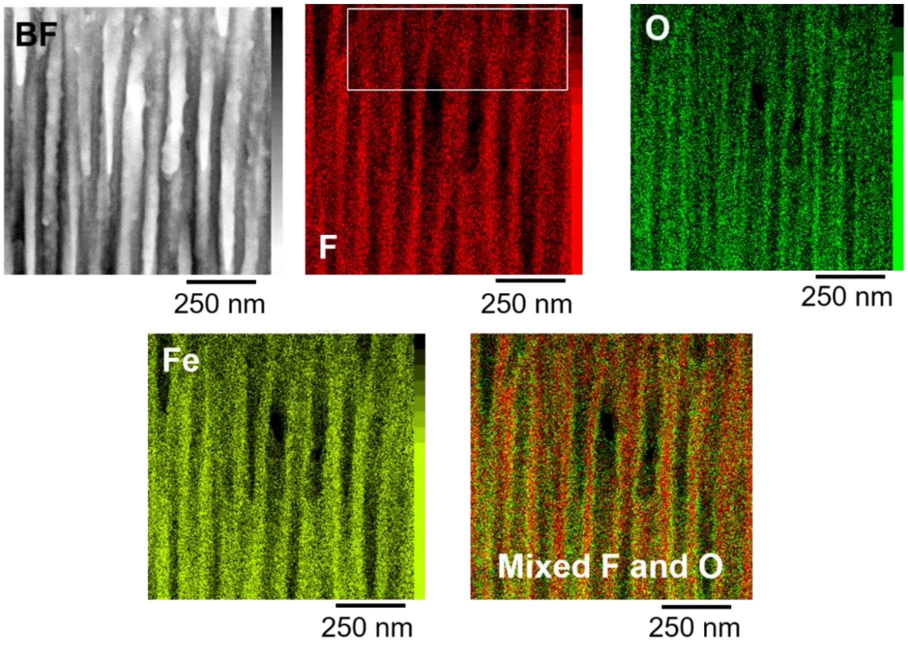

Figure 3.26 Bright field image and corresponding EDS maps of the outer part of FIB-treated anodic film formed on iron at 40 V in the ethylene glycol electrolyte containing 1.5 mol dm^{-3} water and 0.1 mol dm^{-3} ammonium fluoride at 293 K.

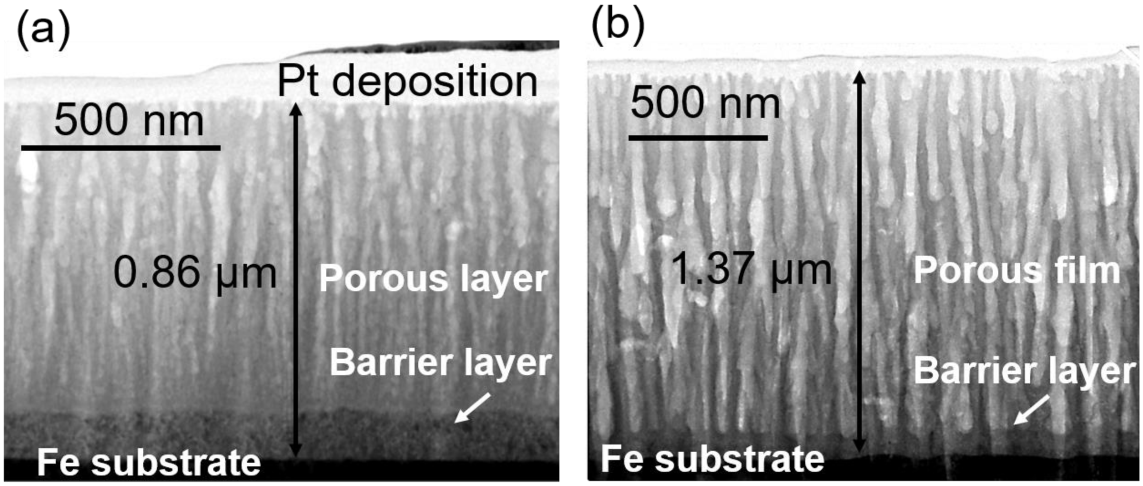

Figure 3.27 Transmission electron micrographs of FIB-treated anodic films potentiodynamically formed on iron at 50 V in the ethylene glycol electrolyte containing 0.1 mol dm^{-3} ammonium fluoride and (a) 0.1 (b) 0.5 mol dm^{-3} water at 293 K.

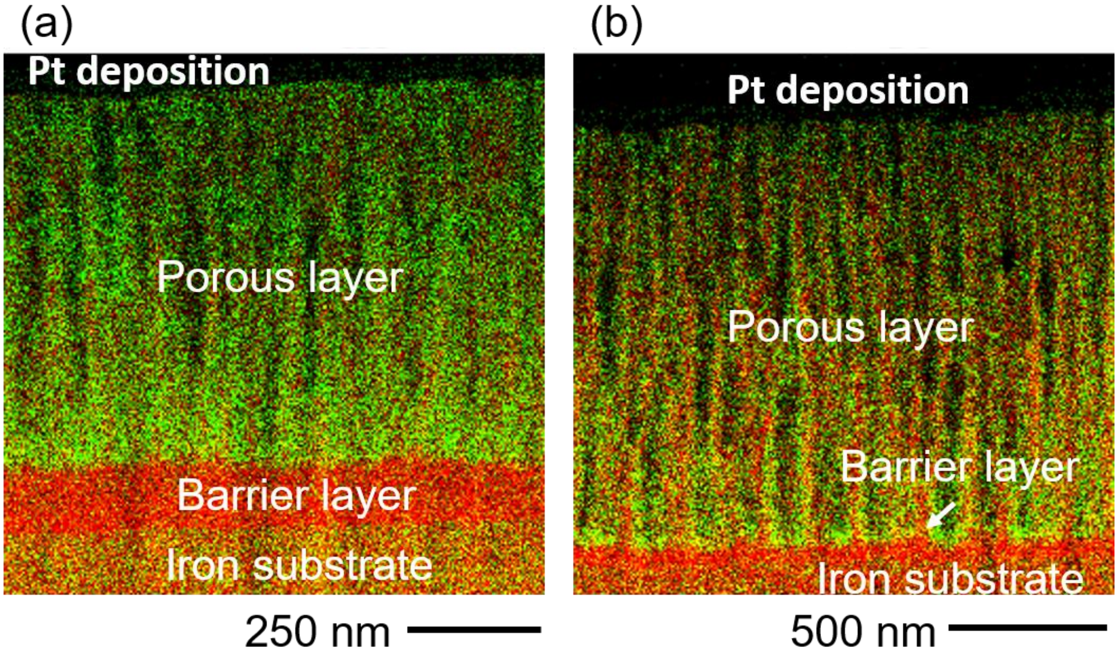

Figure 3.28 EDS images of FIB-treated anodic films formed potentiodynamically on iron at 50 V in the ethylene glycol electrolyte containing 0.1 mol dm^{-3} ammonium fluoride and (a) 0.1 (b) 0.5 mol dm^{-3} water at 293 K. The fluorine and oxygen maps are indicated as red and green colors respectively.

Enlarged bright field and EDS images in **Figs. 3.29a and b** reveal that thickness of the fluoride-rich layer is ~120 nm at 0.1 mol dm^{-3} H_2O and is reduced to ~54 nm at 0.5 mol dm^{-3} H_2O concentration (**Figs. 3.29c and d**), whereas this thickness was only ~15 nm at 1.5 mol dm^{-3} H_2O. It is likely that barrier layer thickness is more than 120 nm because of the fact fluoride-rich layer is mainly formed by the faster inwards migration of fluoride species compared with oxygen species. Therefore, it is probable that oxygen-containing barrier layer is also present next to 120 nm fluoride-rich layer. The accumulation of fluoride-rich layer at the metal/film interface is contrast to 1.5 mol dm^{-3} H_2O concentration, where the fluoride containing layer was uniformly distributed in the bulk of anodic film and thickness of fluoride-rich layer was only ~15 nm at 40 V. In other words, water concentration play a significant role in the distribution of fluoride-rich layer near the metal/film interface as well as in the bulk of the film.

3.6 Influence of anodizing time

Next, the influence of anodizing time on the film morphology was examined. This was performed by applying a relatively low current density of 300 A m^{-2} for the longer anodizing time of the 1200 s and 1800 s at 1.5 mol dm^{-3} H_2O. **Fig. 3.30** shows the similar *i-t* and *v-t* responses for the 1200 s and 1800 s at 1.5 mol dm^{-3} H_2O concentration as in **Fig. 3.17** at 300 A m^{-2}. As shown in **Fig. 3.18b**, the nanoporous film was obtained when the bulk iron sheet was anodized to 900 s at 300 A m^{-2}. However, when the iron sheets were anodized for a longer period of time at the same current density, nanotubular morphology are developed (**Figs. 3.31a and b**). This suggests that at low current density for relatively shorter anodizing time, less electric charge is available, resulting into the formation of porous film (**Fig. 3.18b**), while anodizing under similar conditions for longer anodizing time and with higher amount of electric charge induces the nanotubular structure (**Figs. 3.31a and b**).

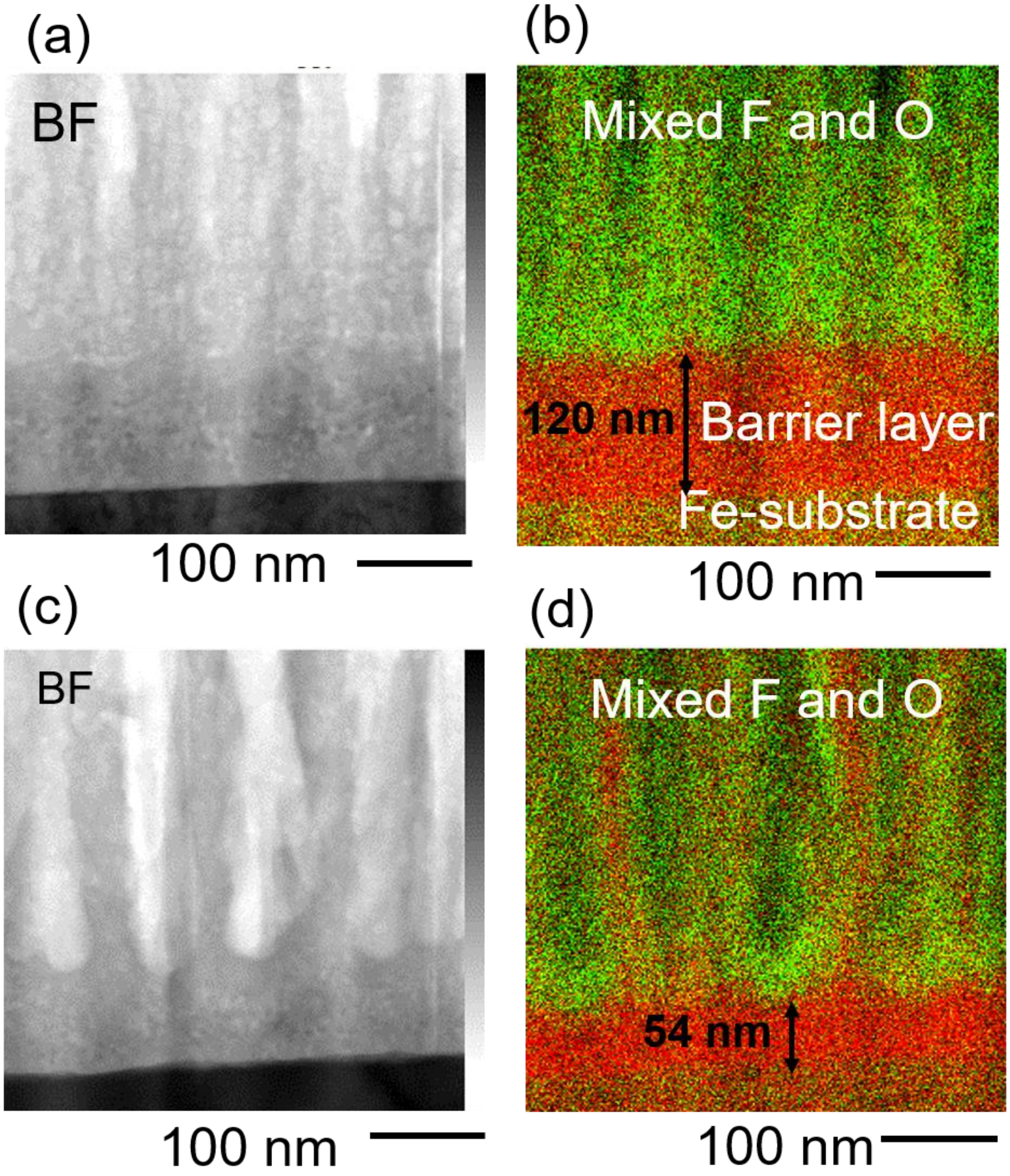

Figure 3.29 Bright field image and corresponding EDS maps of the FIB-treated anodic films formed on iron at 50 V in the ethylene glycol electrolyte 0.1 mol dm^{-3} ammonium fluoride and (a) 0.1 mol dm^{-3} water, and (b) 0.5 mol dm^{-3} water at 293 K. The fluorine and oxygen maps are indicated as red and green colors respectively.

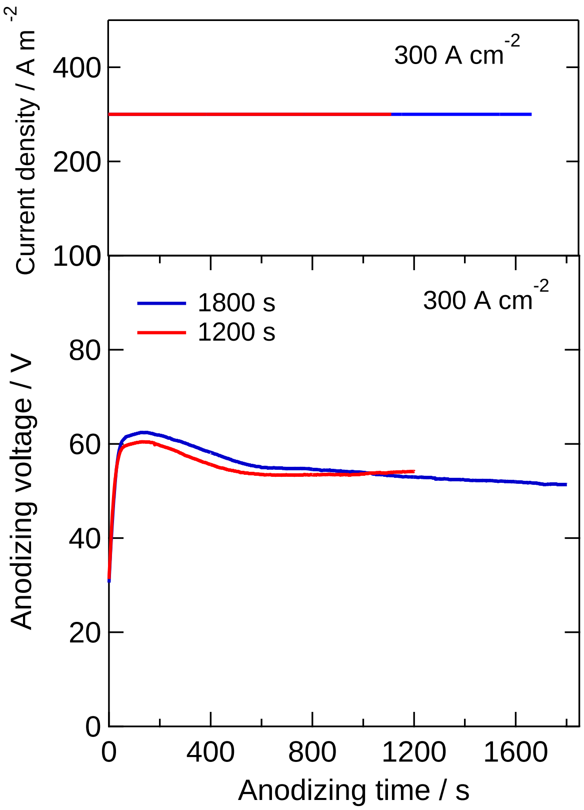

Figure 3.30 *i*-*t* and *v*-*t* curves of the anodic films formed to 300 A m^{-2} for 1200 s and 1800 s in the ethylene glycol containing 1.5 mol dm^{-3} water and 0.1 mol dm^{-3} ammonium fluoride at 293 K.

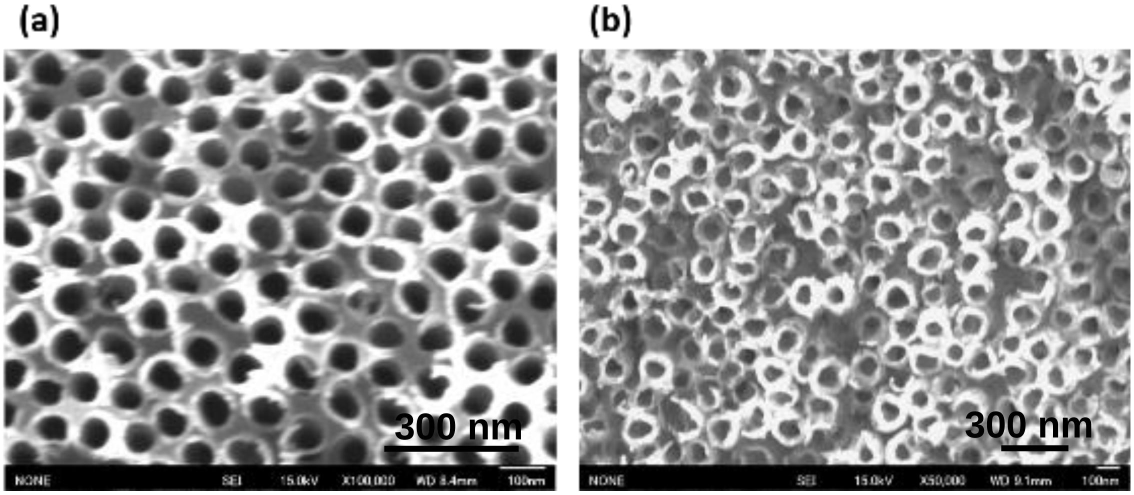

Figure 3.31 Scanning electron micrographs of the anodic films formed on iron at 300 A m^{-2} for 1200 s and 1800 s respectively in the ethylene glycol electrolyte containing 1.5 mol dm^{-3} water and 0.1 mol dm^{-3} ammonium fluoride at 293 K.

3.7 Discussion

The present work shows the formation of iron-based nanoporous and nanotubular anodic films in fluoride containing organic electrolytes and clearly reveals the presence of fluoride-rich layer at the cell boundaries of porous structure for the first time. The direct evidence of fluoride-rich layer and dissolution of such layer near the surface strongly support that dissolution of fluoride-rich layer is the key reason for the nanoporous to nanotubular transition over some other concepts of tube formation. At 1.5 mol dm^{-3} H_2O concentration, although the fluoride-rich layer is present throughout the film thickness at 100 V, but the fluoride-enriched layer in outer part of the film is unclear at 40 V. An irregular anodic film without fluoride-rich cell boundaries may be developed initially at 40 V. Such irregular initially formed outer layer prevents the transition from nanoporous to nanotubular morphology. Thus, no nanotubular film was formed before the irregular outer layer was dissolved chemically during anodizing. At 100 V, electrolyte temperature increased because of high Joule heating and chemical dissolution of the initially formed outer layer. Thus, nanotubular films were developed at shorter anodizing time when anodizing voltage was as high as 100 V.

More significant influence on film morphology appeared by the addition of water in electrolyte. As discussed above, water concentration influences the composition and electric field strength. The water concentration also influences the distribution of fluoride-rich layer within the anodic film. At 0.1 mol dm^{-3} H_2O concentration (**Fig. 3.28a**), fluoride-rich layer is only present near the metal/film interface without any enrichment at the cell boundaries in the bulk anodic film. Further increase in water concentration to 0.5 mol dm^{-3} causes the fluoride enrichment at cell boundaries near the metal/film interface as well as in the bulk of film (**Fig. 3.28b**), but the enrichment is not uniform and apparently absent at the outer region of the anodic film. As a consequence, no preferential dissolution of such layer occurs near film surface and hence the formation of nanotubes is not possible. Thus, only porous film is developed at low water concentration, indicating that water concentration is also critical for the formation of nanotubes. A relatively thick (~120 nm) fluoride-rich layer was developed in the inner layer immediately above the metal/film interface at 0.1 mol dm^{-3} H_2O. It was reported that fluoride migrates faster than oxide ions in growing anodic films on aluminum, titanium, niobium and tantalum [22-24]. Thus, it is likely that even in anodic films on iron fluoride migrates faster than oxide ion, forming fluoride-enriched layer immediately above the metal/film interface. When H_2O concentration is increased, the thickness of the fluoride-rich layer immediately above the metal/film interface became thinner and the enriched layer extended to the cell boundaries in the porous layer. Thus, the distribution of the fluoride in the anodic film changed largely with H_2O concentration. As mentioned above, there are two main mechanisms for the formation of porous anodic alumina: field-assisted dissolution and field-assisted flow [14, 25-26]. From the distribution of fluoride in the anodic films as well as the morphology of the metal/film interface, the growth mechanism appears to change from field-assisted dissolution to field-assisted flow with the H_2O concentration.

A schematic illustration of the change in film morphology with water concentration is demonstrated in **Fig. 3.32**, which indicates unusual flat metal/film interface with a thicker barrier layer at lower water concentrations ≤ 1 mol dm^{-3} H_2O (**Fig. 3.32a**). The relatively small cell size compared with barrier layer thickness hinders the film formation by plastic flow as mentioned above, whereas at water concentrations ≥ 1 mol dm^{-3} H_2O, films with larger cell size compared with barrier layer thickness are obtained (**Fig. 3.32b**) and it is probable that film growth might proceeds by flow of film materials towards cell walls rather than field assisted dissolution. Furthermore, nanotubular morphology is developed from porous base only at anodizing voltages ≥ 60 V by the preferential chemical dissolution of fluoride-rich layer as film at cell boundaries comprises of fluoride-rich material due to differing in the migration rates of the fluoride species and oxide ions.

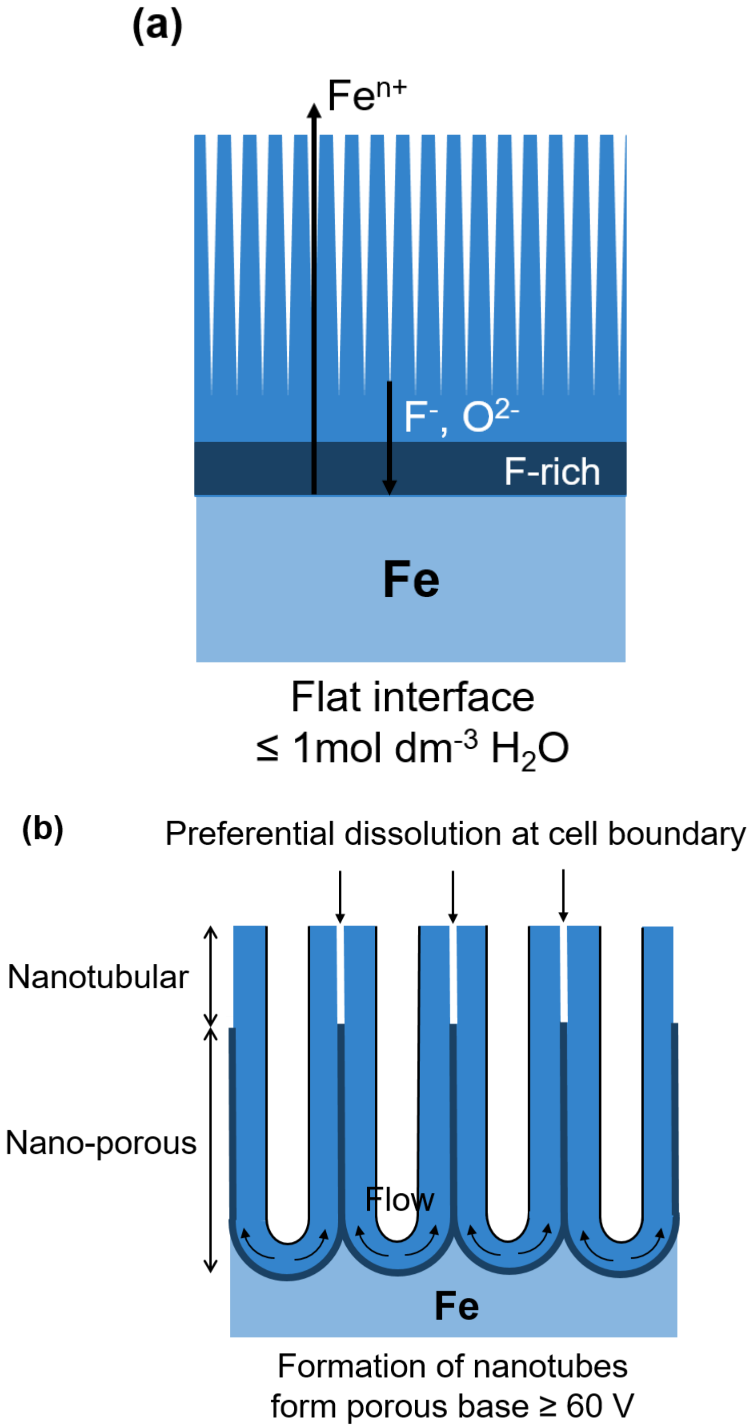

Figure 3.32 Schematic illustrations of the change in film morphology of the anodic films on iron in the ethylene glycol electrolytes containing 0.1 mol dm^{-3} ammonium fluoride (a) flat metal/film interface at water concentration ≤ 1 mol dm^{-3} water, (b) scalloped metal/film interface at water concentration ≥1 mol dm^{-3} water and formation of nanotubes at cell boundaries ≥ 60 V.

3.8 Conclusions

1. Film morphology, composition, and structure of anodic films are largely influenced by water concentration. Thicker anodic films are developed by increasing water concentration up to 1.5 mol dm^{-3} in anodizing of iron at 50 V for 15 min, although the film thickness is reduced at 2.0 mol dm^{-3} water despite a further increase in the electric charge during anodizing. The reduced thickness at this water concentration is associated with enhanced chemical dissolution and gas evolution.
2. The ratio of interpore distance to the barrier layer thickness increases with water concentration. Typical scalloped metal/film interface is developed only when the water concentration is at and above 1.5 mol dm^{-3}.
3. Water concentration plays an important role in the distribution of fluoride-rich layer at the cell boundaries within the anodic film and the distribution and dissolution of the fluoride-rich layer is critical for the transition of nanoporous to nanotubular morphology. Certain anodizing conditions such as voltage, temperature and anodizing time accelerates the dissolution of the fluoride-enriched layer.
4. The reduced thickness of fluoride-rich layer near the metal/film interface and the development of scalloped metal/film interface at 1.5 mol dm^{-3} water may suggest that growth of oxide proceeds by field-assisted flow with the increase in water concentration.

References:

[1] H. Habazaki, Y. Konno, Y. Aoki, P. Skeldon and G. E. Thompson, *J. Phys. Chem. C,* **114,** 18853 (2010) 18853.

[2] Y. Konno, E. Tsuji, P. Skeldon, G. E. Thompson, H. Habazaki, *J. Solid State Electrochem.*, **16**, 3887 (2012).

[3] F. Muratore, A. Baron-Wiechec, A. Gholinia, T. Hashimoto, P. Skeldon, G.E. Thompson, *Electrochem. Acta,* **58**, 389 (2011).

[4] A. Valota, D.J. LeClere, P. Skeldon, M. Curioni, T. Hashimoto, S, Berger, J. Kunze, P. Schmuki, G. E. Thompson, *Electrochem. Acta,* **54**, 4321 (2009).

[5] J. M. Macak, H. Hildebrand, U. Marten-Jahns, P. Schmuki, *J. Electroanal. Chem.,* **621**, 254 (2008).

[6] J. Zhao, X. Wang, R. Xu, F. Meng, L. Guo, Y. Li, *Mater. Lett.,* **62 (29)**, 4428 (2008).

[7] Raghu R. Rangaraju, K.S. Raja, A. Panday, M. Misra, *Electrochim. Acta,* **55**, 785 (2010).

[8] Thomas J. LaTempa, Xinjian Feng, Maggie Paulose, and Craig A. Grimes, *J. Phys. Chem. C,* **113**, 16293, (2009).

[9] S.P. Albu, A. Ghicov, P. Schmuki, *Phys. Status Solidi Rapid Res. Lett.,* **3**, 64 (2009).

[10] Poulomi Roy, Steffen Berger, Patrik Schmuki, *Angew. Chem. Int. Ed.,* **50**, 2904 (2011).

[11] H. Tsuchiya, J. M. Macak, L. Taveira, P. Schmuki, *Chem. Phys. Lett.*, **410 (4-6)**, 188 (2005).

[12] H. Tsuchiya, P. Schmuki, *Electrochem. Commun.,* **6 (11)**, 1131 (2004).

[13] F. Keller, M. S. Hunter and D. L. Robinson, *J. Electrochem. Soc.,* **100**, 411 (1953).

[14] J. P. O'Sullivan and G. C. Wood, *Proc. R. Soc. London, A* **317**, 511 (1970).

[15] J. Oh and C. V. Thompson, *Electrochim. Acta*, **56**, 4044 (2011).

[16] S. J. Garcia-Vergara, L. Iglesias-Rubianes, C. E. Blanco-Pinzon, P. Skeldon, G. E. Thompson and P. Campestrini, *Proc. Royal Soc. A,* **462**, 2345 (2006).

[17] P. Skeldon, G. E. Thompson, S. J. Garcia-Vergara, L. Iglesias-Rubianes and C. E. Blanco-Pinzon, *Electrochem. Solid State Lett.*, **9**, B47 (2006).

[18] Satoshi Kaneco, Yongsheng Chen, Paul Westerhoff, John C. Crittenden, *Scripta Materialia* **56**, 373 (2007).

[19] J. M. Macak, H. Tsuchiya, P. Schmuki, *Angew. Chem. Int. Ed.,* **44**, 2100 (2005).

[20] S. P. Albu, A. Ghicov, S. Aldabergenova, P. Drechsel, D. LeClere, G. E. Thompson, J. M. Macak, P. Schmuki, *Adv. Mater.,* **20**, 4135 (2008).

[21] S. Berger, J. Kunze, P. Schmuki, A. T. Valota, D. J. Leclere, P. Skeldon, G. E. Thompson, *J. Electrochem. Soc.,* **157**, C18 (2010).

[22] K. Shimizu, K. Kobayashi, G. E. Thompson, P. Skeldon, G. C. Wood, *Philosophical magazine B,* **73 (3)**, 461 (1996).

[23] H. Habazaki, K. Fushimi, K. Shimizu, P. Skeldon, G.E. Thompson, *Electrochem. Commun.,* **9**, 1222 (2007).

[24] K. Shimizu, H. Habazaki, P. Skeldon, G.E. Thompson, G.C. Wood, *Electrochim. Acta,* **45**, 1805 (2000).

[25] S. J. Garcia-Vergara, P. Skeldon, G. E. Thompson and H. Habazaki, *Electrochim. Acta,* **52**, 681 (2006).

[26] J. E. Houser and K. R. Hebert, *Nat. Mater.*, **8**, 415 (2009).

Chapter 4

Formation and field-assisted dissolution of anodic films on iron

4.1 Introduction

Because of practical importance and of fundamental interest in the film growth mechanism, nanoporous oxide films formed by anodic polarization of valve metals such as Al, Ti, W, Ta, Zr, and Nb have been extensively explored in the last two decades in terms of controlled variation in electrochemical parameters to achieve the desired morphology, thickness and functionality. These films have potential applications for corrosion protection, super-capacitors, as templates for the fabrication of variety of nanostructures, and in batteries, solar cells, various energy conversion devices [1–4]. As mentioned in chapter 1, there are three general type of anodic films: barrier-type, nanoporous-type, and nanotubular type. The compact barrier-type films are usually formed when the growth proceeds at high efficiency. When the films are amorphous, new film materials are developed both at the film/electrolyte and metal/film interfaces by migration of cations outwards and anions inwards, respectively, in a corporative manner [5]. Under certain anodizing conditions, barrier films are transformed into the porous anodic films and factors such as temperature, time of anodizing, and current density have been reported to influence the morphology of the resultant films [6].

In contrast to the barrier layer, the formation behavior of self-organized porous oxide films has attracted much attention in recent years. It is well accepted that the porous anodic films are formed when new film material is formed only at the metal/film interface, and cation species migrating outwards are ejected directly to the electrolyte at the film/electrolyte interface [6]. Porous oxide films are formed in solutions which promotes the dissolution of oxide under constant anodic voltage (potentiostatic mode) or a constant anodic current density (galvanostatic mode). Most recent studies have focused on the understanding of the mechanism of pore generation, and efforts have been made to resolve the causes of field-induced and stress-induced instabilities at the film/electrolyte interface, leading to pore formation [7-10]. It is generally presumed that pores are initiated at rough film/electrolyte interface under the field, where the electric field is non-uniformly concentrated at the troughs of the film/electrolyte interface. Various mechanisms have been proposed for the growth of porous oxides over the past 50 years, namely (a) field-induced dissolution (b) field-assisted ejection and (c) field-assisted plastic flow [6, 8, 11, 12]. In the field assisted dissolution model, first proposed by Hoar and Mott [13], it is presumed that generation of pores is associated with the dynamic equilibrium between the rate of oxide formation at the metal/film interface and the dissolution of oxide at the film/electrolyte interface and the dissolution rate is enhanced in the presence of electric field, while the barrier layer beneath the porous film stops growing as thickening of the oxide decreases the electric field across the oxide. Most of the previous investigations in the field-assisted dissolution model assumed that steady-state film growth kinetics occurred due to accelerating dissolution of oxide film under the influence of high external electric field at the pore base [6, 11, 13, 14]. Local joule heating at the base of pores was also suggested for increased dissolution rates of the oxide [14]. The reduced current efficiency of ~ 60 % in certain anodizing electrolytes with a typical porosity of 10 -20% for porous anodic alumina suggests the direct dissolution of metal cations into the electrolyte under high field by the mechanism of field-assisted ejection. This mechanism although is not associated directly with pore formation, the direct ejection of cations to the electrolyte through the film provide nucleation sites for subsequent porous film development [6].

Relatively recently, Garcia *et al*. have proposed that generation and growth of porous anodic structure on aluminum is associated with the field-assisted flow of oxide material by the distribution of compressive stresses [12, 15-18]. Through a series of tracer experiments, they concluded that pores are generated by the plastic flow of material from pore base towards cell walls in certain electrolytes. In parallel, Hebert and co-workers have supported their flow model using computational approach [8, 19].

In both field-assisted dissolution and field-assisted flow models, the electric field applied to the barrier layer sandwiched between the porous layer and metal substrate exhibits a crucial role. Direct experimental evidence for the influence of electric field on dissolution and pore initiation and the presence of critical field for pore initiation during anodizing of aluminum have been demonstrated recently by Oh and Thomson [9]. They showed that uniform thinning of oxide film occurs below a field of 7.46 MV cm^{-1} and the field induced instability and pore initiation starts at the critical field. The mechanical instability that leads to major pore formation commences at 8.9 MV cm^{-1}.

As mentioned above, the porous anodic films can now be formed on a range of metals. Fluoride-containing organic electrolytes with a small amount of water have been often used for the formation of porous anodic films on titanium [20], zirconium [21], niobium [22], and iron [23-27]. The nanoporous and nanotubular anodic films formed on iron have attracted attention owing to their future promising applications, including photoanode for water splitting, electrodes for lithium ion batteries, gas sensors, and electrodes for electrochemical capacitors [27-32]. Despite extensive investigations on the mechanism of porous film formation on aluminum, the studies on the formation mechanism of the porous anodic films on iron have been still very limited [23-25].

In the present study, first we formed barrier-type and nanoporous-type anodic films on iron by potentiodynamic anodizing in ethylene glycol (EG) electrolyte containing ammonium fluoride and water and their formation behavior was examined. Then, the influence of electric field on the dissolution rate of anodic films on iron was investigated by applying an electric field to the pre-formed barrier-type anodic film in order to elucidate the crucial role of the electric field in anodizing of iron.

4.2 Results and Discussion

4.2.1 Potentiodynamic growth of anodic films

The iron thin films, ~ 460 nm thick, deposited on glass or anodized aluminum substrate by magnetron sputtering were anodized to 50 V potentiodynamically at 1.0 and 0.05 V s^{-1} in the EG electrolyte containing 0.1 mol dm^{-3} ammonium fluoride and 0.1 mol dm^{-3} H_2O at 273 K. The typical current-voltage responses are shown in **Fig. 4.1.** Initially, the current density increases approximately linearly to a current peak, followed by a current decrease to a steady-state current density. At the potential sweep rate of 0.05 V s^{-1}, a second small current peak appears at 12 V, in addition to the first higher current peak at 4 V. Assuming that uniform thickening of the anodic film occurs, the growth of the barrier anodic film can be described by the following equation,

$$\frac{dV}{dt} = E\frac{dh}{dt} \qquad (4\text{-}1)$$

in which *V* is the applied voltage, *t* is the anodizing time, *E* is the electric field across the anodic film and *h* is the thickness of the anodic film. Considering Faraday's law, the following equation can be described,

$$\frac{dV}{dt} = \frac{\eta EMi}{zF} \qquad (4\text{-}2)$$

in which η is the current efficiency for film growth, *M* is the molar volume, *i* is the anodizing current, *z* is the equivalent number and *F* is the Faraday's constant. This equation suggests that under a constant potential sweep rate (d*V*/d*t* = constant), current becomes constant under a steady state condition, as in the case of **Fig. 4.1.** The presence of a current peak at a low voltage region during potentiodynamic anodizing has been often found in anodizing of valve metals. The phenomenon was well discussed in a review paper by Lorengel [33] and explained in terms of a delayed oxide formation.

Although there are only limited studies on anodic film growth under potentiodynamic conditions, Curioni *et al*. anodized high purity aluminum potentiodynamically in sulfuric acid electrolyte [34]. In contrast to the observation of the steady-state current in the present study, they found a continuous current increase above a narrow plateau potential region less than 3 V. This was interpreted by the flow model, which was valid in anodizing of aluminum in sulfuric acid [7, 35]. Because of the flow of film material, a part of anodic oxide generated at the metal/film interface is displaced to the cell walls. The displacement tends to reduce the thickness of the barrier layer, contributing to the increase in the electric field and the current density. Even though a porous film is formed at the low potential sweep rate as indicated below, the absence of such continuous current increase at 50 V in the present study may suggest that the flow model is not applicable in the present condition.

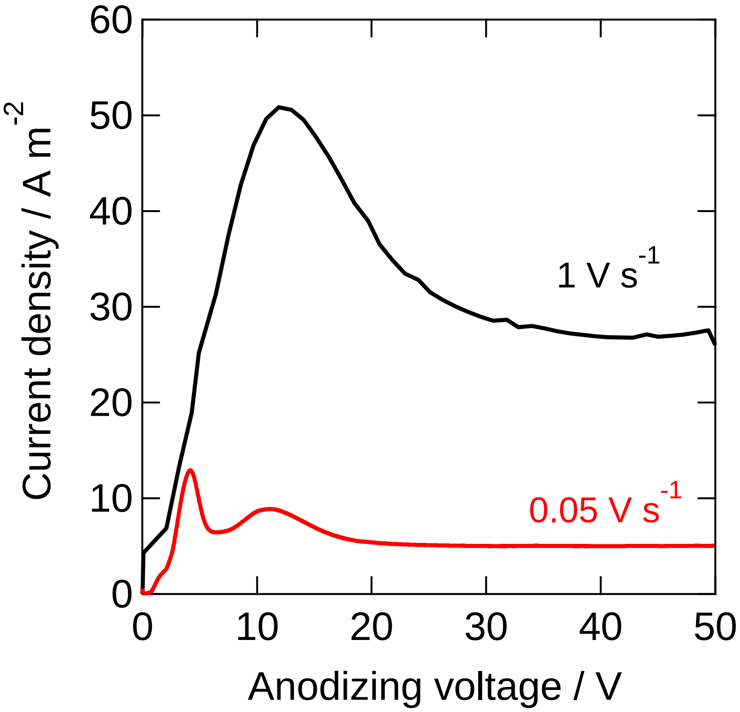

Figure 4.1 *I-V* responses of the magnetron-sputtered iron films at potential sweep rates of 0.05 and 1.0 V s^{-1} in the EG electrolyte containing 0.1 mol dm^{-3} ammonium fluoride and 0.1 mol dm^{-3} H_2O at 273 K.

4.2.2 Film morphology

Fig. 4.2 shows the scanning electron micrographs of surfaces of the magnetron-sputtered iron films as-deposited and anodized to 50V at 0.05 and 1.0V s^{-1}. Associated with the columnar structure of the as-deposited film, relatively rough surface is observed in **Fig. 4.2a.** The apparent grain size (column width) is 50-100 nm. Similar surface morphology is observed after anodizing to 50 V at 1.0 V s^{-1} (**Fig. 4.2b**), with troughs along with grain boundaries, although the surface appears to be smoother within grains. For the iron film anodized at the low sweep rate (**Fig. 4.2c**), nanopores are developed with the average pore size being ~10 nm. The nanopores are formed preferentially at the trough region of the rough surface. A similar result was reported previously in anodizing of carbon steel [36] as well as aluminum [2].

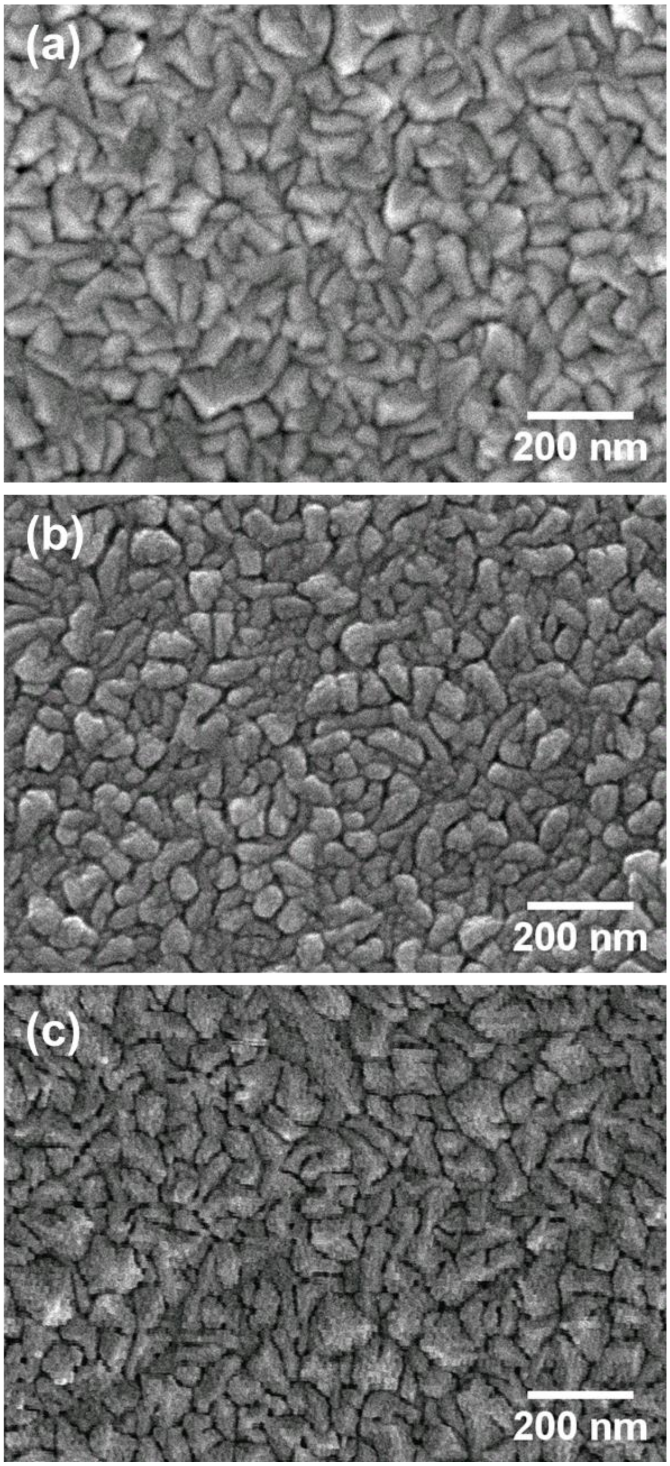

Figure 4.2 Scanning electron micrographs of surfaces of the magnetron-sputtered iron films (a) as-deposited and anodized to 50V at sweep rates of (b) 1.0 and (c) 0.05V s^{-1} in an EG electrolyte containing 0.1 mol dm^{-3} ammonium and 0.1 mol dm^{-3} H_2O at 273K.

The formation of a barrier-type anodic film at the high sweep rate of 1.0 V s^{-1} is confirmed from the scanning electron micrograph of a cross-section of the anodized iron specimen (**Fig. 4. 3a**). On the sputtered-iron layer with a columnar structure, a compact anodic film of 100 ± 5 nm thickness is developed. The metal/film interface is relatively flat, while the film/electrolyte interface is still rough, although barrier-type films formed at high current efficiency usually have a flat film/electrolyte interface. A similar rough film/electrolyte interface and/or a thin porous layer above a barrier layer was found when aluminum was anodized to 40 V potentiodynamically in the tartaric acid electrolyte, in which no film material was formed at the film/electrolyte interface due to the direct ejection of outwardly migrating Al^{3+} ions [37]. As discussed later, no film material is formed at the film/electrolyte interface because of the low current efficiency in the formation of the present barrier-type anodic film on iron. In the anodic film formed at the low sweep rate, cylindrical nanopores channels are developed (**Fig. 4.3b**). The thickness of the anodic film is 400 ± 7 nm and the barrier layer, sandwiched between the porous layer and iron substrate, has a thickness of 72 ± 5 nm, which is slightly thinner than that formed at the high sweep rate. The interpore distance is ~ 60 nm. In anodizing of aluminum in acid electrolytes, the interpore distance is controlled by the formation voltage (2.5-2.8 nm V^{-1}) [14]. Since the thickness of the barrier layer beneath the porous alumina layer is ~1.0 nm V^{-1}, the interpore distance of the porous layer for porous anodic alumina is 2.5-2.8 times the thickness of the barrier layer. Compared with the morphology of the porous alumina films, the interpore distance in the porous film on iron is too small with respect to the thickness of the barrier layer. The interpore distance of the anodic film on iron appears to be similar to the column width of the deposited iron. Considering the preferential formation of pores at the trough region of the as-deposited iron surface, it is likely that the interpore distance is controlled by the morphology of iron surface, not the anodizing parameters under the present anodizing condition. Field-assisted dissolution, rather than field-assisted flow, appears to be dominant in growing the porous films on iron under the present condition.

4.2.3 Film composition

The depth profile analysis of the anodic films formed at a sweep rate of 1 V s^{-1} and 0.05 V s^{-1} was examined by GDOES to get the compositional information as shown in **Fig. 4.4**. The anodic films contain fluorine, derived from fluoride species in the electrolyte, and carbon species, derived from

EG, in addition to oxygen, which may be originated from water added to the electrolyte. It is clear that both oxygen and fluorine are distributed throughout the film thickness and high enrichment of fluorine is also obvious near metal/film interface. The sputtering time to metal/film interface is shorter for the anodic film formed at 1 V s^{-1} and is in full agreement with the thickness of anodic films by SEM (**Fig. 4.3**).

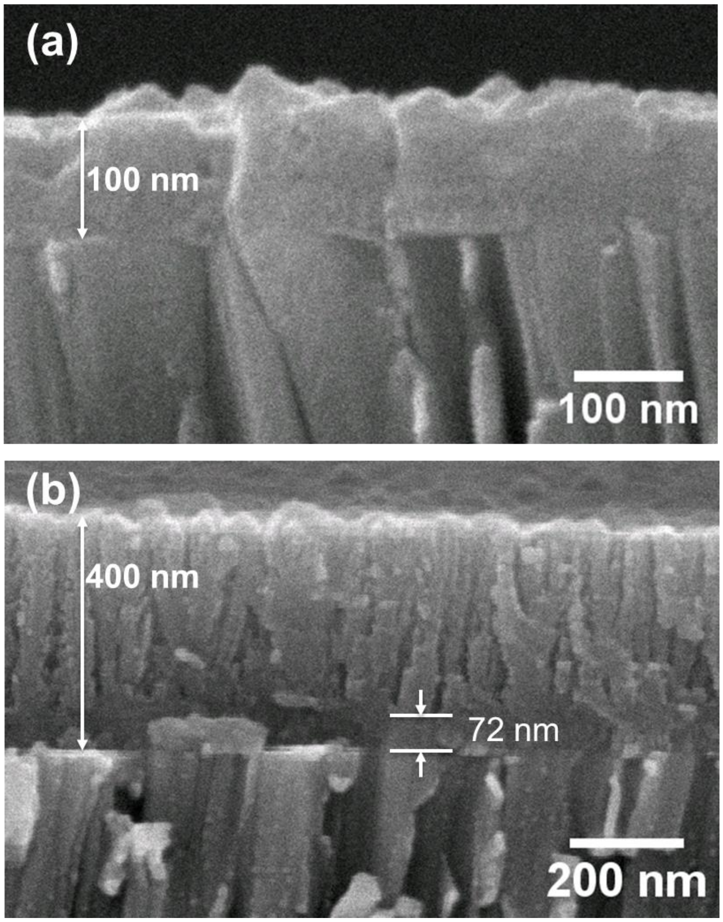

Figure 4.3 Scanning electron micrographs of cross-sections of the magnetron-sputtered iron films anodized to 50 V at sweep rates of (a) 1.0 and (b) 0.05 V s^{-1} in an EG electrolyte containing 0.1 mol dm^{-3} ammonium fluoride and 0.1 mol dm^{-3} H_2O at 273 K.

The compositions of the anodic films formed on iron were further examined by RBS. **Fig. 4.5** shows the experimental and simulated RBS spectra of the iron films as-deposited and anodized to 50 V at the sweep rates of 1.0 and 0.05 V s^{-1}. The RBS spectrum of the as-deposited iron (**Fig. 4.5a**) shows yields from iron, aluminum and oxygen, with the latter two arising from the anodized aluminum substrate. In **Fig. 4.5b** yields from fluorine and oxygen in the anodic film appear separately from the other yields, and higher yield of fluorine in comparison with oxygen indicates that the anodic film is fluoride-rich.

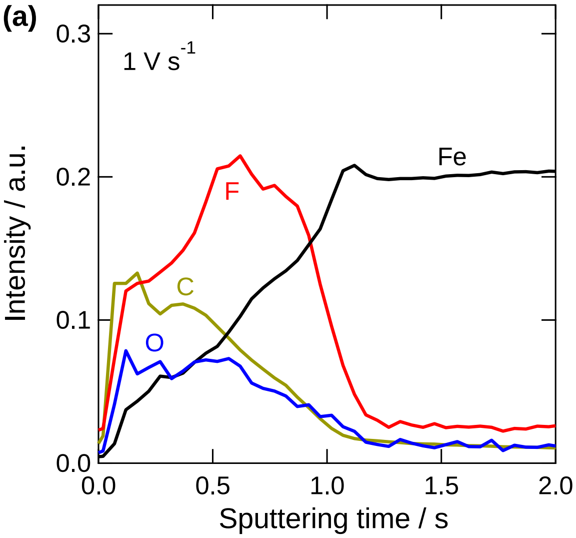

Figure 4.4 GDOES depth profile analysis of anodic films formed on the iron sheet at a sweep rate of (a) 1 V s^{-1} (b) 0.05 V s^{-1} in the EG electrolyte containing 0.1 mol dm^{-3} ammonium fluoride and 0.1 mol dm^{-3} H_2O at 273 K.

In **Fig. 4.5c**, the yield from oxygen appears again, but the yield from fluorine is overlapped with that from iron. The precise compositions of the anodic films were examined by simulation. The simulated spectra shown in **Figs. 4.5b and 4.5c**, obtained using the compositions, density, and thicknesses of individual layers in **Table 4.1**, are fitted well with the respective experimental spectra. In the simulation, probable incorporation of carbon species derived from EG into the anodic films was neglected, due to the low sensitivity of RBS for carbon. The anodic film formed at the high sweep rate consists of two layers; the outer layer is composed of iron (III) hydroxy-fluoride or hydrated oxyfluoride and the inner layer is iron (III) fluoride. The formation of the inner fluoride layer may be associated with the faster inward migration of fluoride ions compared with oxygen species, as reported previously [25]. The faster migration of fluoride in growing barrier-type anodic films has also been reported in anodizing of tantalum [38] and titanium [39]. The outer layer of the present barrier-type anodic film is composed of a hydrated oxide or contains hydroxide. Since the anodic film formed under the present condition was soluble in water, there would be a possibility that the hydration proceeded in laboratory air after anodizing, not during anodizing. The porous anodic film formed at the low sweep rate has also compositionally layered structure. The porous layer, 328 nm thick, is composed of hydrated hydroxy-fluoride and the barrier layer of 72 nm thickness. Both the layers have compositions similar to the respective layers formed at the high sweep rate.

From the comparison of the RBS spectra as-deposited and anodized to 50 V, the thicknesses of the iron films consumed by anodizing were 40 ± 3 and 75 ± 3 nm at the high and low sweep rates, respectively. The schematic illustration of film thickness and composition by RBS simulation is shown in **Fig. 4.6**. Assuming that iron was oxidized to Fe (III) state, the respective electric charges required for the oxidation of iron were 0.16 ± 0.02 and 0.31 ± 0.02 C cm^{-2}, as shown in **Table 4.2**. The electric charges passed during anodizing to 50 V at the high and low sweep rates were 0.15 ± 0.01 and 0.57 ± 0.02 C cm^{-2}, respectively. It is obvious from these results that the electric charge passed during anodizing was used predominantly for oxidation of iron at the high sweep rate, while it reduces to 54% at the low sweep rate. During anodizing at the low sweep rate, gas generation was observed to a minor extent from the specimen surface, contributing to the reduction of the efficiency for oxidation of iron. The probable presence of gas bubbles in the barrier layer may also contribute to the reduction of the barrier layer thickness (~72 nm) in comparison with that at the high sweep rate. The electric charge used for the formation of anodic films was also calculated from the number of iron (III) ions in the anodic films and then the current efficiency for film formation was estimated (**Table 4.2**). Although the barrier-type film is formed at the high sweep rate, the current efficiency is only 49%. It is likely that film materials are formed only at the metal/film interface by inward migration of anions and the direct ejection of outwardly migrating cation species occurs at the film/electrolyte interface; the latter contributes to the reduced efficiency for the film formation. At the low sweep rate, the current efficiency is further reduced to 37%, but 68% of the oxidized iron was converted to the anodic film. The increased conversion efficiency during porous film growth at the low sweep rate in comparison with the barrier film growth at the high sweep rate is of interest, being related to the field-assisted dissolution process and/or the probable presence of oxygen gas bubbles in the barrier layer formed at the low sweep rate. Thus, the field-assisted dissolution was examined in detail.

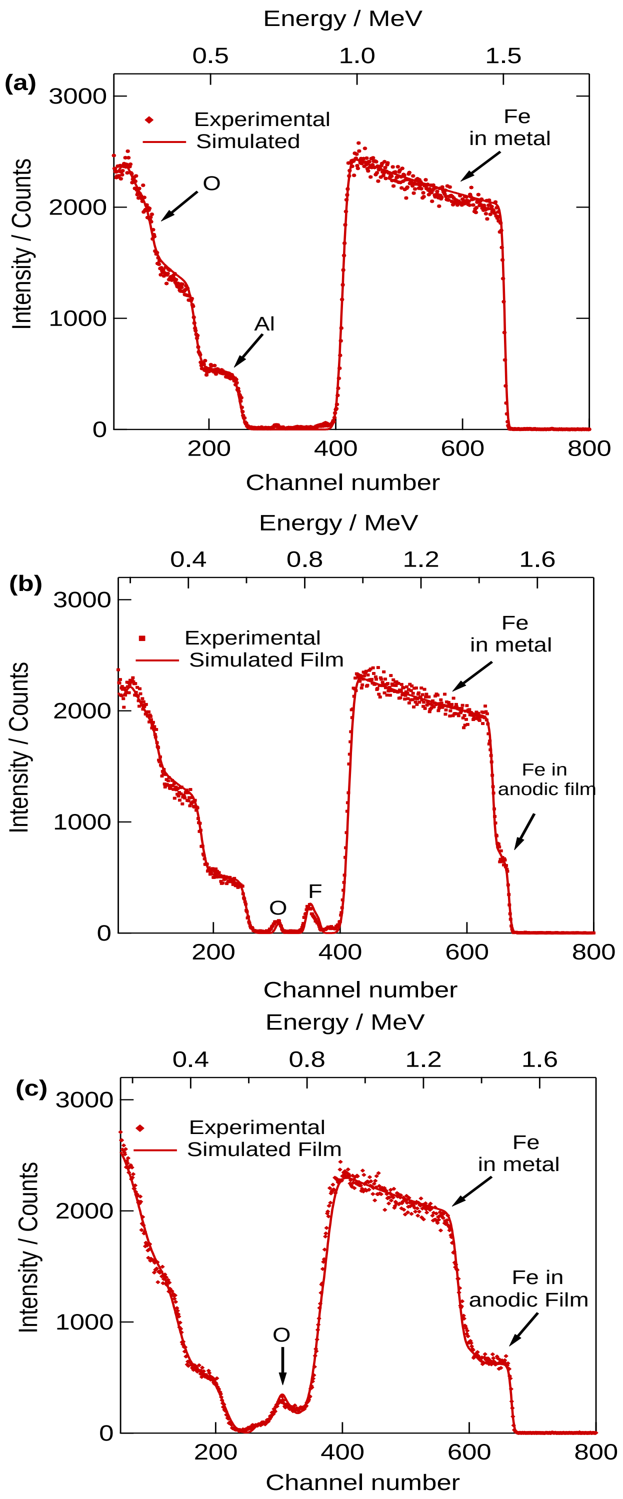

Figure 4.5 Experimental and simulated RBS spectra of magnetron-sputtered iron films (a) as-deposited and anodized to 50 V at sweep rates of (b) 1.0 and (c) 0.05 V s^{-1} in an EG electrolyte containing 0.1 mol dm^{-3} ammonium fluoride and 0.1 mol dm^{-3} H_2O at 273 K.

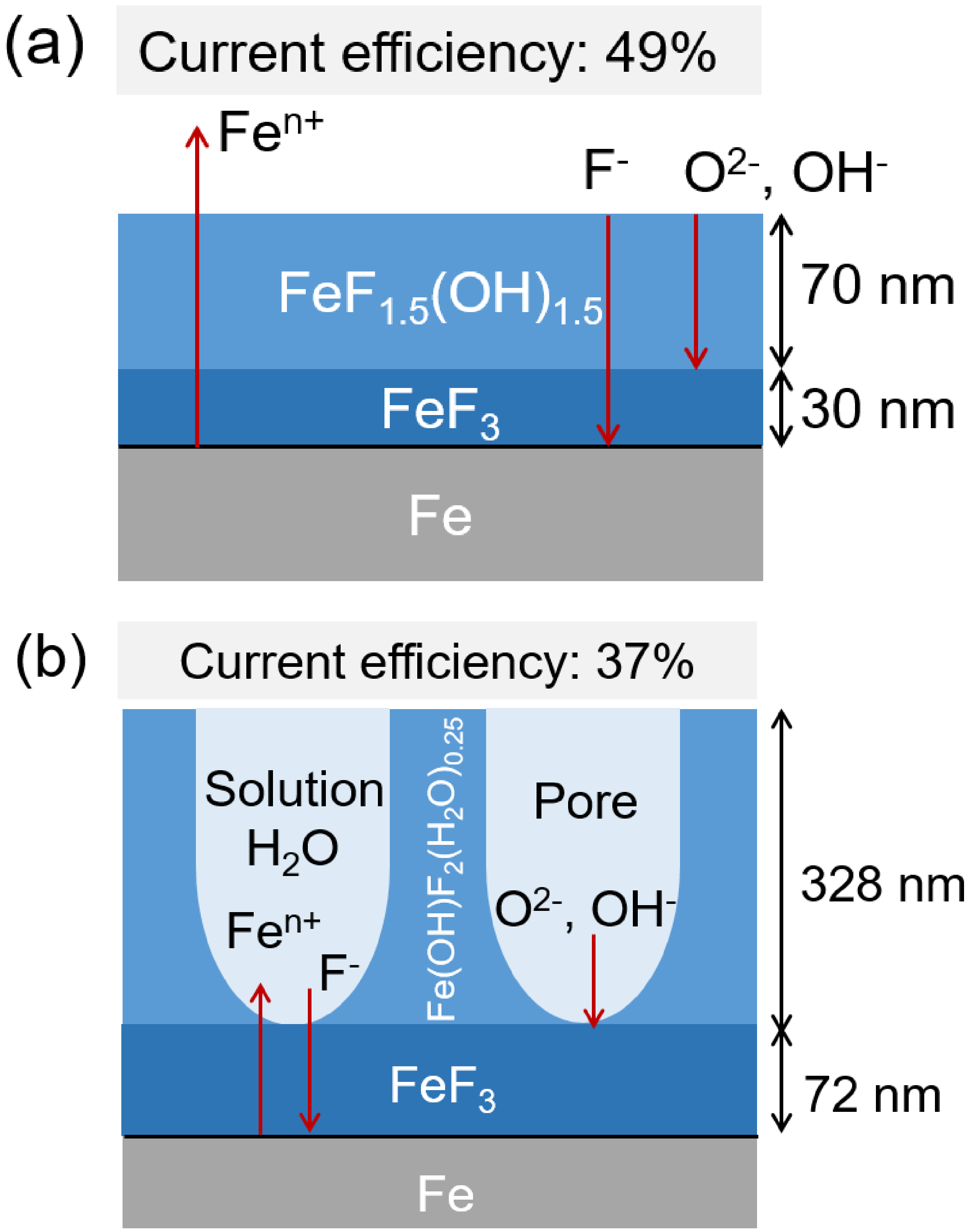

Figure 4.6 Schematic illustration of the composition and morphology of the magnetron-sputtered iron films anodized to 50 V at sweep rates of (a) 1.0 and (b) 0.05 V s^{-1} in an EG electrolyte containing 0.1 mol dm^{-3} ammonium fluoride and 0.1 mol dm^{-3} H_2O at 273 K.

Table 4.1 Results of RBS analysis for the magnetron-sputtered iron films as-deposited and anodized to 50 V at 1.0 and 0.05 V s^{-1} in EG electrolyte containing 0.1 mol dm^{-3} ammonium fluoride and 0.1 mol dm^{-3} H_2O at 273 K.

Sweep rate (V s^{-1})	Layer	Composition	Thickness (nm)	Density (g cm^{-3})
1.0	Outer layer	$FeF_{1.5}(OH)_{1.5}$	70	2.3
	Inner layer	FeF_3	30	3.3
	Fe	Fe	418	
0.05	Porous layer	$Fe(OH)F_2(H_2O)_{0.25}$	328	2.1
	Inner barrier layer	FeF_3	72	3.3
	Fe	Fe	390	

*fast Fe: 458 nm, slow: 465 nm.

Table 4.2 Electric charges for iron oxidation and film formation estimated from the RBS analysis, as well as that passed during anodizing to 50 V and the current efficiency for film formation.

Sweep rate (V s^{-1})	Fe consumed		Charge for film formation (C cm^{-2})	Charge passed (C cm^{-2})*	Current efficiency (%)
	Thickness (nm)	Charge (C cm^{-2})*			
1.0	40	0.16	0.073	0.15	49
0.05	75	0.31	0.21	0.57	37

*Assuming the oxidation to Fe (III).

4.2.4 Field-assisted dissolution

In order to examine the influence of electric field on the dissolution of anodic films formed on iron, a barrier-type film of 100 nm thickness was first formed by anodizing of the magnetron-sputtered iron film to 50 V at the high sweep rate of 1.0 V s^{-1}. Then, several constant voltages were applied to the anodized specimen and examined the change in the film thickness. **Fig. 4.7** shows the change in the current density during re-anodizing the iron specimen, covered with the 100 nm-thick anodic film, at 10, 15, 20 and 30 V. At 10 V the current density is initially very low, since the pre-formed anodic film was developed to 50 V and initial field strength is too low for ion migration. However, the current density gradually increases with time. The initial very low current is also found at 15 V, but the current increase occurs from the commencement of re-anodizing when 20 and 30V are applied.

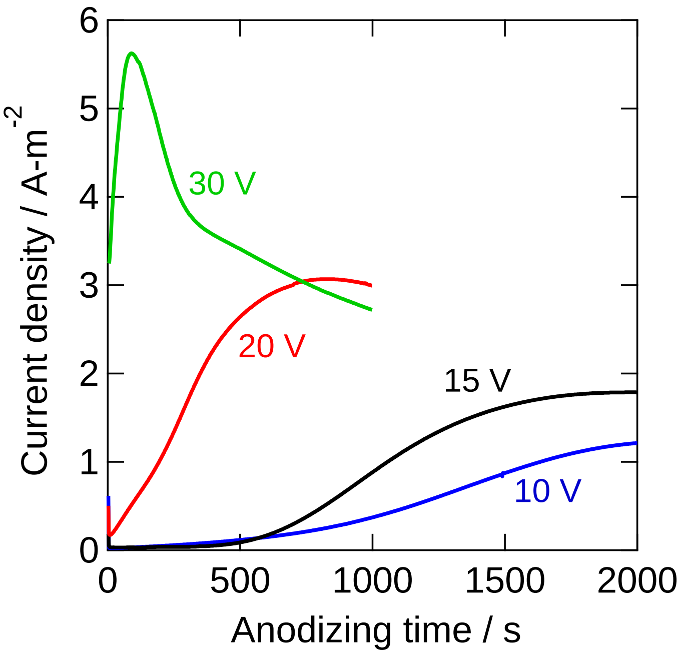

Figure 4.7 Current transients of magnetron-sputtered iron films with a pre-formed 100-nm-thick, barrier-type anodic film during re-anodizing at several constant voltages in an EG electrolyte containing 0.1 mol dm^{-3} ammonium fluoride and 0.1 mol dm^{-3} H_2O at 273 K.

Fig. 4.8 shows the scanning electron micrographs of cross-sections before and after re-anodizing at several voltages for 1000 s. It is obvious that the anodic film of approximately 100 nm thickness (**Fig. 4.8a**) shows thickness reduction to 76 nm uniformly after re-anodizing at 10 V for 1000 s (**Fig. 4.8b**). Further reduced the thickness of 67 nm is observed at 15 V (**Fig. 4.8c**), indicating that the electric field-assisted dissolution occurs. During re-anodizing at these voltages the morphology of the anodic films does not change; no porous film is developed. In contrast, thickening of the anodic film takes place at 20 V (**Fig. 4.8d**). Although the pores are not clearly seen in the anodic film at the available resolution of SEM, a porous film must be grown for film thickening at 20 V. Thickening of the porous film was clearly observed after re-anodizing at 30 V (**Fig. 4.8e**).

The change in the thickness of the anodic film during immersion and re-anodizing at 10 and 15 V (**Fig. 3.9a**) shows the accelerated dissolution under applying an electric field. During immersion of the pre-anodized specimen, film thinning occurs at a rate of 0.47 nm min^{-1}. The dissolution rate is enhanced by applying 10 and 15 V with the latter voltage resulting in the more enhanced dissolution rate. Since the thickness reduction occurs during re-anodizing, the electric field across the barrier layer changes with re-anodizing. The change in the electric field with re-anodizing time is depicted in **Fig. 4.9b**. Since the field-assisted dissolution is found at 10 V and re-anodizing time of 600 s, the electric field of 1.2 MV cm^{-1} appears to be sufficient to enhance the dissolution of the anodic film on iron. This electric field is much lower than that for anodic alumina (5.5 MV cm^{-1}), examined by Oh and Thompson [9]. Oh and Thompson also reported the presence of a critical field (7.46 MV cm^{-1}) for pore initiation due to field-induced instability. In the anodic film on iron, the critical field must be higher than 2.8 MV cm^{-1} since no pores were still found when the electric field was increased to this value at 15 V (**Fig. 4.9b**). In summary, in anodizing of iron in the fluoride-containing EG electrolyte, the electric field has a crucial role in dissolution and the morphology of the anodic films, as in anodizing of aluminum in acid electrolytes. Major pores formed by the mechanical instability, found in anodizing of

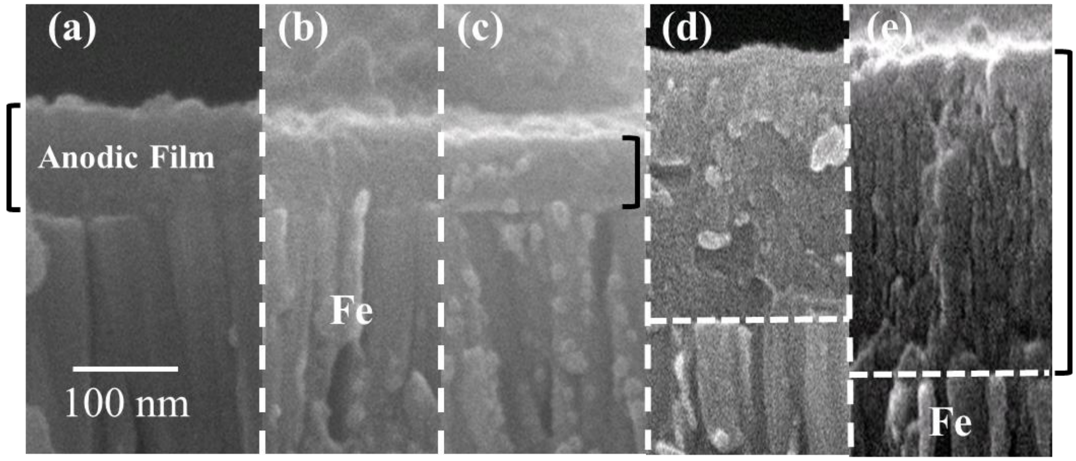

Figure 4.8 Scanning electron micrographs of cross-sections of magnetron-sputtered iron films with a pre-formed 100-nm-thick, barrier-type anodic film (a) before anodizing, and after re-anodizing at (b) 10 V, (c) 15 V, (d) 20 V, and (e) 30 V for 1000 s in an EG electrolyte containing 0.1 mol dm^{-3} ammonium fluoride and 0.1 mol dm^{-3} H_2O at 273 K.

aluminum, were not formed under the present anodizing condition for iron. Thus, pores formed due to field-assisted dissolution appear to be dominant in anodizing of iron.

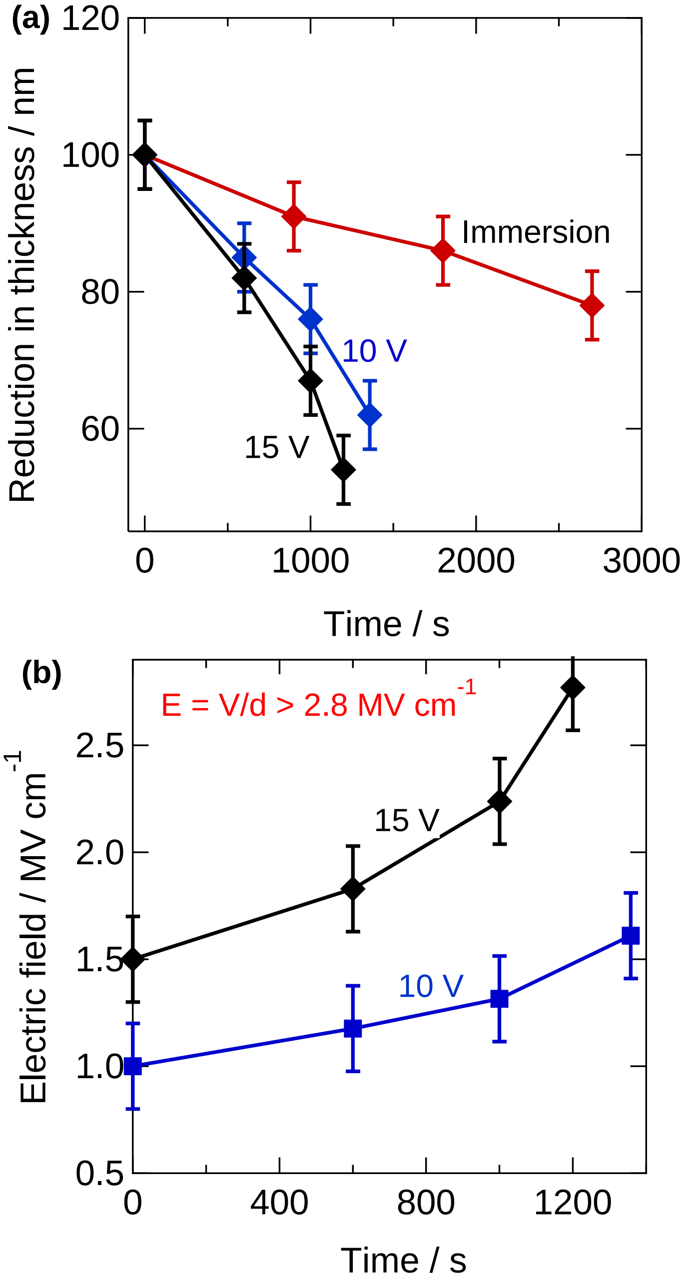

Figure 4.9 (a) Change in thickness of the pre-formed 100-nm-thick anodic films during immersion and re-anodizing at 10 and 15 V in an EG electrolyte containing 0.1 mol dm^{-3} ammonium fluoride and 0.1 mol dm^{-3} H_2O at 273 K and (b) Respective change in the electric field associated with the thinning of the anodic films.

4.3 Conclusions

1. The anodic films are formed on magnetron-sputtered iron films by anodizing potentiodynamically to 50 V at two different sweep rates of 1.0 and 0.05 V s^{-1} in EG electrolyte containing 0.1 mol dm^{-3} ammonium fluoride and 0.1 mol dm^{-3} H_2O at 273K.
2. The film morphology is dependent upon the sweep rate; a barrier-type at the high sweep rate and nanoporous-type at the low sweep rate. The barrier-type film is formed even at a low current efficiency of 49%, suggesting no film material developing at the film/electrolyte interface. In contrast, the nanoporous anodic film is developed by anodizing to the same 50 V at the low sweep rate of 0.05 V s^{-1}. The pores are developed preferentially along with troughs in the surface, which corresponds to the boundaries of columnar morphology. The anodic films consist compositionally of an outer iron (III) hydroxyfluoride layer and an inner FeF_3 layer, with the latter layer forming as a consequence of the faster migration of fluoride ions in comparison with oxygen species.
3. When an electric field is applied to the barrier-type anodic film formed to 50 V at the high sweep rate, chemical dissolution at the film/electrolyte interface is accelerated. The field-assisted dissolution is also of importance in anodizing of iron to form nanoporous anodic films.

References:

[1] C. Blawert, W. Dietzel, E. Ghali, G.L. Song, *Adv. Eng. Mater.*, **8**, 511 (2006).

[2] H. Masuda, K. Fukuda, *Science*, **268**, 1466 (1995).

[3] T. Kyotani, L.-f. Tsai, A. Tomita, *Chem. Mater.*, **7**, 1427 (1995).

[4] P. Roy, S. Berger, P. Schmuki, *Angew. Chem., Int. Ed.*, **50**, 2904 (2011).

[5] L. Young, D.J. Smith, *J. Electrochem.Soc.*, **126**, 765 (1979).

[6] G. E. Thompson, *Thin Solid Films*, **297**, 192 (1997).

[7] S. J. Garcia-Vergara, L. Iglesias-Rubianes, C.E. Blanco-Pinzon, P. Skeldon, G.E. Thompson, P. Campestrini, *Proc. R. Soc. A: Mathematical, Physical and Engineering Sciences*, **462**, 2345 (2006).

[8] J. E. Houser, K.R. Hebert, *Nat. Mater.*, **8**, 415 (2009).

[9] J. Oh, C.V. Thompson, *Electrochim. Acta*, **56**, 4044 (2011).

[10] K. R. Hebert, S.P. Albu, I. Paramasivam, P. Schmuki, *Nat. Mater.*, **11**, 162 (2012).

[11] G. E. Thompson, R.C. Furneaux, G.C. Wood, J.A. Richardson, J.S. Goode, *Nature*, **272**, 433 (1978).

[12] S. J. Garcia-Vergara, P. Skeldon, G.E. Thompson, H. Habazaki, *Electrochim. Acta*, **52**, 681 (2006).

[13] T. P. Hoar, N.F. Mott, *J. Phys. Chem. Solids*, **9**, 97 (1959).

[14] J. P. O'Sullivan, G.C. Wood, *Proc. R. Soc. Lond.*, **A317**, 511 (1970).

[15] F. Zhou, A. Baron-Wiecheć, S.J. Garcia-Vergara, M. Curioni, H. Habazaki, P. Skeldon, G.E. Thompson, *Electrochim. Acta*, **59**, 186 (2012).

[16] F. Zhou, A.K.M. Al-Zenati, A. Baron-Wiechec, M. Curioni, S.J. Garcia-Vergara, H. Habazaki, P. Skeldon, G.E. Thompson, *J. Electrochem. Soc.*, **158**, C202 (2011).

[17] S. J. Garcia-Vergara, D. Le Clere, T. Hashimoto, H. Habazaki, R. Skeldon, G.E. Thompson, *Electrochim. Acta*, **54**, 6403 (2009).

[18] S. J. Garcia-Vergara, P. Skeldon, G.E. Thompson, H. Habazaki, *Thin Solid Films*, **515**, 5418 (2007).

[19] J. E. Houser, K.R. Hebert, *Phys. Status Solidi A*, **205**, 2396 (2008).

[20] J. M. Macak, P. Schmuki, *Electrochem. Acta*, **52**, 1258 (2006).

[21] S. Berger, J. Faltenbacher, S. Bauer, P. Schmuki, *Physica Status Solidi-Rapid Res. Lett.*, **2**, 102 (2008).

[22] W. Wei, K. Lee, S. Shaw, P. Schmuki, *Chem. Commun.*, **48**, 4244 (2012).

[23] A. Jagminas, K. Mazeika, N. Bernotas, V. Klimas, A. Selskis, D. Baltrunas, *Appl. Surf. Sci.*, **257**, 3893 (2011).

[24] A. Jagminas, V. Klimas, K. Mazeika, N. Bernotas, A. Selskis, G. Niaura, *Electrochim. Acta*, **56**, 5452 (2011).

[25] H. Habazaki, Y. Konno, Y. Aoki, P. Skeldon, G.E. Thompson, *J. Phys. Chem. C*, **114**, 18853 (2010).

[26] S. P. Albu, A. Ghicov, P. Schmuki, *Physica Status Solidi-Rapid Res. Lett.*, **3**, 64 (2009).

[27] H. E. Prakasam, O.K. Varghese, M. Paulose, G.K. Mor, C.A. Grimes, *Nanotechnol.*, **17**, 4285 (2006).

[28] S. K. Mohapatra, S.E. John, S. Banerjee, M. Misra, *Chem. Mater.*, **21**, 3048 (2009).

[29] R. R. Rangaraju, A. Panday, K.S. Raja, M. Misra, *J. Phys. D: Appl. Phys.*, **42**, 135303 (2009).

[30] Z. H. Zhang, M.F. Hossain, T. Takahashi, *Appl. Cat. B-Env.*, **95**, 423 (2010).

[31] K. Y. Xie, J. Li, Y.Q. Lai, W. Lu, Z.A. Zhang, Y.X. Liu, L.M. Zhou, H.T. Huang, *Electrochem. Commun.*, **13**, 657 (2011).

[32] H. Cheng, Z. G. Lu, R.G. Ma, Y.C. Dong, H.E. Wang, L. J. Xi, L. X. Zheng, C. K. Tsang, H. Li, C. Y. Chung, J.A. Zapien, Y.Y. Li, *J. Mater. Chem.*, **22**, 22692 (2012).

[33] M. M. Lohrengel, *Mater. Sci. Eng. R-Rep.*, **11**, 243 (1993).

[34] M. Curioni, P. Skeldon, G.E. Thompson, *J. Electrochem. Soc.*, **156**, C407 (2009).

[35] S. J. Garcia-Vergara, P. Skeldon, G.E. Thompson, H. Habakaki, *Corros. Sci.*, **49**, 3696 (2007).

[36] Y. Konno, S. Yang, E. Tsuji, Y. Aoki, P. Skeldon, G.E. Thompson, H. Habazaki, *ECS Trans.*, **50**, 183 (2013).

[37] M. Curioni, T. Gionfini, A. Vicenzo, P. Skeldon, G.E. Thompson, *Surf. Interface Anal.*, **45**, 1485 (2013).

[38] K. Shimizu, K. Kobayashi, G.E. Thompson, P. Skeldon, G.C. Wood, *J. Electrochem. Soc.*, **144**, 418 (1997).

[39] H. Habazaki, K. Fushimi, K. Shimizu, P. Skeldon, G.E. Thompson, *Electrochem. Commun.*, **9**, 1222 (2007).

Chapter 5

Growth of barrier-type anodic film on magnesium in EG-water mixed electrolytes containing fluoride and phosphate

5.1 Introduction

Magnesium is the eighth most abundant element on the earth and has huge worldwide resources, especially in the ocean. Therefore, magnesium and its alloys have attracted growing interest in the recent years as structural materials in aerospace, electronics, and automotive industries owing to their low density, good thermal conductivity, and high strength/weight ratios, and are considered as alternatives to aluminum alloys. Magnesium is also promising as an anode material in non-rechargeable batteries because of its negative potential and high energy density in aqueous electrolytes. Likewise, magnesium/non-aqueous batteries are believed to be an alternative to the lithium-ion batteries because of their low cost, high energy density, and recyclability. The major challenge for the development of magnesium-based batteries is the passivity of the magnesium anode. Magnesium alloys are more important than high purity magnesium for technological applications, such as for aerospace and military purposes and very high strength and creep-resistant magnesium alloys are critical for above-mentioned applications. Likewise, electronic industry is an emerging market for magnesium alloys. These applications generally demand high corrosion resistance. Unfortunately, magnesium and its alloys have low corrosion resistance in aqueous electrolytes, which limits their wide range of applications as mentioned in chapter 1 [1, 2].

It is now well known that low corrosion-resistant magnesium alloys need surface treatments or coating in many applications and variety of surface treatments are being used to protect magnesium and its alloys from corrosion. These surface treatments include galvanizing/plating (Cu, Ni, Cr, Zn), anodizing (HAE, Dow 17, Keronite, Tagnite etc.), and surface conversion coatings such as chromating and phosphating. Among these processes, anodizing appears to be the most efficient technique for corrosion protection of magnesium alloys. Most anodizing treatments produce relatively thick porous films under conditions of dielectric breakdown [3-5]. Films formed under the absence of dielectric breakdown have also been investigated in aqueous and non-aqueous electrolytes. A variety of aqueous electrolytes have been utilized to form anodic films on magnesium and its alloys and the films formed on magnesium have been reported to consist of MgF_2, MgO and/or $Mg(OH)_2$ [6-8]. However, only a few reports are available on the understanding of growth behavior of anodic films on magnesium in aqueous electrolytes. This may be due to irregular porous structure produced during anodizing.

Because of the difficulty of film formation in aqueous electrolytes at high Faradaic efficiency, fluoride-containing organic electrolytes have been utilized recently to form the anodic films at high efficiency on iron, magnesium, titanium, zirconium, and niobium [9-13]. Therefore, understanding the behavior of metals in organic electrolytes is also important because organic electrolytes are widely used in lithium-ion batteries and electric double layer capacitors. However, only a few studies have been conducted on anodizing magnesium in organic electrolytes [13, 14]. Organic species were also incorporated into the anodic films, and their incorporation was enhanced by reducing the water concentration.

By utilizing organic electrolytes containing fluoride, it was also reported recently that the growth of barrier-type anodic films proceeded at high current efficiency in fluoride-containing glycerol or ethylene glycol electrolytes [15, 16]. In particular, the growth efficiency of the anodic films formed on magnetron-sputtered magnesium in the fluoride/EG was close to 100%. The films contained crystalline MgF_2 phase and the Pilling-Bedworth ratio (PBR) in this film growth is greater than unity, probably contributing to the uniform and efficient film growth, in addition to the high chemical stability of MgF_2. The formation of uniform anodic films on magnesium provides an opportunity of systematic and detailed studies on the growth of anodic films on magnesium and its alloys. Influence of phosphate addition into the fluoride/EG electrolytes on the growth, structure and composition of the anodic films was also investigated [17].

The incorporation of phosphate changed the film structure from crystalline to amorphous. In addition, much thicker anodic films were formed at the same formation voltage in the phosphate-containing electrolyte, indicating the increase of the PBR value by phosphate incorporation. In the fluoride/EG electrolytes, the growth efficiency is reduced by the addition of water above 50% and film breakdown occurs at low voltages. The difficulty of the formation of uniform anodic films on magnesium in aqueous electrolytes has often been explained in terms of the PBR value (~ 0.80) of MgO/Mg less than unity [18, 19]. It is therefore probable that the incorporation of phosphate into the anodic films on magnesium promotes the uniform growth of anodic films even in aqueous electrolytes by enlarging the PBR value. In the present study, the growth behavior of anodic films on magnesium EG-H_2O electrolytes containing either fluoride or both fluoride and phosphate was examined. Particular attention was paid to the influence of the concentration of H_2O and the addition of phosphate in electrolyte on the growth efficiency and uniformity of the anodic films. Since the incorporation of phosphate, which increases the PBR, may influence the growth efficiency at high water concentrations.

5.2 Results

5.2.1 Voltage-time response in phosphate-containing electrolytes

Fig. 5.1 shows the voltage-time curves of the magnetron-sputtered magnesium films of ~220 nm thickness during anodizing in the EG-H_2O electrolytes containing 0.1 mol dm^{-3} ammonium fluoride and 0.1 mol dm^{-3} potassium dihydrogen phosphate at a constant current density of 10 A m^{-2}. The anodizing voltage increases linearly (~ 0.76 V s^{-1}) to more than 200 V up to 30 vol. % H_2O. The voltage rises steeply above 200V, because of the complete consumption of magnetron-sputtered magnesium films of ~220 nm thickness. The rate of the voltage rise to 200 V is 0.76 V s^{-1} and independent of the H_2O concentration up to 30 vol. % H_2O. The results are very similar to the previous study of magnesium films in phosphate-free EG electrolytes, where film growth proceeds close to 100 % efficiency up to 50 vol. % H_2O at a rate of 0.96-1.0 V s^{-1} [17]. Further increase in the H_2O concentration gradually reduces the rate of voltage rise. In addition, the linear voltage rise is terminated below 200 V because of dielectric breakdown accompanying visible sparking and voltage fluctuation. The breakdown voltage also decreases with the H_2O concentration and reaches 120 V in the aqueous electrolyte.

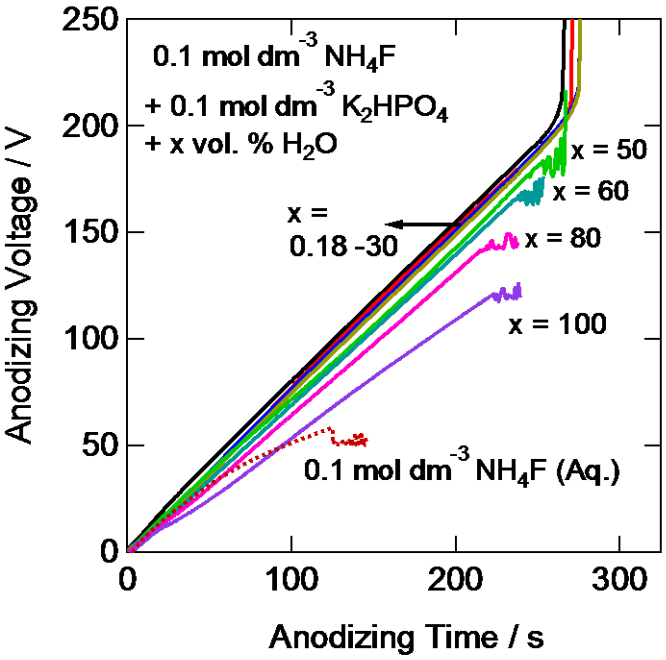

Figure 5.1 Voltage-time responses of the magnetron-sputtered magnesium films during anodizing at a current density of 10 A m^{-2} in the EG-H_2O electrolytes containing 0.1 mol dm^{-3} ammonium fluoride, 0.1 mol dm^{-3} dipotassium hydrogen phosphate and x vol. % H_2O and an aqueous electrolyte containing 0.1 mol dm^{-3} ammonium fluoride at 293 K.

In **Fig. 5.1** the voltage-time curve of the magnesium film during anodizing in the phosphate-free aqueous electrolyte containing 0.1 mol dm^{-3} fluoride is also included. It is obvious that the linear voltage rise continues to a higher voltage in the phosphate-containing aqueous electrolyte in comparison with the phosphate-free counterpart. In addition, the dielectric breakdown voltage in the phosphate-containing electrolyte (120 V) is much higher than that in the phosphate-free electrolyte (55 V). Thus, it is likely that the addition of phosphate in the electrolyte promotes the growth of uniform anodic films on magnesium to higher voltages.

Fig. 5.2 shows the change in the slope of the voltage rise with the H_2O concentration in the electrolyte. The slopes obtained in the phosphate-free EG-H_2O electrolytes with the same fluoride concentration are also included in this figure. The slopes are always lower in the phosphate-containing electrolytes (~ 0.76 V s^{-1}) in comparison with those in the phosphate-free counterparts (1–0.96 V s^{-1}) [17]. The reduction of the slope suggests that the anodic films formed in the phosphate-containing electrolytes are thicker than those in the phosphate-free electrolytes. The slope decreases gradually with an increase in water concentration above 30 vol. % H_2O in the phosphate-containing electrolytes, whereas the significant reduction of slope occurs above 50 vol. % H_2O in the phosphate-free electrolytes. The reduced slope at high H_2O concentrations is associated with a decrease in current efficiency for film growth as discussed later.

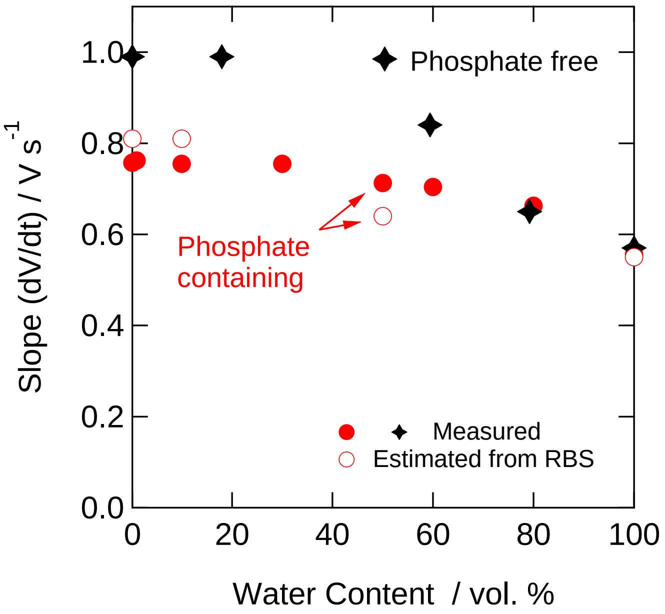

Figure 5.2 Slopes of linear voltage rise as a function of water concentration in the electrolyte for the magnetron-sputtered magnesium films during anodizing at a constant current density of 10 A m^{-2} in the EG-H_2O electrolytes containing 0.1 mol dm^{-3} ammonium fluoride with and without 0.1 mol dm^{-3} dipotassium hydrogen phosphate at 293 K.

Fig. 5.3 shows the change in the voltage of dielectric breakdown with the logarithm of electrolyte conductivity. There is a good linear correlation between the breakdown voltage and the logarithm of the conductivity in the phosphate-containing electrolytes containing 50 vol. % and higher H_2O concentrations. This linear correlation is well-known in anodizing of valve metals in aqueous electrolytes. There was another report that the breakdown voltage was controlled by the anion concentration in the aqueous electrolytes [20]. However, in the present study, the anion concentration remains unchanged and only H_2O concentration was changed. Thus, it is unlikely that the anion concentration is a critical factor in controlling the dielectric breakdown in the present EG-H_2O mixed electrolytes. The breakdown voltage in the phosphate-free electrolyte, also shown in this figure, is located far below the linear correlation for the phosphate-containing electrolytes. The low breakdown voltage in the phosphate-free aqueous electrolyte is, therefore, not due to the electrolyte conductivity. The presence of phosphate in electrolyte or phosphate incorporation in the anodic film may have a positive influence in an increase in the breakdown voltage.

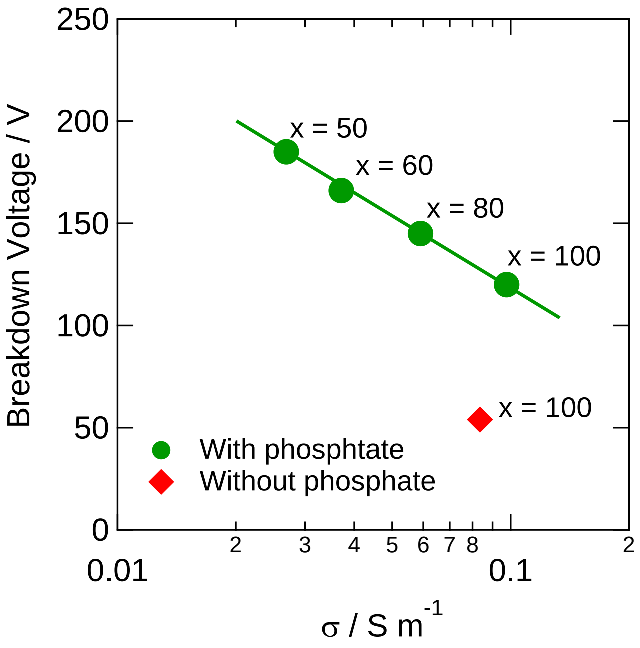

Figure 5.3 Change in the breakdown potential with the electrolyte conductivity for the magnetron-sputtered magnesium films during anodizing at a current density of 10 A m^{-2} in the EG-H_2O electrolytes containing 0.1 mol dm^{-3} ammonium fluoride, 0.1 mol dm^{-3} dipotassium hydrogen phosphate and x vol. % H_2O at 293 K.

5.2.2 Film morphology

Fig. 5.4 shows the scanning electron micrographs of the surfaces of the sputter-deposited magnesium films as-deposited and anodized to 100 V in the EG-H_2O electrolytes containing 0.1 mol dm^{-3} NH_4F and 0.1 mol dm^{-3} K_2HPO_4 at 293K. The hexagonal shaped grains are evident in the micrograph of the as-deposited magnesium (**Fig. 5.4a**), suggesting that the deposited hcp magnesium film has (0001) preferred orientation. When the magnesium films were anodized to 100 V in the electrolytes at various H_2O concentrations, the surfaces become smooth and featureless (**Figs. 5.4b-e**), even in the aqueous electrolyte (**Fig 5.4e**). This indicates the homogeneous formation of the anodic film in the phosphate-containing EG-H_2O electrolytes. The formation of uniform anodic films in phosphate-containing electrolytes is in contrast to the film formed in the phosphate-free aqueous electrolyte, in which the surface of the anodic film is relatively rough even below the dielectric breakdown voltage (**Fig. 5.4f**).

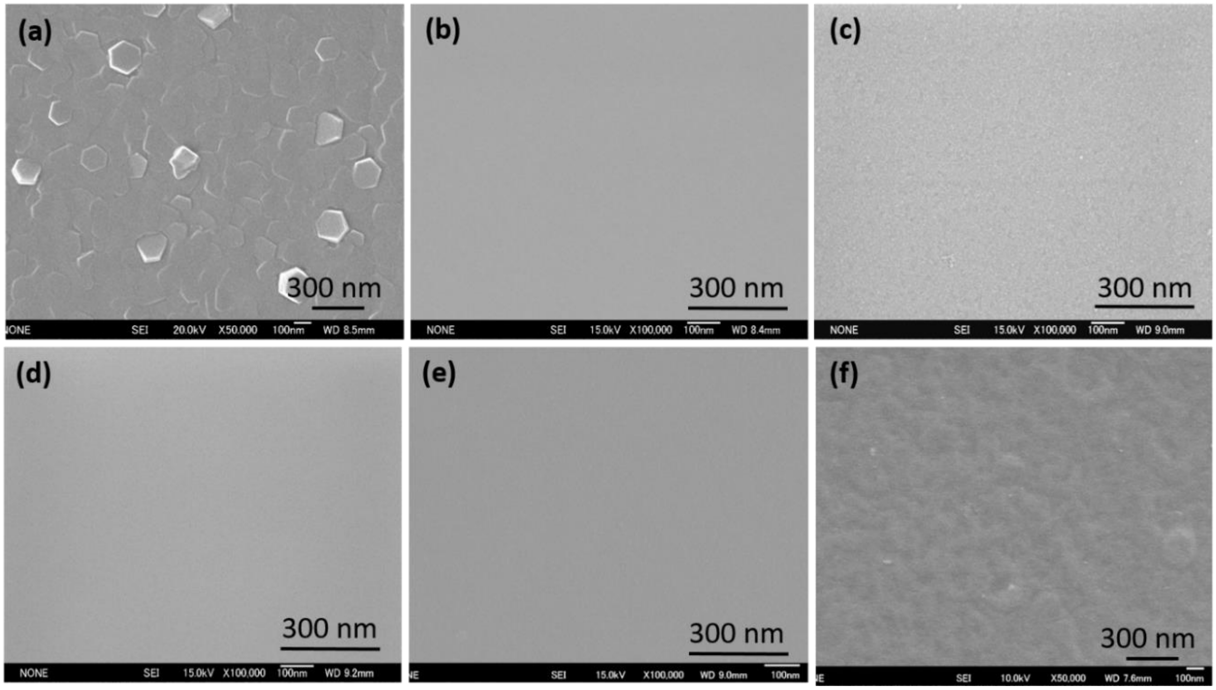

Figure 5.4 Scanning electron micrographs of surfaces of the magnetron-sputtered magnesium films (a) as-deposited and anodized to 100 V at 10 A m^{-2} in the EG-H_2O electrolytes containing 0.1 mol dm^{-3} ammonium fluoride, 0.1 mol dm^{-3} dipotassium hydrogen phosphate and (b) 0.18 vol. % H_2O (c) 10 vol. % H_2O (d) 50 vol. % H_2O and (e) 100 vol.% H_2O and (f) to 50 V in phosphate-free aqueous electrolyte containing 0.1 mol dm^{-3} ammonium fluoride at 293 K.

5.2.3 Structure of anodic films

The structure of anodic films formed in EG-H_2O mixed electrolytes containing 0.1 mol dm^{-3} ammonium fluoride and 0.1 mol dm^{-3} potassium dihydrogen phosphate was examined by XRD

(**Fig. 5.5**). In the previous study, it is reported that anodic film contains crystalline MgF_2 phase, regardless of water concentration in the electrolyte in phosphate free electrolytes [17]. However, the XRD patterns of the anodized specimens in EG-H_2O mixed electrolytes containing fluoride and phosphate, reveal only the reflections from the hcp magnesium film and the fcc aluminum substrate; the anodic films formed in the present electrolytes containing phosphate appear to be amorphous. The present study indicates that the structure of the anodic films on magnesium is always amorphous in the phosphate-containing EG-H_2O electrolytes, regardless of H_2O concentration (**Fig. 5.5**).

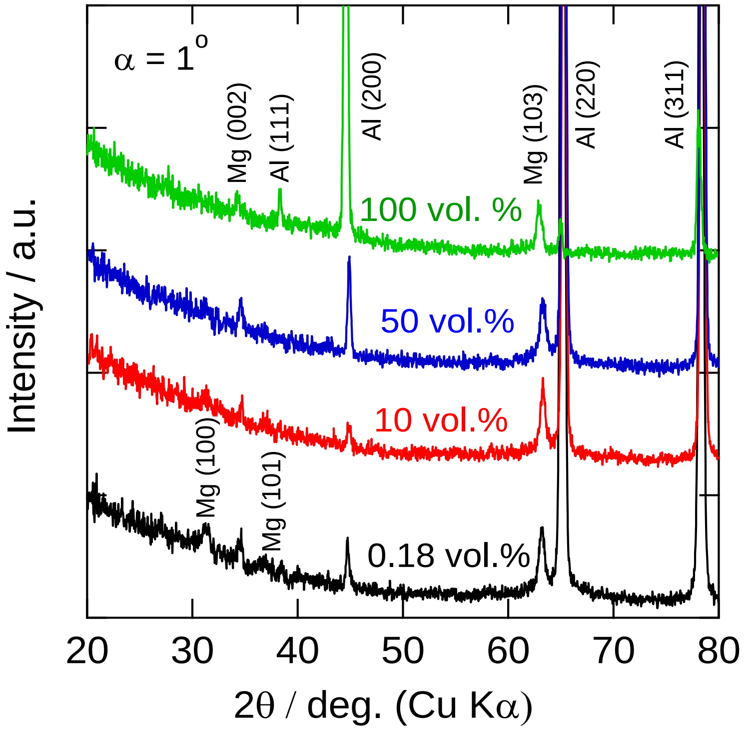

Figure 5.5 XRD patterns of the magnetron-sputtered magnesium films anodized to 100 V at 10 A m^{-2} in the EG-H_2O mixed electrolytes containing 0.1 mol dm^{-3} ammonium fluoride, 0.1 mol dm^{-3} dipotassium hydrogen phosphate at 293 K.

5.2.4 Film thickness

The anodic films formed on magnesium were further examined by transmission electron microscopy. Habazaki and co-workers recently investigated the formation of barrier-type films with flat and parallel metal/film and film/electrolyte interfaces in phosphate containing and phosphate free electrolytes at 0.1 mol dm^{-3} H_2O. They found that formation ratio was changed from 1.24 nm V^{-1} to 1.8 nm V^{-1} by the addition of phosphate. Further, phosphate addition transformed film structure from crystalline to amorphous as shown in **Fig. 5.6** [15, 17]. The amorphization of the anodic film by the addition of phosphate also changes the transport number of cations from ~ 0.6 to ~ 0.72.

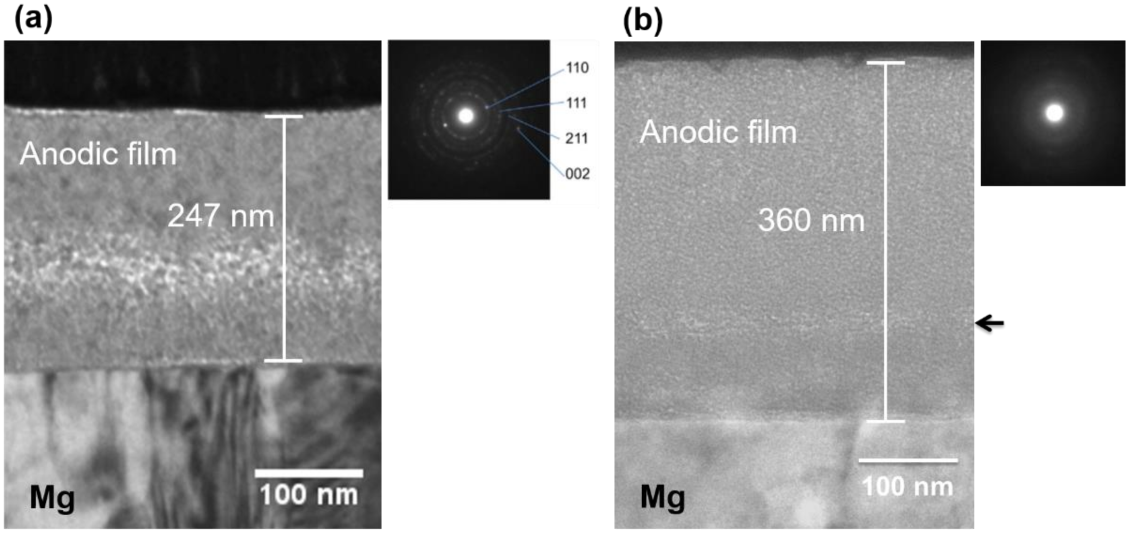

Figure 5.6 Transmission electron micrographs and selected area electron diffraction patterns of the anodic film formed on the magnetron-sputtered magnesium specimens anodized to 200 V in the EG electrolyte containing 0.1 mol dm^{-3} H_2O and (a) 0.1 mol dm^{-3} ammonium fluoride and, (b) 0.1 mol dm^{-3} ammonium fluoride and 0.1 mol dm^{-3} dipotassium hydrogen phosphate at 293 K [15, 17].

When the water concentration is increased to 50 vol. % (**Fig. 5.7a**), an anodic film of 142 nm thickness is obtained after anodizing to 100 V, corresponding to the formation ratio of 1.42 nm V^{-1}. The film thickness and formation ratio are further reduced to 113 nm and 1.13 nm V^{-1} in the aqueous electrolyte containing phosphate (**Fig. 5.7b**). The transmission electron micrographs in phosphate containing electrolytes reveal that the anodic films appear to consist of two layers. The inner part of the anodic films, approximately one-third of film thickness, shows apparently darker appearance. From later RBS analyses, the inner part contains a less amount of incorporated phosphate. The absence of diffraction contrast in the outer part of the anodic films suggests the amorphous or poorly crystalline nature, in agreement with the XRD pattern. The inner part of the anodic films showed electron-beam-induced crystallization during observation; thus, diffraction contrast appears in the inner part of the anodic films in **Figs. 5.7a and b**. The electron-beam-induced crystallization was often found in amorphous anodic alumina [21] and the crystallization was delayed by the incorporation of electrolyte anion species [22]. In the present anodic films, preferential crystallization in the inner layer at higher water concentration may also be associated with the lower concentration of phosphate in the inner layer. In agreement with SEM, the TEM cross section of the anodic film in phosphate free aqueous electrolyte (**Fig. 5.7c**) shows the non-uniform film formation. The remarkably reduced thickness of ~ 65 nm indicates that incorporation of phosphate has a significant influence on the uniform film formation in magnesium anodizing, which in turn effect the volume expansion factor as discussed later.

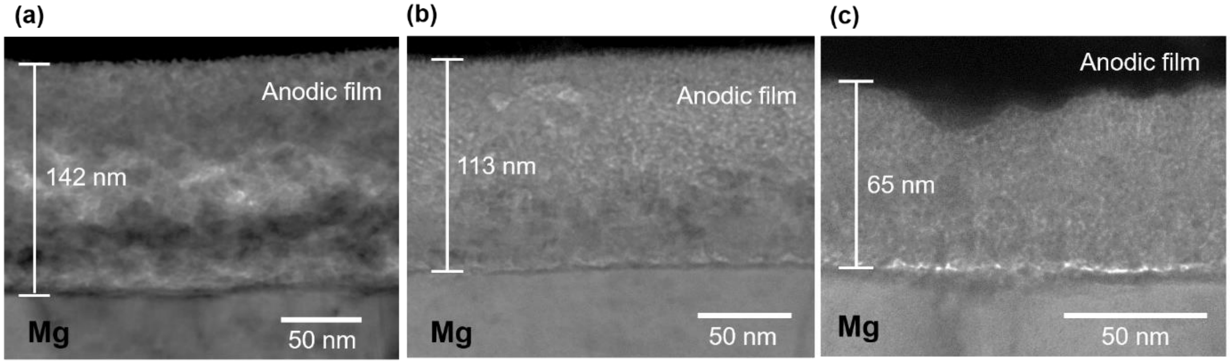

Figure 5.7 Transmission electron micrographs of FIB cross-sections of the magnetron-sputtered magnesium films anodized to 100 V at 10 A m^{-2} in the EG-H_2O electrolytes containing 0.1 mol dm^{-3} ammonium fluoride, 0.1 mol dm^{-3} dipotassium hydrogen phosphate and (a) 50 vol. % and (b) 100 vol. % H_2O and (c) to 54 V in a phosphate-free aqueous electrolyte containing 0.1 mol dm^{-3} ammonium fluoride at 293 K.

5.2.5 Film composition

Quantitative compositional analysis of anodic films formed in phosphate containing electrolytes was carried out by Rutherford backscattering spectroscopy (RBS). **Fig. 5.8a** shows the experimental and simulated RBS spectra of the magnesium films as-deposited and anodized to 100

V in the phosphate-containing EG-H_2O electrolytes. The RBS spectrum of the as-deposited magnesium shows the yield from magnesium, aluminum, and oxygen. The yields from oxygen and aluminum arise from the anodized aluminum substrate. Additional yields from phosphorus and fluorine are present in the anodized magnesium specimens, indicating the incorporation of phosphate and fluoride in the anodic films.

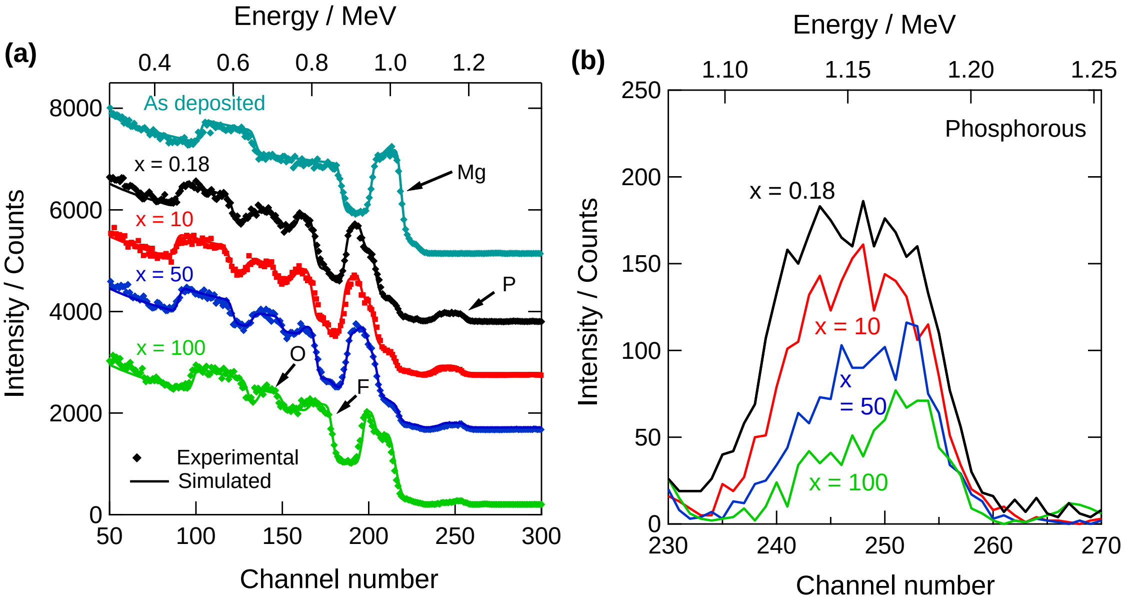

Figure 5.8 (a) Experimental and simulated RBS spectra of the magnetron-sputtered magnesium films as-deposited and anodized to 100 V at 10 A m^{-2} in the EG-H_2O electrolytes containing 0.1 mol dm^{-3} ammonium fluoride, 0.1 mol dm^{-3} dipotassium hydrogen phosphate, and x vol.% H_2O at 293 K. (b) Enlarged experimental spectra of the phosphorus yield region of (a).

The experimental RBS spectra of the anodic films at various H_2O concentrations are fitted well with the simulated spectra obtained using the composition, thickness, and density of each layer of the specimens, shown in **Table 5.1 and Fig. 5.9.** It is obvious from **Table 5.1** that the anodic films consist of phosphate-incorporated magnesium oxyfluoride at all H_2O concentrations. The hydroxide is also present in the anodic films at the H_2O concentration ≥10 vol. % in the electrolyte and the content of hydroxide increases with the H_2O concentration in the electrolyte. The fluoride concentration is similar in both the outer and inner layers, but the phosphate concentration in the inner layer is highly reduced compared with that in the outer layer. The phosphate concentration is also reduced with an increase in H_2O in the electrolyte. This fact is also evident in **Fig. 5.8b**, in which the yield from phosphorus is enlarged.

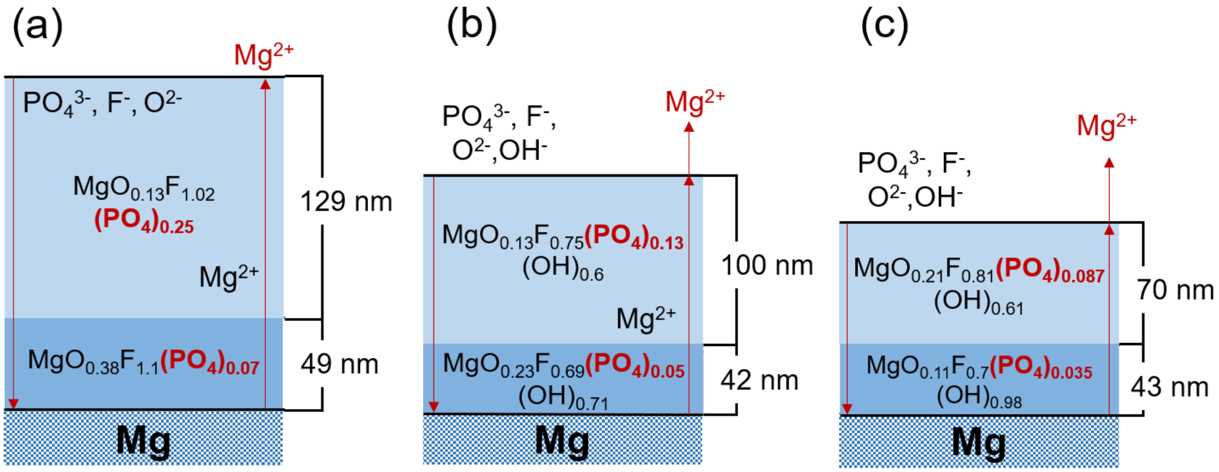

Figure 5.9 Schematic diagram elucidates the composition and thickness reduction of the outer layer by RBS simulation of the films anodized to 100 V in the EG electrolytes containing 0.1 mol dm^{-3} ammonium fluoride and 0.1 mol dm^{-3} dipotassium hydrogen phosphate and (a) 0.18 vol. H_2O (b) 50 vol. % H_2O (c) the aqueous electrolyte at 293 K.

The reduced amount of phosphate species with an increase in H_2O concentration was also examined by FTIR (**Fig. 5.10a**). Phosphate shows a characteristic peak at 1130 cm^{-1}, corresponding to a ν_3 band of PO_4^{3-}. The peak intensity decreases with an increase in H_2O concentration. From the phosphorus yield in RBS spectra (**Fig. 5.10b**), the number of phosphate ions in the anodic films was estimated and plotted as a function of H_2O concentration in the electrolyte, together with the FTIR absorbance of the phosphate peak.

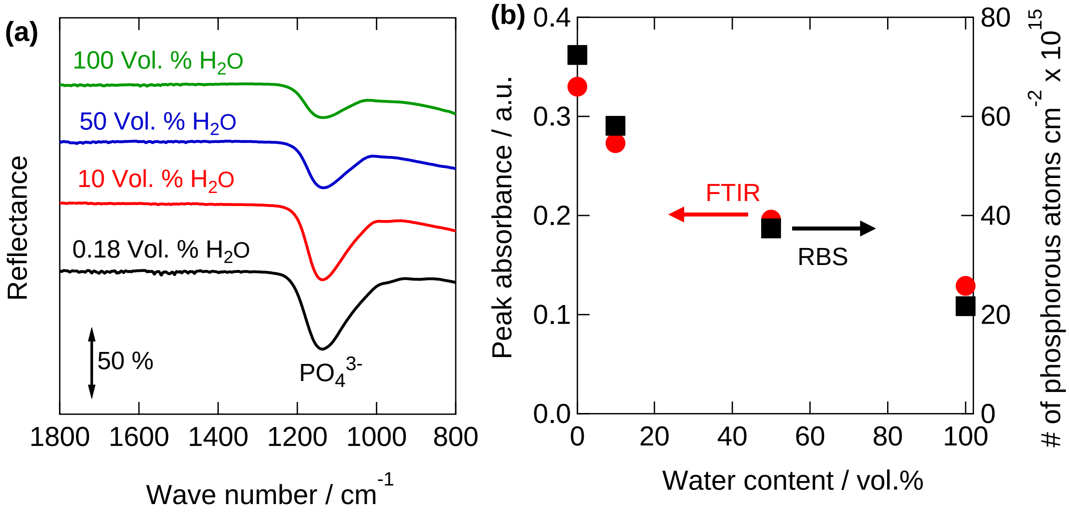

Figure 5.10 (a) FTIR spectra of the magnetron-sputtered magnesium films anodized to 100 V at 10 A m^{-2} in the EG-H_2O electrolytes containing 0.1 mol dm^{-3} ammonium fluoride, 0.1 mol dm^{-3} dipotassium hydrogen phosphate and various concentrations of H_2O and (b) Change in the peak absorbance and the number of phosphorus atoms in the anodic films with comparison of reduction in number of phosphorous atoms and peak absorption by RBS and FTIR respectively in the same electrolytes.

Table 5.1 Results of RBS analysis of the magnetron-sputtered magnesium films anodized to 100 V at a constant current density of 10 A m^{-2} in the EG-H_2O mixed electrolytes containing 0.1 mol dm^{-3} ammonium fluoride and 0.1 mol dm^{-3} dipotassium hydrogen phosphate.

H_2O concentration (vol. %)	Layers	Composition	Thickness (nm)	Density (Mg m^{-3})
0.18	Outer	$MgO_{0.13}F_{1.02}(PO_4)_{0.25}$	129	2.4
	Inner	$MgO_{0.38}F_{1.1}(PO_4)_{0.07}$	49	2.2
10	Outer	$MgO_{0.195}F_{0.837}(PO_4)_{0.195}(OH)_{0.2}$	126	2.3
	Inner	$MgO_{0.267}F_{0.8}(PO_4)_{0.044}(OH)_{0.6}$	48	2.1
50	Outer	$MgO_{0.13}F_{0.75}(PO_4)_{0.13}(OH)_{0.6}$	100	2.8
	Inner	$MgO_{0.225}F_{0.69}(PO_4)_{0.05}(OH)_{0.71}$	42	2.3
100	Outer	$MgO_{0.21}F_{0.81}(PO_4)_{0.087}(OH)_{0.61}$	70	3.1
	Inner	$MgO_{0.11}F_{0.7}(PO_4)_{0.035}(OH)_{0.98}$	43	2.2

Table 5.2 Comparison of electric charge passed during anodizing, that estimated from the magnesium thickness consumed by anodizing to 100 V in the EG-H_2O mixed electrolytes containing 0.1 mol dm^{-3} ammonium fluoride and 0.1 mol dm^{-3} dipotassium hydrogen phosphate at 293 K and the cations charge within the anodic films. The current efficiency estimated from RBS is also shown.

H_2O concentration (vol. %)	Electric charge passed during anodizing (C cm^{-2})	Mg consumed		Cations charge within film (C cm^{-2})	Current efficiency (%)
		Thickness (nm)	Charge estimated from thickness consumed (C cm^{-2})		
0.18	0.122	90	0.125	0.122	100
10	0.123	90	0.125	0.122	99.2
50	0.155	111	0.154	0.116	74.8
100	0.175	130	0.179	0.091	52.0

Table 5.3 Thicknesses of the anodic films formed and the magnesium films consumed and the volume expansion factors obtained after anodizing of the magnetron-sputtered magnesium films anodized to 100 V at a constant current density of 10 A m^{-2} in the EG-H_2O mixed electrolytes containing 0.1 mol dm^{-3} ammonium fluoride and 0.1 mol dm^{-3} dipotassium hydrogen phosphate.

H_2O concentration (vol. %)	Thickness of anodic film (nm)	Thickness of magnesium consumed (nm)	Volume expansion factor	Transport number of cations
0.18	178	90	1.98	0.73
10	174	90	1.93	0.74
50	142	111	1.28	0.78
100	113	130	0.87	0.80
100*	65	102	0.64	-

*The result in phosphate-free electrolyte (55 V).

5.2.6 Electrochemical impedance spectroscopy

Figs. 5.11 and 5.12 show the Bode plots of the magnesium films anodized in the phosphate-free and phosphate-containing EG electrolytes to several anodizing potentials. The impedance (**Figs. 5.11a and 5.12a**) changes linearly with frequency at a slope of approximately -1 and the phase angle (**Figs. 5.11b and 5.12b**) reaches a value close to -90^o in a wide frequency range, being typical of dielectric anodic films. In this frequency range, the impedance increases with anodizing potential.

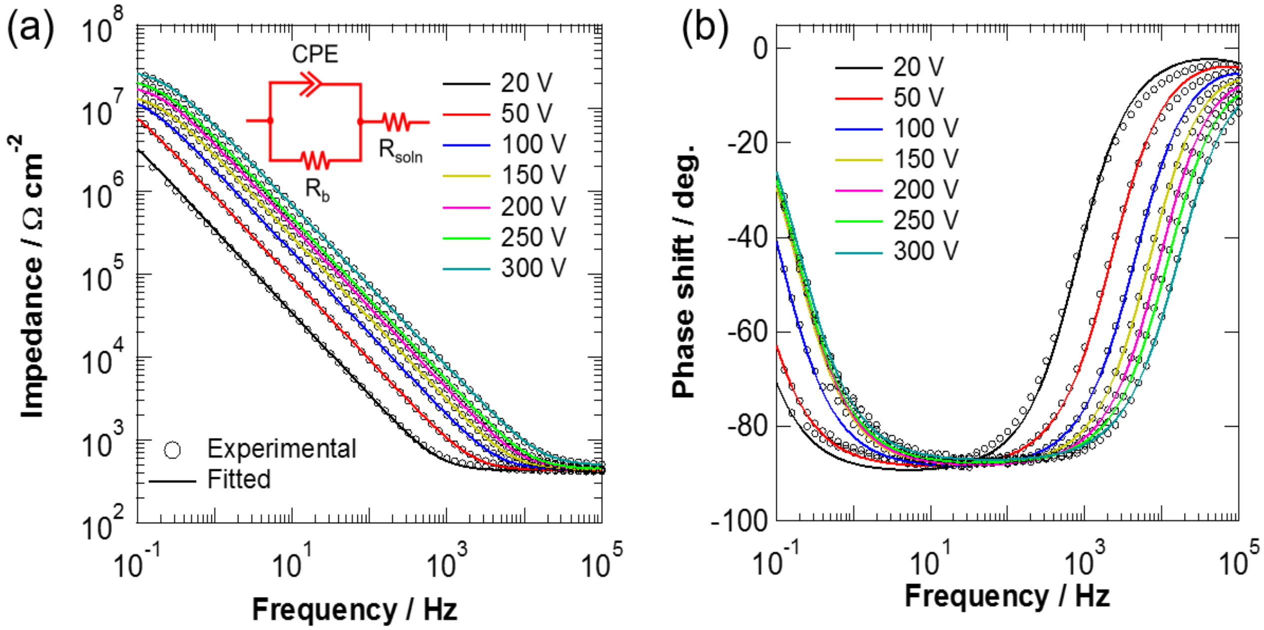

Figure 5.11 Impedance bode-plots of the magnetron-sputtered magnesium films anodized to several potentials at a constant current density of 10 A m^{-2} in the EG electrolyte containing 0.1 mol dm^{-3} ammonium fluoride and 0.1 mol dm^{-3} H_2O at 293 K.

Using an equivalent circuit shown in **Fig. 5.11a**, the capacitances of the anodic films were obtained. To consider the non-ideal capacitive behavior of the anodic film, the origin of which is often explained in terms of surface roughness, a constant phase element (CPE) was used instead of an ideal capacitance. The impedance of a CPE is given by

$$Z_{CPE} = 1 / Q (j\omega)^{\alpha} \qquad (5\text{-}1)$$

In which ω is the angular frequency, and Q and α are the pre-exponential factor and exponential factor ($0 \leq \alpha \geq 1$), respectively. When α equals 1 a CPE simplifies to a capacitor, while a CPE represents a pure resister when α equals 0. In the present measurements, α values were close to 1, being always higher than 0.97. The capacitances, C_b, of the anodic films were estimated using the following Hsu and Mansfeld formula [17]

$$C_b = Q\ (\omega_{max})^{\alpha-1} \qquad (5\text{-}2)$$

in which ω_{max} is the frequency at a maximum of the impedance of imaginary part (-*Zimg*) in -*Zimg* - *logf* plot.

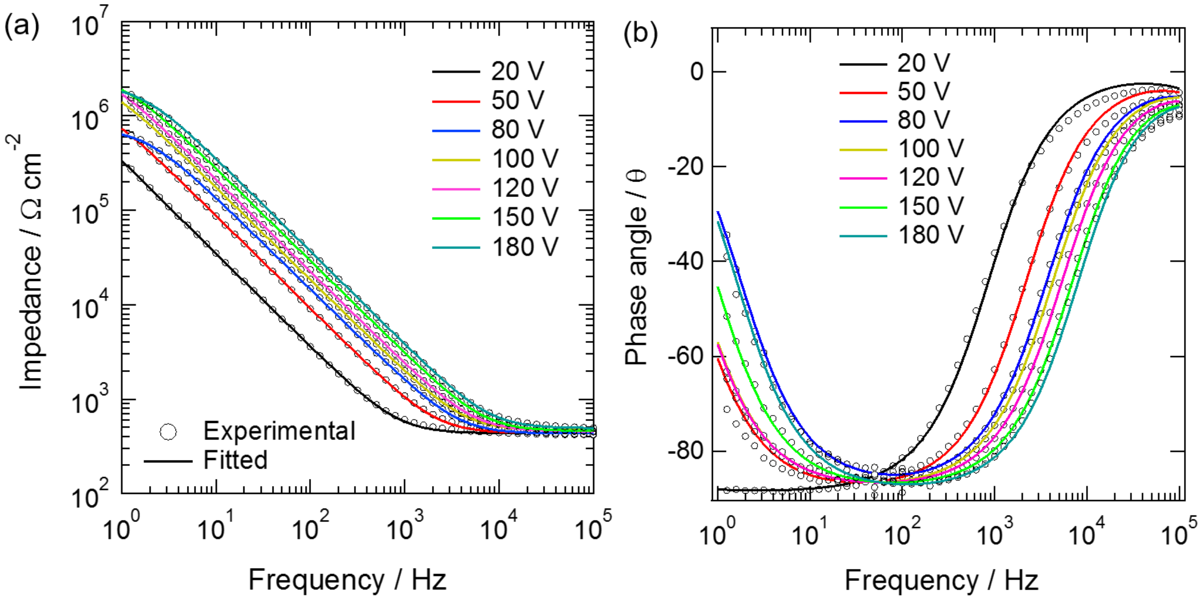

Figure 5.12 Impedance bode-plots of the magnetron-sputtered magnesium films anodized to several potentials at a constant current density of 10 A m^{-2} in the EG electrolyte containing 0.1 mol dm^{-3} ammonium fluoride, 0.1 mol dm^{-3} dipotassium hydrogen phosphate and 0.1 mol dm^{-3} H_2O at 293 K.

Fig. 5.13 shows the changes in the reciprocal of capacitance with the formation potential for the films anodized with or without phosphate addition. The reciprocal capacitance increases linearly with the anodizing potential, as expected from the following equation.

$$C_b = \frac{\varepsilon_o \varepsilon_{ox} S}{d} = \frac{\varepsilon_0 \varepsilon_{ox} S}{kV} \qquad (5\text{-}3)$$

in which, ε_o is the permittivity of vacuum, ε_{ox} is the relative permittivity of the anodic film, *S* is the surface area, *d* is the thickness of the anodic film and *V* is the anodizing potential. The capacitance of the anodic films formed in the phosphate containing electrolyte is almost similar to that in the phosphate-free electrolyte at the same anodizing potential, despite the fact that the thickness of the former anodic films is much larger than that of the latter films. This indicates that the amorphous phosphate-containing anodic films have larger capacitance compared with the anodic films containing a crystalline MgF_2 phase. The relative permittivity of the anodic films estimated from Eq. (3), formed in the phosphate-free and phosphate-containing electrolytes are 6.1 and 8.8, respectively. The value of the phosphate-free anodic films is close to that of the previously reported surface film formed on mechanically polished magnesium by immersion in 10% HF aqueous solution at room temperature [23]. The similar values in both films are reasonable since MgF_2 is present predominantly in both films.

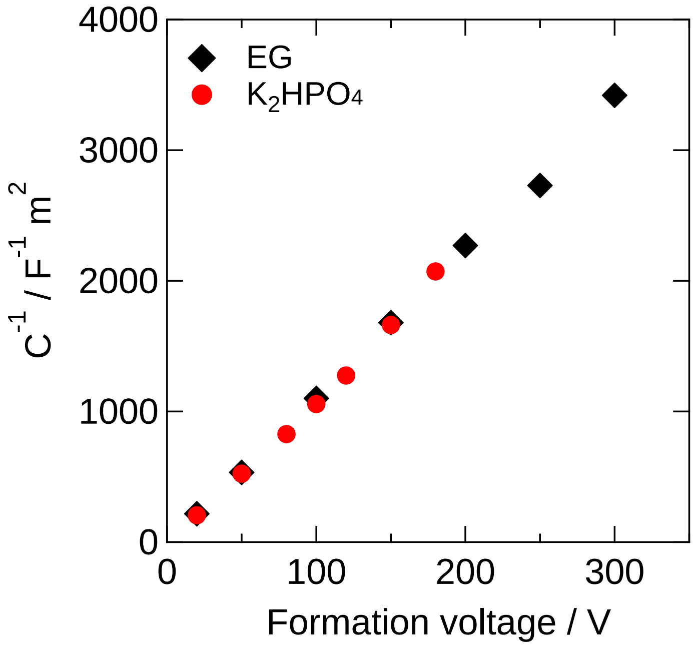

Figure 5.13 Change in the reciprocal of the capacitance of the anodic films with anodizing potentials. The anodic films were formed at a constant current density of 10 A m^{-2} in the EG electrolytes containing 0.1 mol dm^{-3} ammonium fluoride and 0.1 mol dm^{-3} H_2O with and without 0.1 mol dm^{-3} dipotassium hydrogen phosphate.

It is interesting that the incorporation of phosphate increases the relative permittivity of the present fluoride-based anodic films on magnesium, although the incorporation of phosphate often reduces the relative permittivity of oxide-based anodic films [24]. This may be partly due to the increased oxygen content in the phosphate-containing anodic films; the oxide-based anodic films have higher relative permittivity compared with fluoride-based anodic films. The enhanced relative permittivity may also be related to the change in film structure from crystalline to amorphous. The phosphate ions distribute throughout the anodic films, in contrast to the limited incorporation of electrolyte anion species in the barrier-type anodic films formed on a range of valve metals in aqueous electrolytes [25]**.** This means that various electrolyte species, in addition to phosphate, may influence largely the structure and properties of the anodic films formed on magnesium in fluoride-containing organic electrolytes.

5.3 Discussion

5.3.1 Current efficiency

Uniform growth of anodic films proceeded on magnetron-sputtered magnesium film in the EG-H_2O electrolytes containing both fluoride and phosphate in a wide H_2O concentration range up to 100 vol. %, as confirmed by scanning electron micrographs of the anodized magnesium surfaces (**Fig. 5.4**). The growth efficiency of the anodic films formed at various H_2O concentrations was estimated from the comparison of the electric charge passed during anodizing and that used for the formation of the anodic film. The latter was estimated from the number of Mg^{2+} ions in the anodic film, which was obtained by RBS analysis. The results are summarized in **Table 5.2**. The thickness of the magnesium film consumed by anodizing was also estimated from the RBS analyses. The electric charge passed during anodizing is in a good agreement with that estimated from the thickness of magnesium film consumed by anodizing, indicating that the electric charge is used mostly for the oxidation of magnesium metal. The charge for other reactions, such as oxygen generation was negligible. The current efficiency for the anodic film growth is close to 100 % when magnesium is anodized at low H_2O concentrations up to 10 vol. %. The efficiency is reduced to ~75 % and ~50 % at 50 and 100 vol. % H_2O, respectively. Thus, even at such low efficiencies uniform anodic films with flat film surface are developed on a magnetron-sputtered magnesium film.

As shown in **Fig. 5.1**, the voltage increases linearly with time to more than 100 V in the phosphate-containing electrolytes, although the slope reduces with an increase in H_2O concentration. The slope of the voltage rise is described by the following equation;

$$\frac{\mathrm{d}V}{\mathrm{d}t} = \frac{\eta E M i}{zF} \tag{5-4}$$

where V is the anodizing voltage, t is the anodizing time, E is the electric field across the anodic film, η is the current efficiency for film growth, M is the molar volume of the anodic film, i is the current density, z is the equivalent number and F is Faraday's constant. The slope ($\mathrm{d}V/\mathrm{d}t$) is, therefore, dependent upon the current efficiency, electric field strength, and the molar volume of the anodic film, which change with the H_2O concentration in the electrolyte. The slope estimated using the equation (1) is also plotted in **Fig. 5.2**. The estimated slopes are similar to the measured one. As shown in **Table 5.1**, the thinner anodic films are formed by increasing H_2O concentration. The electric field strength at 100 % H_2O is 1.6 times that in 0.18 vol. % H_2O. However, both the current efficiency and molar volume decrease with an increase in the current efficiency. The decrease in the molar volume with an increase in the H_2O concentration is estimated from the increased film density shown in **Table 5.1**. The decrease in the current efficiency and molar volume is larger than the increase in the field strength, therefore, the slope decreases with an increase in the H_2O concentration.

The film growth efficiency might be reduced by the direct ejection of outwardly migrating Mg^{2+} ions into electrolyte at the film/electrolyte interface. In the fluoride-containing EG-H_2O and glycerol-H_2O electrolytes, the anodic films are formed by simultaneous migrations of cations (Mg^{2+}) outwards and anions (mainly F^- and O^{2-}) inwards [15, 16]. The transport number of cations was estimated to be ~ 0.6 in the phosphate-free electrolytes, but it increased further to 0.72 in the phosphate-containing EG-H_2O. The transport number of cations is usually less than 0.5 for the anodic films formed on many valve metals, such as aluminum, bismuth, niobium, tantalum, titanium, and zirconium. The relatively high transport number of cations is one of the characteristics of the anodic films formed on magnesium in the fluoride-containing electrolytes. Because of the high transport number of cations, film material must be formed at the film/electrolyte interface, in addition to the metal/film interface, even at a current efficiency of 50 %. In other words, the ejection of Mg^{2+} into electrolyte and film formation occur simultaneously at the film/electrolyte interface in the aqueous electrolyte containing both fluoride and phosphate.

In anodizing of aluminum in acid electrolytes, porous anodic alumina films, not barrier-type films, are formed. Barrier-type anodic alumina films are formed usually in neutral aqueous electrolytes since the anodic films grow at high current efficiency. In acid electrolytes, no film material is formed at the film/electrolyte interface, and field-assisted ejection and/or field-assisted dissolution proceeded to form a porous layer. It was reported that direct ejection of outwardly migrating cations into electrolyte at the film/electrolyte interface without forming an oxide at this interface was a prerequisite for the formation of porous anodic films. The formation of barrier-type anodic films on magnesium even at the current efficiency of 50 % in the aqueous solution in the present study might be associated with the fact that film material is still formed at the film/electrolyte interface in addition to the partial ejection of Mg^{2+} ions into electrolyte at this interface. Non-uniformity of the film thickness induces the local increase in the field strength. The field-assisted dissolution is enhanced at the film/electrolyte interface by the increased field strength, developing pores in the anodic film.

As mentioned above, a light band, rich in oxygen species, was found in the anodic film in phosphate free electrolytes at low water concentrations [15-16]. The band was associated with an air-formed film, which was present before anodizing. Thus, the location of the band was assumed to be a marker plane, above which film material was formed at the film/electrolyte interface. In the phosphate-containing electrolyte, the band corresponds to the boundary between an outer layer containing a relatively high concentration of phosphate and an inner layer containing a less amount of phosphate [17]. By assuming a marker plane at the boundary between the outer and inner layers, the transport numbers of cations in the anodic films formed at 0.18 and 10 vol.% H_2O, estimated from the number of Mg^{2+} ions in the outer layer with respect to that in the anodic film, were 0.73 and 0.74, respectively, which were in agreement with the previous study [26]. At 50 and 100 vol. % H_2O, the current efficiency for film formation was low, as discussed above. By considering the dissolved amount of Mg^{2+} ions, the transport number of cations was estimated even at 50 and 100 vol. % H_2O. The value was 0.8 in both H_2O concentrations in the electrolyte, indicating no significant change in the transport number of cations with H_2O concentration. As a consequence of the partial dissolution of Mg^{2+} ions from the film/electrolyte interface under the presence of the high electric field during anodizing, the thickness ratio of the outer layer with respect to the total film thickness is reduced at 50 and 100 vol. % H_2O as shown in **Table 5.1**. Because of such a high transport number of cations, an outer layer formed at the film/electrolyte interface is present even at low current efficiency close to 50 %. The formation of film material at the film/electrolyte interface is a contrast to the condition of the formation of no film material at the film/electrolyte interface for the formation of a porous anodic film [27]. Anodizing of magnesium in this aqueous electrolyte containing fluoride and phosphate is an interesting system for the formation of a uniform barrier–type anodic film even at low current efficiency. For a better understanding of both the film formation and dissolution processes at the film/electrolyte interface during anodizing of magnesium, the further detailed study is awaited.

5.3.2 Volume expansion factors

The difficulty of the formation of a protective surface film on magnesium is often explained in terms of the Pilling-Bedworth ratio (PBR), i.e., the ratio of the molar volume of the oxide to that of metal. The PBR values for most of the valve metals, including aluminum, niobium, tantalum, titanium, and zirconium are greater than unity, such that the oxide films formed on these metals could cover the entire metal surface. In contrast, the PBR value for MgO/Mg is only ~ 0.8. The value less than unity makes the formation of a protective film covering entire metal surface difficult. In fact, highly cracked oxide films, mainly consisting of MgO, were formed on high purity magnesium after immersion in H_2O for 48 h.

Table 5.3 summarizes the volume expansion factors, i.e., the thickness ratios of the anodic film to magnesium metal consumed, in anodizing of magnesium in the EG-H_2O electrolytes with various H_2O concentrations. Since the current efficiency for film formation is not always 100 %, the volume expansion factor is different from the PBR. When the anodic films are formed in the electrolytes containing $\leq$ 10 vol. % H_2O, the volume expansion factor is equal to PBR, being as large as ~2.0. The value is reduced to 1.28 in the electrolyte containing 50 vol. % H_2O, partly due to reduced growth efficiency of ~75 % (**Table 5.2**). The volume expansion factor in this electrolyte is reduced to 1.7 even if the growth efficiency of 100 % is assumed. This may arise from the fact that the concentration of incorporated phosphate is reduced at higher H_2O concentration in the electrolyte (**Table 5.1 and Figs. 5.8 and 5.10**). The volume expansion factor for the anodic film/Mg in the phosphate-free EG electrolyte containing 0.18 vol.% water is 1.67, being lower than that formed in the phosphate-containing electrolyte with the same H_2O concentration. The volume expansion factor in the aqueous electrolytes with and without phosphate is further reduced and becomes less than unity, as shown in **Table 5.3**. Despite the volume expansion factor less than unity, a uniform anodic film is formed in the phosphate-containing aqueous electrolyte (**Fig. 5.4e**). The finding indicates that the volume expansion factor greater than unity is not a critical factor for the formation of the anodic film. The formation of the uniform anodic film in the phosphate-containing aqueous electrolyte may be associated with the fact that the estimated PBR in this electrolyte is 1.7, being greater than unity.

In the phosphate-free aqueous electrolyte, it is more difficult to form anodic films uniformly to high voltages. However, as shown in **Fig. 5.1**, the voltage increases linearly with anodizing time. At low formation voltages, the anodic films appear to grow uniformly even in the phosphate-free electrolyte. Because of the low breakdown voltage (~ 56 V), the anodic film could not thicken to more than 70 nm. The quantitative RBS analysis of such a thin film was difficult, making the PBR, growth efficiency and film composition remaining unclear. From TEM cross-sections, the volume expansion factor is estimated to be as low as ~ 0.64 (**Table 5.3**), which is again lower than that in the phosphate-containing electrolyte. This low value may be due to low current efficiency, not due to low PBR, such that linear voltage rise occurs at low formation voltages. The easy breakdown and non-uniform film growth below 50 V is a subject of future study.

5.3.3 Fluoride distribution

It is a well-known fact that ionic transport processes involved in amorphous anodic oxide films on valve metals are very complex [28]. Generally, the growth of amorphous oxide films proceeds by the migration of metal and oxygen ions in a co-operative manner under high electric field. In addition, electrolyte-derived anions species are incorporated into the films during film growth and it is generally accepted that fluoride species migrate faster than oxide ions and accumulate near the metal/film interface [29]. However, the detail consideration of anodic films on magnesium by RBS analysis reveals the absence of fluoride-enriched layer near the metal/film interface. This is in contrast to the film formation on iron, where the fluoride-rich layer was always present near the metal/film interface regardless of the water concentration. On possibility of such contrasting behavior of film growth in magnesium anodizing is the relatively low transport number of anions, which is as low as ~ 0.2 in fluoride-containing aqueous electrolyte. Thus, Mg^{2+} cations contribute majority of the ionic current compared with anion species and it is likely that relatively low migration of fluoride species hinders the formation of fluoride-enriched layer near the metal/film interface. Furthermore, the unusual presence of phosphate species throughout the film thickness and absence of fluoride-rich layer may also suggest that growth of anodic film might be proceeded by different mechanism from the usual cation-anion co-operative transport process. However, we must not jump into the final conclusion without further consideration of such anomalous behavior.

In summary, the electrolytes containing fluoride and phosphate are suitable to grow a uniform anodic film on magnesium to high voltages of more than 100 V. The anodic films are barrier-type even if the growth efficiency is as low as ~ 50 %. The formation of phosphate-incorporated oxyfluoride films with PBR greater than unity and high cation transport number of cations (~ 0.75) may be responsible for the formation of uniform anodic films even in aqueous electrolyte at low efficiency.

5.4 Conclusions

1. Barrier-type anodic films are formed galvanostatically to more than 100 V on magnetron-sputtered magnesium films in the EG-H_2O electrolytes containing ammonium fluoride and dipotassium hydrogen phosphate in a wide H_2O concentration range including 100 vol. % H_2O.
2. The anodic films are apparently amorphous and consist of phosphate-incorporated oxyfluoride. The amount of phosphate in the anodic films decreases gradually with an increase in H_2O concentration in the electrolyte. The phosphate distributes throughout the film thickness.
3. The anodic films consist of two layers with an inner layer containing less amount of phosphate. The inner layer is formed at the metal/film interface by inward migration of anions and the outer layer is formed at the film/electrolyte interface by outward cation migration.
4. The efficiency of film formation is close to 100 % at low H_2O concentrations but decreases to 52 % in the EG-free aqueous electrolyte. Even at such a low efficiency, a barrier-type film of uniform thickness is developed.
5. In contrast to anodizing of iron, no fluoride-rich layer is developed neat the metal/film interface.

References:

[1] J. E. Gray, B. Luan, *J. Alloys Compd.,* **336**, 88 (2002).

[2] C. Blawert, W. Dietzel, E. Ghali, G.L. Song, *Adv. Eng. Mater.,* **8** , 511 (2006).

[3] R. Arrabal, A. Pardo, M.C. Merino, M. Mohedano, P. Casajus, E. Matykina, P. Skeldon, G. E. Thompson, *Corros. Sci.,* **52**, 3738 (2010).

[4] S. P. Sah, Y. Aoki, H. Habazaki, *Mater. Trans.*, **51**, 94 (2010).

[5] K. Murakami, M. Hino, M. Hiramatsu, K. Nakai, S. Kobayashi, A. Saijo, T. Kanadani, *Mater. Trans.,* **48**, 3101 (2007).

[6] C. S. Lin, Y.C. Fu, *J. Electrochem. Soc.,* **153**, B417 (2006).

[7] S. Moon, Y. Nam, *Corros. Sci.,* **65**, 494 (2012).

[8] Tanaka, K, Anodization with the Coloring of magnesium and magnesium alloys, *European Patent* (1993).

[9] J. M. Macak, P. Schmuki, *Electrochim Acta,* **52**, 1258 (2006).

[10] S. Berger, J. Faltenbacher, S. Bauer, P. Schmuki, *Phys. Status Solidi Rapid Res. Lett.,* **2**, 102 (2008).

[11] W. Wei, K. Lee, S. Shaw, P. Schmuki, *Chem. Commun.,* **48**, 4244 (2012).

[12] A. Jagminas, K. Mazeika, N. Bernotas, V. Klimas, A. Selskis, D. Baltrunas, Appl. *Surf. Sci.,* **257**, 3893 (2011).

[13] J. M. Hernandez-Lopez, A. Nemcova, X.L. Zhong, H. Liu, M.A. Arenas, S.J. Haigh, M.G. Burke, P. Skeldon, G. E. Thompson, *Electrochim. Acta*, **138**, 124 (2014).

[14] H. Habazaki, F. Kataoka, E. Tsuji, Y. Aoki, S. Nagata, P. Skeldon, G.E. Thompson, *Electrochem. Commun.,* **46**, 30 (2014).

[15] H. Habazaki, F. Kataoka, E. Tsuji, Y. Aoki, S. Nagata, P. Skeldon, G.E. Thompson, *Electrochem. Commun.,* **46**, 30 (2014).

[16] J. M. Hernandez-Lopez, A. Nemcova, X.L. Zhong, H. Liu, M.A. Arenas, S.J. Haigh, M.G. Burke, P. Skeldon, G.E. Thompson, *Electrochim. Acta,* **138**, 124 (2014).

[17] H. Habazaki, F. Kataoka, K. Shahzad, E. Tsuji, Y. Aoki, S. Nagata, P. Skeldon, G. E. Thompson, *Electrochim. Acta,* **179**, 402 (2015).

[18] K. M. Ismail, S. Virtanen, *Electrochem. Solid-State Lett.,* **10**, C9 (2007).

[19] M. Taheri, J.R. Kish, *J. Electrochem. Soc.,* **160**, C36 (2013).

[20] M. Kato, E. Uchida, T. Kudo, *J. Met. Finish. Soc. Jpn.,* **35**, 475 (1984).

[21] K. Shimizu, G. E. Thompson, G.C. Wood, *Thin Solid Films,* **77**, 313 (1981).

[22] K. Shimizu, G. E. Thompson, G.C. Wood, *Thin Solid Films,* **81**, 39 (1981).

[23] C. H. Hsu, F. Mansfeld, Technical note: *Corros. Sci.,* **57**, 747 (2001).

[24] M. Santamaria, F. Di Quarto, S. Zanna, P. Marcus, *Electrochim. Acta,* **56**, 10533 (2011).

[25] Y. M. Li, L. Young, *J. Electrochem. Soc.,* **147**, 1344 (2000).

[26] G. C. Wood, P. Skeldon, G. E. Thompson, K. Shimizu, *J. Electrochem. Soc.,* **143**, 74 (1996).

[27] G. E. Thompson, *Thin Solid Films*, **297**, 192 (1997).

[28] J. P. S. Pringle, *J. Electrochem. Soc.*, **120**, 398 (1973).

[29] K. Shimizu, H. Habazaki, P. Skeldon, G. E. Thompson, G. C. Wood, *Electrochim. Acta,* **45**, 1805 (2000).

Chapter 6

General conclusions and future suggestions

This dissertation was aimed to understand the formation behavior of anodic films on high purity iron and magnesium in the fluoride containing ethylene glycol electrolyte and attention has been focused on the formation behavior and growth mechanisms by the addition of water. Based on observations of morphologies, composition, and structure of anodic films on iron and magnesium, final conclusions are summarized in the following section. Suggestions for future work are also presented.

6.1 General summary and conclusions

1. The film morphology, composition, and structure of anodic films on iron are largely influenced by water concentration. Thicker anodic films are developed by increasing water concentration up to 1.5 mol dm^{-3} in anodizing of iron at 50 V for 15 min and film thickness is reduced at 2.0 mol dm^{-3} water despite a further increase in the electric charge during anodizing. The reduced thickness at this water concentration is associated with enhanced chemical dissolution and gas evolution. Typical scalloped metal/film interface is developed only when the water concentration is at and above 1.5 mol dm^{-3}. The distribution of fluoride in the anodic films is dependent upon the water concentration in electrolyte; the enrichment of fluoride at the cell boundaries occurs only at high water concentration, while fluoride enriches only just above the metal/film interface at low water concentration. Nanotubular morphology is developed by preferential dissolution of the fluoride-rich layer at the cell boundaries, such that relatively high water concentrations are necessary to develop nanotubular anodic films on iron (Chapter 3).

2. Barrier-type and porous-type anodic films have been successfully fabricated potentiodynamically by employing ethylene glycol electrolyte containing fluoride and small amount of water. The film morphology of the anodic films on magnetron-sputtered iron is mainly

dependent on potential sweep rate; a barrier-type film at high sweep rate and a nanoporous-type film at low sweep rate. The barrier-type film is formed at the low efficiency of 49 %, suggesting that no film material is developed at the film/electrolyte interface, while the nanoporous film is developed at the much lower efficiency of 37 % even though both films are anodized to same 50 V. The faster voltage sweep rate impedes the pore initiation, such that a barrier-type film is obtained. The anodic films at low and high sweep rates consist of an outer iron (III) hydroxyfluoride layer with a much thinner inner FeF_3 layer. The inner layer is formed because of the fast migration of fluoride ions compared to the oxygen species. During immersion or re-anodizing of the iron specimen with an approximately 100-nm-thick, barrier-type anodic film at and below 15 V, thinning of the anodic film proceeds uniformly and film dissolution is enhanced by applying an electric field. A nanoporous morphology in the anodic film emerges above a critical electric field of 2.8 MV cm^{-1} (Chapter 4).

3. In the second part of this study, the formation behavior of barrier-type anodic film on magnetron-sputtered magnesium was investigated in detail. A barrier-type anodic film forms at a constant current density of 10 A m^{-2} in EG-H_2O mixed electrolytes containing 0.1 mol dm^{-3} ammonium fluoride and 0.1 mol dm^{-3} dipotassium hydrogen phosphate. The growth efficiency is close to 100 % up to 10 vol. % H_2O, but decreases to ~ 52 % in the EG-free aqueous electrolyte. Even at such a low efficiency in the aqueous electrolyte, a uniform barrier-type anodic film with flat and parallel metal/film and film/electrolyte interfaces is developed over 100 V. This is a contrast to the non-uniform film growth and low breakdown voltage in the phosphate-free aqueous electrolyte containing ammonium fluoride. The anodic films appear to be amorphous regardless of H_2O concentration in the phosphate-containing electrolytes and consist of phosphate-incorporated oxyfluoride. The phosphate incorporation is suppressed by an increase in H_2O concentration. In addition, the anodic films consist of two layers with an inner layer containing less amount of phosphate. The outer layer is probably formed at the film/electrolyte interface by the migration of Mg^{2+} ions outwards, while the inner layer is formed at the metal/film interface. The film formation at the former interface even in the aqueous electrolyte at low efficiency is likely to contribute to the formation of barrier films, not porous anodic films (Chapter 5).

4. This study demonstrates the formation of different types of film morphologies on iron and magnesium in the ethylene glycol electrolytes containing fluoride and water; Nanoporous or nanotubular films are mainly formed on iron while only barrier-type films are developed on magnesium even though the growth efficiencies are similar. In addition, a fluoride-rich layer is developed in the anodic films just above the metal/film interface in anodizing of iron, but no such enriched layer is developed on magnesium. The different morphology and fluoride distribution for the two metals may be due to different interfacial process at the film/electrolyte interface and different mechanism of ionic transport.

6.2 Suggestions for the future work

Through the work described in this thesis, it could be clarified that the morphology, composition, and growth mechanism are dependent upon the water concentration in the electrolyte in anodizing of iron. In particular, it is likely that the transition from “field-assisted dissolution” to “field-assisted flow” mechanism occurs due to an increase in water concentration. To clarify the detailed origin of such transition, it is important to evaluate the stress distribution during film growth and mechanical properties of the anodic films under the electric field. For the direct observation of flow mechanism in iron anodizing, tracer study with a selection of suitable tracer and quantitative determination of the electric field and stress distribution by the computational approach in the barrier film beneath the porous film is needed.

Direct observation of the porous film morphology is limited owing to nanoscale nature of the pore and cell. In addition, SEM and TEM provide only two dimensions images of the porous structure, which can be improved by employing 3D TEM and SEM in combination with computer simulation and observation of distribution of incorporated tracer species within the films can be enhanced by the use of 3D electron tomography. This will help in the more precise understanding of the growth mechanism of the barrier and porous-type films.

Although, uniform anodic films on magnesium with high PBR are developed by the addition of phosphate. The addition of various other trace elements can further improve the pilling bed-worth ratio and contribute to the formation of uniform films to higher anodizing voltage in both organic and aqueous electrolytes. At present, no evidence of self-organized porous anodic film on magnesium has been found under present anodizing conditions. Such films can be attained by the complete removal of outer layer at very low growth efficiency. This could be achieved by the addition of appropriate additives in the anodizing electrolytes.

6.3 Applications of anodic films on iron and magnesium

Finally, it is worth-mentioning to address the potential applications of anodic films on iron and magnesium. Production of photo-corrosion stable materials that can capture a significant portion of solar energy and its subsequent utilization for water splitting remains an unsolved challenge over the past few decades. The inexpensive iron-based anodic films are promising materials as photoanode for capturing solar spectrum. Efficient energy conversion and storage requirements for water splitting can be well accomplished owing to the electronic, physical, and chemical nature of the iron-based films as well as low processing cost of anodizing. However, iron-based materials suffer recombination losses due to low electron mobility and short diffusion length of minority carrier. Through the understanding of critical factors and morphological control of anodic films, it is likely to produce nanoporous and nanotubular nanostructures with controlled morphology that would allow charge separation prior to recombination and ultimately would result in a remarkable increase in the photoelectrochemical properties. Anodic films on iron are also the potential candidate for the protection of underlying substrate against corrosion by the application of suitable adhesive polymer coatings. For such applications, understanding of the distribution of fluoride species and its eventual removal from the anodic films is essential for improving the corrosion protection and adhesion of coatings. The morphological control of porous anodic films on iron can further extend their promising applications as electrodes for iron-air batteries, electrochemical capacitors, and gas sensors.

Potential applications of magnesium films include corrosion and wear resistant coatings as well as dielectric materials for electronic use. Corrosion of magnesium-based components is an important issue in the automotive, aerospace, defense, electronics, and oil and gas industries. Magnesium’s weight advantage over aluminum makes it an attractive alternative, especially because of the high cost of fuel. For instance, lightweight and high-performance magnesium-based alloys are necessary for fuselage structures, aircraft skins, aero engine frames, and components.

Magnesium-based alloys are also very promising as engine materials in near future and corrosion is always an important problem in the cooling system of an engine block. Ethylene glycol and phosphate are main components of engine coolant. The understanding of formation behavior and hence subsequent corrosion study would lead to the selection of successful coolant material for magnesium components. Likewise, high corrosion resistant magnesium-based biomaterials are promising because of magnesium’s physiological compatibility, bioactive behavior, and absorbable characteristics.

List of publications

[Publications]

1. **Khurram Shahzad**, E.Tsuji, Y. Aoki, S. Nagata, H. Habazaki, *Formation and field-assisted dissolution of anodic films on iron in fluoride-containing organic electrolytes*, Electrochimica Acta, **151** (2015) 363-369.
2. Hiroki Habazaki, Fumitaka Kataoka, **Khurram Shahzad**, Etsushi Tsuji, Yoshitaka Aoki, Shinji Nagata, Peter Skeldon, George E. Thompson, *Growth of barrier-type anodic films on magnesium in ethylene glycol electrolytes containing fluoride and water*, Electrochimica Acta, **179** (2015) 402-410.
3. H. Habazaki, T. Hiraga, **K. Shahzad**, E. Tsuji, and Y. Aoki, *Formation of Self-Organized Porous Anodic Films on Iron and Stainless Steels*, ECS transactions, **69** (2015) 211-223.
4. **Khurram Shahzad**, Chunyu Zhu, Etsushi Tsuji, Yoshitaka Aoki, Shinji Nagata, Hiroki Habazaki, *Growth of barrier-type anodic films on magnesium in ethylene glycol-water mixed electrolytes containing fluoride and phosphate,* Materials Transactions, **57** (2016) 1552-155.

[Conference proceedings]

1. **Khurram Shahzad**, E.Tsuji, Y. Aoki, S. Nagata, H. Habazaki, *On the influence of electric field on the dissolution rate of anodic films on iron*, Proceedings of 2nd International Symposium on Anodizing Science and Technology, 4-6 June, 2014, Sapporo, Japan.
2. **Khurram Shahzad**, E.Tsuji, Y. Aoki, S. Nagata, H. Habazaki, *Effect of sweep rate on the formation of nanostructured iron oxide films under potentiodynamic anodizing,* 3rd Frontier Chemistry Centre International Symposium, 13-14 June, 2014, Sapporo, Japan.

3. **Khurram Shahzad**, E.Tsuji, Y. Aoki, S. Nagata, H. Habazaki, *Formation behavior of nanoporous oxide films on iron under linear sweep anodizing*, 130th Meeting of Surface Finishing Society of Japan, September 23, 2014, Kyoto, Japan.
4. **Khurram Shahzad**, Fumitaka Kataoka, E. Tsuji, Y. Aoki, S. Nagata, H. Habazaki, *Formation behavior of barrier type anodic film on magnesium in EG-H_2O electrolytes containing fluoride and phosphate*, 82nd Meeting of the Electrochemical Society of Japan, March 15-17, 2015, Yokohama, Japan.
5. **Khurram Shahzad**, E. Tsuji, Y. Aoki, H. Habazaki, *Critical factors influencing on morphology and growth mechanism of anodic films on iron*, The Meeting of Electrochemical Society of Japan, September 12, 2015, Saitama, Japan.
6. **Khurram Shahzad**, E. Tsuji, Y. Aoki, H. Habazaki, *Formation of self-organized nanoporous and nanotubular anodic films on iron*, The 4th joint symposium between Hokkaido university and Harbin Engineering, Aug. 31-Sept. 2, 2015, Sapporo, Japan.
7. **Khurram Shahzad**, E. Tsuji, Y. Aoki, S. Nagata, H. Habazaki, *Influence of water concentration on growth efficiency of barrier type anodic film on magnesium,* 66th Annual Meeting of the International Society of Electrochemistry, October 4-9, Taipei, Taiwan, 2015.
8. H. Habazaki, T. Hiraga, **K. Shahzad**, E. Tsuji, and Y. Aoki, *Formation of Self-Organized Porous Anodic Films on Iron and Stainless Steels,* ECS meeting, Phoenix convention centre and the Hyatt Regency, October 11-15,2015, Phoenix, Arizona, United States.
9. **Khurram Shahzad**, E. Tsuji, Y. Aoki, H. Habazaki, *Formation behaviour of nanostructured anodic oxide films on iron*, Hokkaido university-University of California, Berkeley Joint Symposium on Chemical Sciences and Engineering, January 7th, 2016, Sapporo, Japan.
10. **Khurram Shahzad**, E. Tsuji, Y. Aoki, H. Habazaki, *Influence of Fluoride enrichment on the formation of nanotubes on iron*, 4th Frontier Chemistry Centre International Symposium, February 23-24, 2016, Sapporo, Japan.

Acknowledgments

I would like to express my gratitude to every laboratory and staff member of Hokkaido University who has helped and supported me during my PhD at Hokkaido University. Firstly, I would like to thanks to my supervisor **Professor Hiroki Habazaki**, for his priceless personal supervision, and edifying discussion with me. I am deeply grateful to my professor for giving me an opportunity and especially for being patient with me during my time at Hokkaido University. He has been a constant source of motivation throughout my journey here. He always pointed what is missing and what must be clarified and it is out of question that his insight is critical for this thesis. He is simply the best professor I have met in my life. The valuable suggestions of Professor Azumi, Professor Murakoshi, and Professor Hasegawa for improving this dissertation is highly appreciated. I am also grateful to Professor Y. Aoki, Professor E. Tsuji, Professor Chunyu Zhu, and Professor Soo Gil Park for their constructive criticism and suggestions to improve my research.

This research work could not be completed without a friendly work environment and positive discussions and helping hand of the members of Laboratory of Interfacial Electrochemistry. The help of **Mr. Kohei Kobayashi**, Mr. Tomizawa, Mr. Nakayama, **Doctor Konno**, **Miss Chiharu Kura**, Miss Matsura, Miss Inoue, and Mr. Shakhashita has been much appreciated. I am also deeply grateful to graduate school of Chemical Sciences and Engineering (CSE) and Ministry of Education, Culture, Sports, Science and Technology (MEXT), Japan for financial support of this research.

I am deeply grateful to my parents, my family, and Miss Ruba for their understanding, optimism, and constant backing during my PhD. I wouldn’t be where I am without their love and support. Finally, I would like to thank to ‘My ALLAH’ for giving me everything that made this possible.

Khurram Shahzad